Modeling, Simulation and Experimental Investigation of Charge Transport Properties of Dye Sensitized Solar Cells

A thesis submitted to the
University of the Petroleum and Energy Studies

For the Award of

Doctor of Philosophy

in

Electronics and Communication Engineering

By
Deepak Kumar

February 2021

SUPERVISOR(s)

Dr. Piyush Kuchhal

Dr. Kanak Pal Singh Parmar

UPES
UNIVERSITY WITH A PURPOSE

Department of Electrical and Electronics Engineering
School of Engineering
University of the Petroleum and Energy Studies
Dehradun-248007: Uttarkhand

Modeling, Simulation and Experimental Investigation of Charge Transport Properties of Dye Sensitized Solar Cells

A thesis submitted to the
University of the Petroleum and Energy Studies

For the Award of
Doctor of Philosophy
in
Electronics and Communication Engineering

By
Deepak Kumar
SAP ID: 500049549

February 2021

SUPERVISOR(s)

Dr. (Prof.) Piyush Kuchhal
Department of Physics, UPES

Dr. (Assoc.Prof.) Kanak Pal Singh Parmar
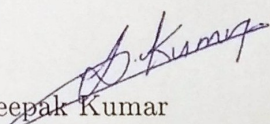Department of Physics, UPES

UPES

UNIVERSITY WITH A PURPOSE

Department of Electrical and Electronics Engineering
School of Engineering
University of the Petroleum and Energy Studies
Dehradun-248007: Uttarkhand

Declaration

Declaration

I declare that the thesis entitled "Modeling, Simulation and Experimental Investigation of Charge Transport Properties of Dye Sensitized Solar Cells" has been prepared by me under the guidance of Dr. (Prof.) Piyush Kuchhal (Supervisor), Department of Physics and Dr. (Assoc.Prof.) Kanak Pal Singh Parmar (Co-Supervisor), Department of Physics, University of Petroleum and Energy Studies (UPES), Dehradun. No part of this thesis has formed the basis for the award of any degree or fellowship previously.

Deepak Kumar
SAP ID: 500049549

Department of Electrical and Electronics Engineering
University of Petroleum and Energy Studies (UPES)
ENERGY ACRES, UPES, BIDHOLI, via, Prem Nagar
Dehradun, Uttarakhand 248007

Date: 02/02/2024

Certificate

Certificate

We certify that Deepak Kumar has prepared his thesis entitled "Modeling, Simulation and Experimental Investigation of Charge Transport Properties of Dye Sensitized Solar Cells", for the award of Ph.D degree of the University of Petroleum and Energy Studies (UPES), under our guidance. He has carried out the work at the Department of Electrical and Electronics Engineering, University of Petroleum and Energy Studies (UPES).

Supervisor(s)
Dr. (Prof.) Piyush Kuchhal (Supervisor)
Department of Physics
University of Petroleum and Energy Studies (UPES)
ENERGY ACRES, UPES, BIDHOLI, via, Prem Nagar
Dehradun, Uttarakhand 248007

Date: 02|02|2021

Dr.(Assoc. Prof.) Kanak Pal Singh Parmar (Co-Supervisor)
Department of Physics
University of Petroleum and Energy Studies (UPES)
ENERGY ACRES, UPES, BIDHOLI, via, Prem Nagar
Dehradun, Uttarakhand 248007

Date: 02/02/2021

ii

Abstract

Population growth significantly expanding the boundaries of residential areas and living standard for the mankind on the globe which further increases huge demand of electricity consumption. To meet the tremendous growth in energy consumption, electricity production through renewable energy resources can be considered as a fastest-growing energy sources to meet the demand of rapid growth of electricity generation. The Sun is the source of energy (clean and free) available to mankind which is pervasive, readily available and renewable. Unlike fossil fuels, which are found only in a few areas, solar energy is freely available in every part of the world. Thus, all countries can benefit significantly from solar energy, regardless of their geographical position. So, it is essential to harness the sun's irradiation to produce electricity. Solar cell technology is one of the suitable technologies to harness the solar energy to produce power. Among the various solar cell technologies such as silicon solar cell, dye-sensitized solar cell (DSSC), organic photovoltaic, quantum dot solar cells and perovskite solar cell, DSSC solar cell technology is adopted because of its attractive features such as low cost, high power conversion efficiencies under cloudy and artificial light conditions, offer transparency and optimum performance to cost ratio.

DSSC has a sandwiched like architecture based on key components: working electrode (photosensitive dye adsorbed on nano structured metal oxide semiconductor based electrode), a liquid redox couple and counter electrode which plays important role to achieve optimized photovoltaic (PV) performance. On light irradiation, the charge collection efficiency of DSSC depends on generation-recombination and transportation of charge carriers, dye of suitable energy band gap with a larger optical absorbance, charge transfer process at electrode/dye/electrolyte interface and losses of charge due to kinetics role of working electrode's light absorptivity/energetics of dye and transportation of redox ions.

In order to improve the efficiency of the DSSC, it is required to optimize the charge transport properties of the key components of DSSC. This research work is mainly focused on optimizing the properties (thickness and morphology) of working electrode (WE) of the DSSC sin order to achieve the optimized PV performance.

An highly crystalline TiO_2 powder consisting of morphologically rice-like nanoparti-

cles is synthesized by a simple hydrothermal process using a premixture of titanium isopropoxide, ethanol and aqueous ammonia. An efficient mechanism decoupling hydrolysis and condensation promotes the formation of a rice-like morphology. As the average particle size and BET properties of nanorice-like TiO_2 were found to be quite similar to a commercially available TiO_2 (Degussa P25), their photoelectric properties were compared as a DSSC electrode. Under 1 sun irradiation the photovoltaic efficiency of nanorice-like TiO_2 was measured to be ca. 20 % higher in contrast to the mediocre efficiency ($\sim$5.45 %) of P25. We suggest that together with a generally exploited reference, such nanorice-like TiO_2 could also be adopted as a model material for various applications.

A comparative investigation involving experimental and modelling-simulation is carried out to maximize the photovoltaic conversion efficiency (η) of a DSSC device assembled using N719 dye, an iodide redox liquid electrolyte and TiO_2 electrode. The measured current density-voltage (J-V) characteristics under 1 sun condition of a pre-assembled DSSC is simulated in a tiberCAD based microscopic model (TCMM) along with single-diode based macroscopic model (SDMM). The calibrated model parameters are then utilized for predicting a maximum η of a DSSC belonging to an unknown electrode's thickness (L). The microscopic simulations provided a good qualitative nature of J-V characteristics curves for different L and η values. A complete and best J-V curve fitting is achieved using a TCMM by incorporating an unaccounted series resistance of a FTO substrate. Particularly, model simulated J-V characteristics matches perfectly well to experimental results of a post-assembled DSSC device ($\eta \sim$ 5.46; L$\sim$12.0 μm) with a tolerable error ($<$0.1 %).

The theoretically modeled equations defining various bulk and interface impedances are incorporated with EIS spectrum analyzer software to fit the simulated EIS curves with experimentally measured EIS curves to evaluate the charger transfer and recombination properties of the assembled DSSCs. EIS fitting parameters investigated to study the impact of WE thickness on the charge transport properties of assembled DSSC. It is observed that the charger transfer resistance at TiO_2/electrolyte interface (R_k) and series resistance (R_s) are reduced from 8 $\Omega cm^2 \longrightarrow$ 4.05 Ωcm^2 and 14.5 $\Omega cm^2 \rightarrow$ 10.06 Ωcm^2 respectively which shows consistency with improvement in electron life time (τ_e) from 5.8 ms $\rightarrow$ 12.4 ms for increasing WE thickness, L = 3 μm $\rightarrow$ 12 μm. The combined impact of significant reduction in R_k and R_s along with improved trend of τ_e can be considered as major factors for efficient electron injection across Dye/TiO_2 interface hence increases short circuit current (I_{sc}) from 1.485 mA $\rightarrow$ 2.365 mA and photovoltaic conversion efficiency (η) from 3.55 % $\rightarrow$ 5.46 % for L = 3 μm $\rightarrow$ 12 μm, respectively. Moreover, a remarkable increment in η ($\sim$45 %), τ_e ($\sim$56.3 %) and a noticeable reduction in R_k($\sim$38.75 %), R_s ($\sim$23.8 %) are observed for WE variations (L = 3 μm $\rightarrow$ 6 μm).

Acknowledgement

First and foremost, I would like to thank Almighty God for giving me the strength, knowledge, ability and opportunity to undertake this research study and to persevere and complete it satisfactorily. Without his blessings, this achievement would not have been possible.

I would like to express my sincere gratitude to my supervisors Dr. (Prof.) Piyush Kuchhal and Dr. (Assoc.Prof.) Kanak Pal Singh Parmar for their continuous support in my Ph.D related study and research, for their patience, motivation, and immense knowledge. Their guidance helped me in all the time of research and writing of this thesis. I could not have imagined having better advisors and mentors for my Ph.D work.

I would like to express my heartfelt gratitude towards the Hon'ble Chancellor, Hon'ble Vice Chancellor of UPES and Dr. (Prof.) Kamal Bansal, Snr. Director Academic Development (UPES) who gave their kind consent to carry on this work and for providing support throughout this work.

I am thankful to Dr. Gurvinder Singh Virk, Dean SOE for providing consistent motivation to put best effort in this work.

I am also thankful to Dr. Sushabhan Choudhury (HoD, EEE), Dr. R. Gowri, Dr. Ranjan Mishra, Dr. Gagan Anand and entire faculty members of Electrical and Electronics Eng. Department for providing support and motivation in my research work.

I am also thankful Dr. D K Avasthi (Dean, R&D) and entire team of Research and Development Department for supporting my research by a SEED grant from UPES (UPES/RnD/122018/06). I am also thankful to the staff members of Nano science Lab and Pharmacy Lab(UPES).

I would be failing in my duties if I miss to thank Mr. Raj Gaurav Mishra and Dr. Syed Mohammad Tauseef for their constant help and support. I am also thankful to all of my friends who lent constant motivation and support.

The greatest sense of acknowledgement would go to my family members: my parents,my sisters and to my wife who have been in the roots of whatever I am and have achieved in my life including this research work.

Contents

List of Figures

List of Tables

List of Abbreviations

A

AM	Air Mass	AN	Aceto Nitrile
aSi	amorphous Silicon	ABS	Absorbance

B

BD	Black Body	BDDT	Bruauer, Deming, Deming and Teller
BET	Brunauer, Emmett, Teller	BJH	Barrett, Joyner, Halenda
BSEs	back Scattered Electrons	B-V	Butler-Volmer

C

CAD	Computer Aided Design	CB	Conduction Band
CdS	Cadmium sulphide	Cdse	Cadmium Selenide
CdTe	Cadmium Telluride	CE	Counter Electrode
CIGS	Copper Indium Gallium Selenide	CIS	Copper Indium Selenide
CL	CathodoLuminescence	CNT	Carbon Nano Tube
CO	Conducting Oxide	CPE	Constant Phase Element
CSi	Crystalline Silicon	CT	Charge Transfer
CZTS	Copper Zinc Tin Sulphide		

D

D-A	Donar-Acceptor	DC	Direct Current
DCA	Deoxy Cholic Acid,	DSL	Dyesol
DSSCs	Dye Sensitized Solar Cell	DLC	Double Layer Capacitance

E

EC	Ethyl Cellulose	ECD	Electrochemical Deposition
EIA	Energy Information Administration	EIS	Electrochemical Impedance Spectroscopy
EtOH	Ethyl Alcohol		

F

FDSSC	Flexible Dye Sensitized Solar Cells	FF	Fill Factor
FL	Finite-Length	FTO	Fluorine-Doped Tin Oxide
G			
GNP	Graphene Nano Platelets	GO	Graphene Oxide
H			
HEL	Higher Energy Level	HOMO	Highest Occupied Molecular Orbital
HT			
I			
IL	Ionic Liquids	IPCE	Incident Photon-to-Current Conversion Efficiency
ITO	Indium Doped Tin Oxide	IUPAC	International Union of Pure and Applied Chemistry
I-V	Current Voltage		
J			
JV	Current-Density Voltage		
L			
LEL	Lower Energy Level	LEs	Liquid Electrolytes
LHE	Light Harvesting Efficiency	LN_2	Liquid Nitrogen
LUMO	Lowest Unoccupied Molecular Orbital		
M			
MaP	Macro Porous	MeP	Meso Porous
ML	Multi Layer	MP	Micro Porous
MPP	Maximum Power Point	MS	Micro-Spheres
MWCNT	Multi-Wall Carbon Nanotubes		
N			
NaOH	Sodium hydroxide	NR	Nano-Rod
NS	Nano-Spehere		
O			
OECD	Economic Cooperation and Development	OPVs	Organic Photovoltaics
OS	Ohmic Series		

P

PbS	Lead Sulphide	PE	Photo Electrode
PL	Path Length	PSS	Poly-Styrene Sulfonate
PV	Photo Voltaic	PEDOT	Poly(3,4-EthyleneDiOxyThiophene
PEG	Poly Ethylene Glycol		

Q

QDSSC	Quantum Dot-Sensitized Solar Cells	QE	Quantum Efficiency
QSSELs	Quasi Solid State Liquid Electrolytes	QSS	Quasi Solid State

R

RF	Radio Frequency	RMSE	Root Mean Square Error

S

SDMM	Single-Diode Macroscopic Model	SEM	Scanning Electron Microscopy
SEs	Secondary electrons	SL	Seed layer
SSE	Sum Squared Error	SSTMs	Quasi State Transport Materials
SSP	Single Strip-Shaped		

T

TAS	Transient Absorption Spectroscopy	TBP	4-Tert-Butyl Pyridine
TCMM	Tiber CAD Microscopic Simulations	TCO	Transparent Conducting Oxide
TE	TiO_2-Electrolyte	TEC	
TTIP	Titanium-Isopropoxide	TW	Tera Watt

U

UV	Ultra Violet		

W

WE	Working Electrode	WISE	World Industrial Sector Energy

X

XRD	X-Ray Diffractometry	ZnO	Zinc Oxide
XRPD	X-Ray Powder Diffractometry		

List of Symbols

S*	Excited state of dye	V	Voltage
S	Ground state of dye	I	Current
S$^+$	Oxidized state of dye	R_{dc}	DC resistance
I$_3^-$	Triiodide	Z_{Re}	Real part of Z
I$^-$	Iodide	Z_{Im}	Imaginary part of Z
ν	Mobility	ω_d	Characteristic frequency of electron diffusion in the TiO$_2$
h	Plank's constant	ω_k	Characteristic frequency of recombinations at TiO$_2$/electrolyte interface
Pt	Platimum	ω_{CE}	Characteristic frequency of electrolyte/CE interface
e_{cb}	Electron in conduction band	ω_D	Characteristic frequency of electrolytes diffusion
ϕ_{ph}	Intensity of the incident light	R_{Pt}	Charge transfer resistance at electrolyte/CE interface
Φ_{coll}	Collection efficiency	Z_{Pt}	R-C equivalent impedance at electrolyte/CE interface
Φ_{reg}	Generation efficiency	C_{TCO}	DLC at exposed TCO/electrolyte
Φ_{inj}	Injection efficiency	C_{Pt}	Equivalent capacitance
I_o	Intensity at front sample	Z_d	Diffusion impedance of I$_3^-$ in electrolyte represented by Warburg element

I	Intensity at back side of sample	R_{CO}	Resitance at TCO/TiO$_2$ contact
k_{reg}	Rate constant for regeneration	C_{CO}	Capactitance at TCO/TiO$_2$ contact
k_{rec}	Rate constant for recombination	Rs$_{TCO}$	Sheet resistance of FTO glass.
ε	Permitivity	R_{OS}	Ohmic series resistance in DSSCs
$\tau_{1/2(inert)}$	Half time without redox mediator	Z_{OS}	Ohmic series impedeance
$\tau_{1/2(redox)}$	Half time with redox mediator	C_{Pt}	Equivalent capacitance
η_{reg}	Efficiency of the dye regeneration	R_k	Electron transfer resistance related to e/I$_3^-$ recombination
^oC	Degree Celsius	R_d	Electron transport or diffusion resistance,
V_{OC}	Open circuit voltage	n_k	CPE index
J_{SC}	Short circuit current density	Z_{DI}	Diffusion impedance experienced by I$_3^-$
η	Efficiency	R$_{DI}$	Diffusion resistance experienced by I$_3^-$
V_{OPT}	Optimum Voltage	D$_I$	Diffusion coeffcient of I$_3^-$
J_{OPT}	Optimum current density	δ	Diffusion length ofI$_3^-$
V_F	Voltage Equivalent to E_F	ω_{max}	Peak frequency)
E_F	Fermi energy level	Z_{WE}	Equivalent impedances for diffusion and recombination process
E_{red}	Redox energy level	Z_{DSSC}	Net impedance across the anode and cathode of the DSSC
V_{red}	Voltage Equivalent to E_{red}	Y_{CPE}	Admittance of CPE
ϕ_{ph}	Intensity of the incident light	n	Ideality factor
eV	Electron volt	$Z_{Uelement}$	User defined element
J_L	Photo current density	W_{sr}	Warburg coefficient.
R_s	Series resistance	W_{sc}	Warburg coeffcients.
R_{sh}	Shunt resistance	Z_{Ws1}	Warburg short terminus

Δ	Gradient	f_k	Peak frequency
$\mu_{I_3^-}$	Mobility of triiodide	τ_e	Electron life time
$n_{I_3^-}$	Concentration of I_3^-	L_n	Diffusion length of electrons
$\phi_{I_3^-}$	Electrochemical potential of I_3^-	L	Electrode thickness
$\bar{n}_{I_3^-}$	Concentration of I_3^- in dark conditions	F	Faraday constant
μ_c	Mobility of cation	R	Ideal gas constant
n_c	Concentration of cations	Å	Angstrom
ϕ_c	Electrochemical potential of cations	S_{BET}	Specific BET surface area
μ_e	Mobility of electrons	V_P	Pore-volume
n_e	Concentration of electrons	D_P	Pore-volume
ϕ_e	Electrochemical potential of electrons	f_p	peaks of characteristic frequency
$\bar{n}_c$	Concentration of cations in dark conditions	C_μ	Chemical capacitance
μ_{I^-}	Mobility of I^-	k_3	Dye regeneration rate constant
n_{I^-}	Concentration of I^-	$j^0_{cathode}$	Exchange current density
ϕ_{I^-}	Electrochemical potential of I^-	E^0_{redox}	Standard redox potential
$\bar{n}_{I^-}$	Concentration of I^- in dark conditions	J_0	Saturated dark current density
μ	Mobility	W(Q)	Lambert W-function
D	Diffusion Constant	V_T	Thermal equivalent voltage
N_{CB}	Effective density of states	P	Porosity
G(x)	Generation rate (e-h pairs)	A	Cell Area
$\alpha(\lambda)$	Absorption coefficient of the dye	Z(ω)	Impedance
$\psi(\lambda)$	Spectral power flux	ω	Angular frequency
R	Recombination rate	Z(0)	Impedance at 0 frequency
β	Exponent for the electron density	N_D^+	Oxidized dye molecules concentration

Chapter 1

Introduction

1.1 Global Demand of energy

One of the most important and biggest problems mankind facing today is the incredible increase in energy use. The United States Energy Information Administration (EIA) reported that world's energy consumption will increase by nearly 50 % between 2018 and 2050 as clearly seen from Figure 1.1 The large fraction of increase in energy consumption comes from those countries which are not listed in Organization for Economic Cooperation and Development (OECD), and this growth is focused in regions where demand is driven by the strong economic growth, particularly in Asia [1].
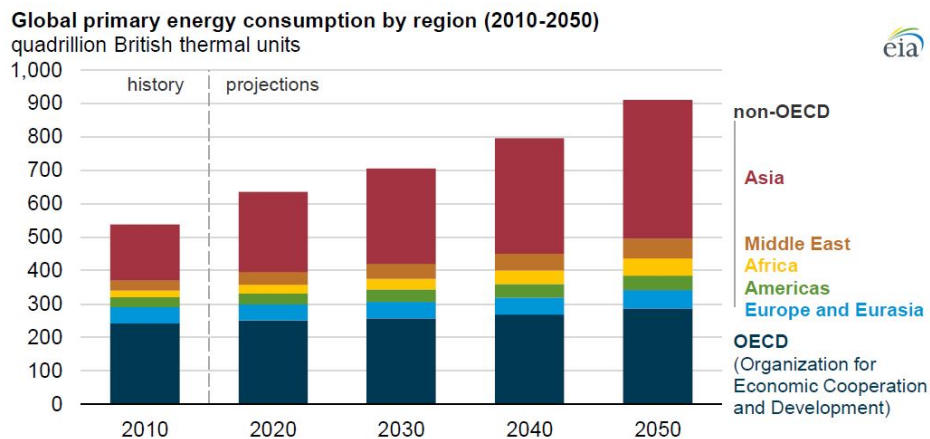
Figure 1.1: Global primary energy consumption by region (2010-2050) [1]

World industrial sector energy (WISE) usage will get increased by more than 30 % between 2018 and 2050 due to the increment in of good's consumption as clearly

1

seen from Figure 1.2. The industrial sector comprises of manufacturing, agriculture, construction, refining and mining, bags largest share of energy consumption throughout the projection period (2010-50). It is clearly projected that consumption for WISE is predicted to get reached to 315 quadrillion British thermal units (Btu) by 2050.

Increase of nearly 40 % in transportation energy consumption (TEC) can be projected from the reports for 2018-2050. This significant increase in TEC is largely driven by non-OECD countries, where TEC will increase by nearly by 80 % between 2018 and 2050. The growth in personal travel and freight movement can be considered as two major factors responsible for significant energy consumption in these countries as compared to OECD countries. Reports also suggested that energy consumption for residential and commercial of the sector will increase by 65 % in the projected period, i.e. from 91 quadrillion to 139 quadrillion Btu. Moreover factors like urbanization, rising income, and efficiently access to electricity will also lead to rising demand for energy [1] .
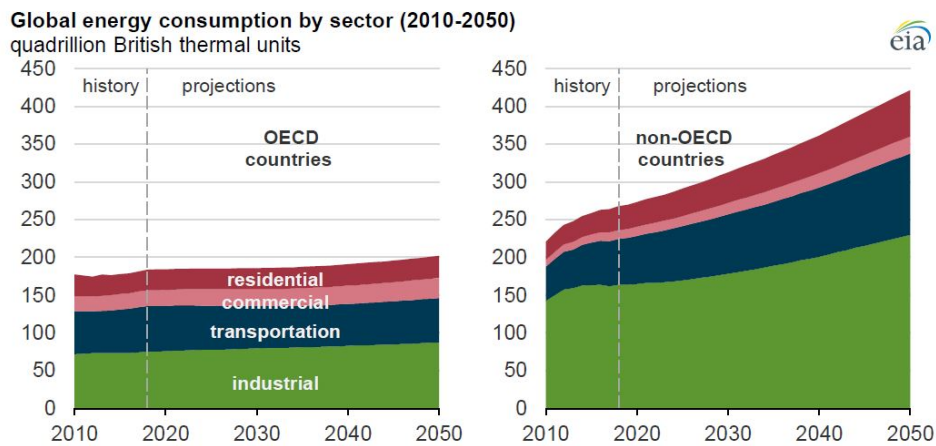
Figure 1.2: Global energy consumption by sector (2010-2050) [1]

To meet the tremendous growth in energy consumption, it is also projected that 79 % of increment in electricity generation is projected for 2018-2050 as mention in Figure 1.3. Population growth over the projection period will significantly expand the boundaries of residential areas and living standard for the mankind belongs to non-OECD countries. Hence give rise to huge demand for electrical appliances which further lead to raise the electricity consumption. The development electric vehicles

and rail expansion entering in the fleet of transportation sector is one of the major
factor which increases the demand of electricity in the projection period.
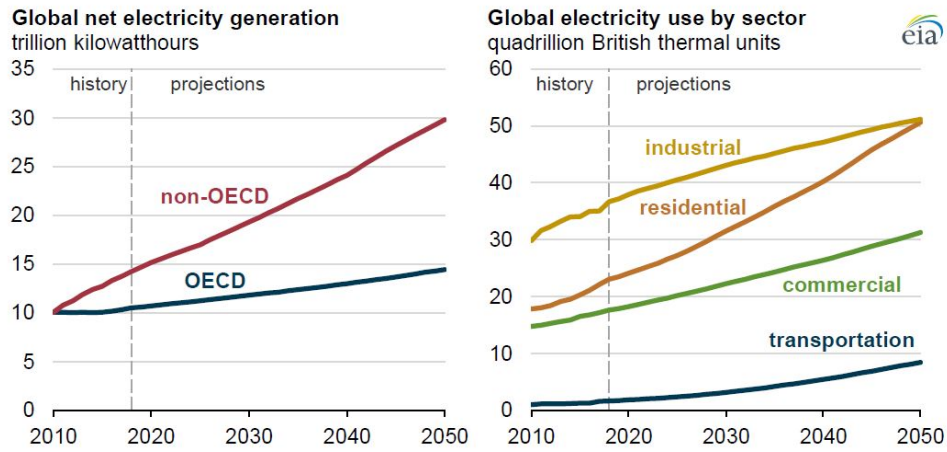
Figure 1.3: Global net electricity generation and usage by sector [1]
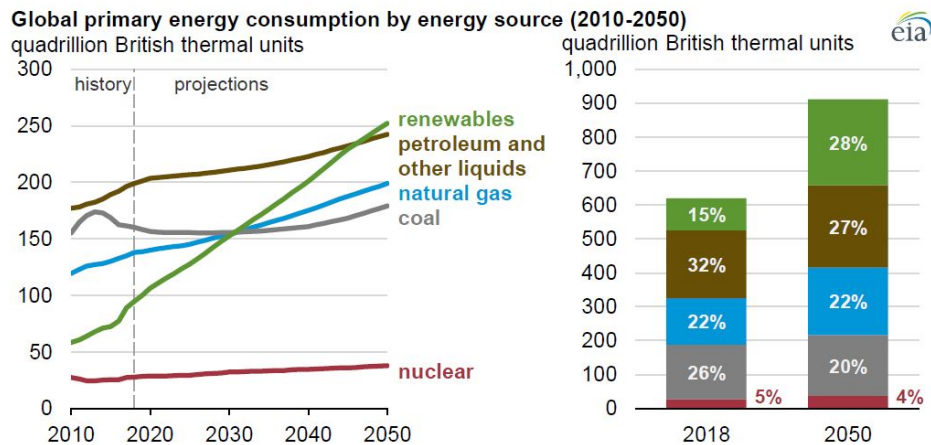
Figure 1.4: Global primary energy consumption by energy source (2010-2050) [1]

Electricity production through renewable including solar, wind, and hydroelectric
power can be considered as a fastest-growing energy sources to meet the demand
of rapid growth of electricity generation. Renewable energy resources will be sur-
passing the petroleum and other liquids to become the most used energy source
in projected period (2018-50) as clearly depicted from Figure 1.4. The Worldwide
annual energy consumption will get increased by 3.1 %, 0.6 %, 0.4 % and 1.1 %
in renewable, petroleum and other liquids, coal and gas consumption respectively
between 2018 and 2050. This trend clearly indicates that human being will more
rely on renewable energy resources to full fill the energy needs. The increase of more

than 40 % is projected for consumption of global natural gas and net consumption
will get reached nearly to 200 quadrillion Btu by 2050. Along with manufacturing of
chemical and primary metals, oil and natural gas extraction also account for growing
industrial demand. Moreover the demand of global liquid fuels consumption may
get increased by more than 20 %, and total consumption reaches more than 240
quadrillion Btu in 2050 (Figure 1.4) [1].

The rapid use of non renewable energy resources (fossil fuels) such as petroleum,
coal and natural gas has radically increased in 21st century as compared to the rate
of formation of fossil fuels which leads to complete consumption of the fossil fuel
reservoir. Hence, providing sustainable energy to mankind will be one of the major
challenges. According to the Kyoto Protocol CO_2 emission has to be reduced and
this should be done by utilizing less fossil fuel. Hence, the CO_2 problem is another
reason why new and environment friendly renewable energy resources are required
to be taken into account.

Our capability to meet the future needs of energy lies in the utilization of renewable
sources. Among the several kinds of renewable energy sources like solar energy, wind
power, hydroelectricity, bio-mass energy, geo-thermal power, and wave/tidal power
solar energy can be considered as one of the most promising energy source as the
sun irradiates 165 thousand terawatt (TW) of power each day to the surface of the
earth. It would be enough to match our global energy requirement by harnessing
the freely available energy direct from the sun.

1.2   Solar Energy : Source of Renewable Energy

Solar power is an energy directly received from the sun that can be converted into
thermal or electrical energy as per various requirement and applications. Solar
energy is the environmentally friendly and freely available most abundant renewable
energy source existing for the mankind.

1.2.1   Solar spectrum

The Sun is a source of black body (BD) radiation emitting everlasting amount of
energy at 5500 degree K with very wide spectrum, stretching out from the X-rays

4

wavelength (0.01 nm − 10 nm) to Radio wavelength (> 1 mm) with the spectral irradiance peak at 525 nm. Along with protecting the earth surface from excessive high energy radiation [2], the Earth's atmosphere also transform the profile of the solar spectrum as shown in Figure 1.5 .

Spectrum of Solar Radiation (Earth)
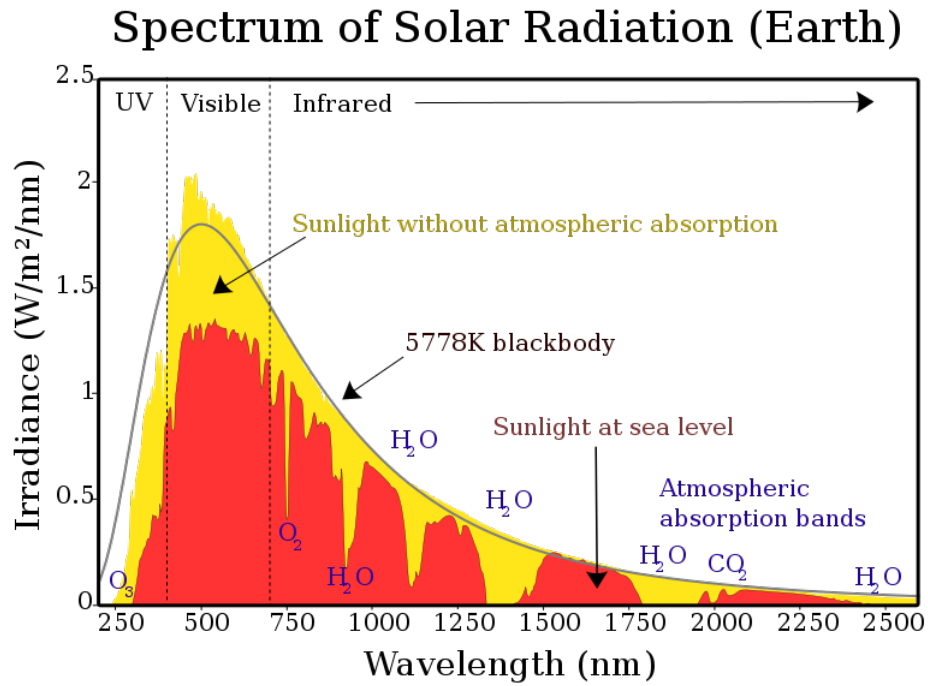
Figure 1.5: Solar irradiance spectrum reaching at the earth's atmosphere
[2]

The earth's atmosphere provides attenuation to the solar spectrum which depends on the atmospheric thickness (path length; PL) covered by the sun rays reaching the earth's surface. The air mass coefficient (AM) defines the direct optical path length through the Earth's atmosphere, expressed as a ratio relative to the path length covered vertically upwards, i.e. at the zenith. The AM is used to characterize the solar spectrum reaching at the earth's surface after absorbing the solar radiation by the atmosphere. For a path length L through the atmosphere, and solar radiation incident at zenith angle z relative to the normal to the Earth's surface (Figure 1.5), the air mass coefficient (AM) is given by eqn.1.1, where L_0 is the path length at zenith (perpendicular to the Earth's surface) at sea level.
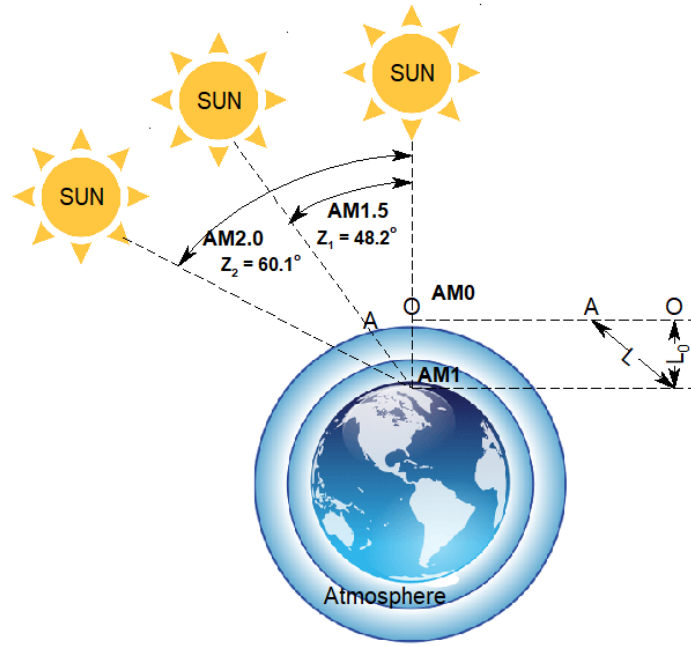
Figure 1.6: Solar radiation incident at angle z relative to the normal to the Earth's
surface representing the air mass coefficient (AM)

$$AM = L/L_0 \approx \frac{1}{cos z} \tag{1.1}$$

AM0, meaning 'zero atmospheres,' is the spectrum outside the atmosphere, and
AM1 is means that the sun is radiating directly perpendicular to the earth's surface
(z = 0°, relative atmospheric thickness = 1; (L/L_0), where AM1.5 means relative
atmospheric thickness (L/L_0) is 1.5 appears at z = 48.2°. Most of the earth's
population is living at the latitudes where the sun radiates its energy is located
at the angle is close to z = 48.2° throughout the year. Therefore overall annually
standard solar irradiation reaching at the earth's surface can be represented by
parameter AM1.5 which further can be opted as a standard potential parameter for
photovoltaic (PV) measurements of solar cells [3].

1.2.2   Harnessing of Solar Energy

Solar technologies can harness solar energy for a variety of uses, including power
generation, lighting or comfortable indoor environments, and domestic, commercial
or industrial water heating. A simple and elegant way to harness the energy of

the sun is photovoltaic (PV) technology. PV devices (solar cells) are unique in that they convert the incident solar radiation directly into electricity, making them robust, reliable and long-lasting without noise, pollution or moving parts. Solar cells have found in various application such satellites and space missions, solar car, solar water irrigation and solar power supply etc. This has led to a strong research interest for discovering new ways to use cheaper and more efficient techniques for solar energy.

1.3   Types of solar cell technology

In Photovoltaic (PV), photo means light and volt means to measure the electricity. In 1983, Becquerel reports the PV effect by observing a system where a current was flowing across two metal electrodes (Ag) immersed in an electrolyte solution upon light irradiation [4]. Based on the parameters; property of photosensitive material, components of PV system, optimum photo conversion efficiency available, and cost of PV power generating system, Martin Green has classified PV solar cells and their technology into three major categories described below.

1.3.1   First Generation of PV systems: 1970s

Silicon is one of the most abundant elements on earth (20 % of the earth's crust) and found in the form of silica sand (SiO_2). The abundant nature of silicon makes it an attractive material for semiconductor industry. These PV cells are used manufacture from crystalline silicon (c-Si) based semiconductor material suitable for PV applications, with energy band gap of 1.1 eV. Crystalline silicon solar cells are further classified into two main types on the basis of silicon wafers manufacturing process [5] shown in Table 1.1.

Table 1.1: Classification and performance of 1st generation solar cells

Sr.No	Type of c-Si solar cells	Silicon Wafer purity	Efficiency
1	Monocrystalline solar cells (Mono c-Si)	Highest-grade silicon	20-25 %
2	Polycrystalline (Poly c-Si)	Lower silicon purity	13-16 %

1.3.2 Second Generation of PV systems: 1980s

Conventional technologies employed for manufacturing crystalline silicon for PV application deal with various complex processing steps and required great deal of work. In the 2nd generation, a few micrometers thick of multilayer of semiconductor materials are deposited on low-cost substrates such as glass, flexible plastic or stainless steel while retaining the first generation of PV efficiencies. As a result, in order to absorb the same amount of sunlight, they need less semiconductor material to make due to its better light absorption coefficient. Furthermore, it is possible to pack thin films into compact and lightweight structures. Table 1.2 lists the commercially developed thin film solar cells [6,7]:

Table 1.2: Classification and performance of 2nd generation solar cells

Sr.No	2nd Generation solar cells	Efficiency
1	Amorphous silicon (a-Si)	6-7%
2	Cadmium Telluride (Cd-Te)	15.8 %
3	Copper-Indium-Selenide (CIS)	7-16 %
4	Copper-Indium-Gallium-Diselenide (CIGS)	20.3 %

1.3.3 Third Generation of PV Systems: 1990s

Though the theoretical upper limit for converting sunlight to energy is 33% for a conventional solar cell, the Carnot limit is approximately 95% for the same. This opens the possibility to increasing the efficiency of solar cells by two to three times if various strategies for raising efficiency without incurring excessive expenses can be implemented. There is a lot of research going on to develop low-cost semiconductor materials that can have their bandgap regulated for maximum performance, allowing to adjust the absorptive properties of the solar cell. This is what third generation solar cells have attempted for alternative materials to harvest solar energy. In recent years, new solar cell concepts have been introduced to enhance PV performance. Cells of the third generation are less commercially sophisticated 'emerging' techniques. Organic Photovoltaics (OPVs), Copper Zinc tin sulphide (CZTS), Perovskite solar cells, Dye-Sensitized Solar Cells (DSSCs), and Quantum Dot solar cells are all designed to combine the benefits of first and second generation systems. These

technologies are expected to play a significant role in fast-growing PV areas due to low-cost materials and easy manufacturing and classification with the performance measuring parameters are listed in Table 1.3 [8].

Table 1.3: Classification and performance of 3rd generation solar cells

Sr.No	3rd generation solar cells	Material based	Efficiency	Charge Injection Process	Advantage	Limitations
1	PV technology with concentrators	Silicon-based cells	20%-25%	At the interface of Si semiconductor junctions	Less PV material, hence less cost; Higher productivity throughout the day due to tracking	Lense fitted solar trackers increases architecture's complexity)
		Multi junction solar cells using III-V	40%	At interface of multiple junctions		
2	Dye Sensitized Solar Cells (DSSCs)	Dye adsorb on nano structured semiconductor material	5%-15%	From the excited photosensitive dye	Fabrication from cheap materials and low cost; Higher temperature performance; Low light performance	Very few dyes absorb broad solar spectrum.
3	Organic Solar Cells	Organic polymer materials for electron and transport layers	4%-5 (commercially), 6%-8% (laboratory)	Organic polymer materials	Lightweight and flexible	Low η and instability over time

1.4 Dye Sensitized solar cells (DSSCs)

An interesting development of solar cell technology today is that of new type of photochemical solar cell invented by O'Regan and Grätzel in 1991 which is known as Dye Sensitized Solar Cell (DSSC) [8]. It has attracted a lot of interest in recent years, in research as well as in industry. A DSSC is considered as potential photo electrochemical energy device with additional flexibility characteristics and a lower production cost due to its simple fabrication process [10].

$$S = S^+ + e \tag{1.2}$$

$$2S^+ + 3I^- = 2S + I_3^- \tag{1.3}$$

$$2S^+ + \frac{1}{2}I_3^- (electrolyte) = \frac{3}{2}I^- \tag{1.4}$$
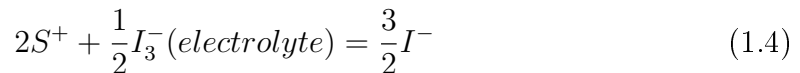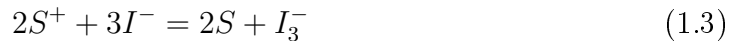
A DSSC consist of a nanoporous working electrode (WE: adsorbed by suitable photosensitive dye molecules), iodide(I^-)/triiodide(I_3^-) based redox electrolyte and a counter platinum (Pt) electrode. The adsorbed dye molecules get excited upon light illumination and injects electron in the conduction band (CB) of a working electrode as given by eqn. 1.2. The injected electron diffuses through electrode (inter-connected network of TiO$_2$ nanoparticles) until it reaches the back transparent conducting oxide (TCO) or recombines. The excited dye (S^+) on TiO$_2$ surface is then reduced back to its original state (S) by the redox electrolyte (I^-) shown by eqn. 1.3. This reduction process changes the equilibrium concentrations of redox electrolytes and creates a concentration gradient, which tend to diffuse I_3^- towards Pt electrode to preserve the equilibrium concentration of the redox electrolytes and completes the close circuit shown by eqn. 1.4. Charge transport between the rear Pt/TCO electrode and the dye molecules is accomplished by means of I^-/I_3^- redox electrolyte [10]- [12].

To obtain a higher efficiency (η), the key challenges are thus to enhance specific role of individual components of a DSSC viz. working electrode (WE), photosensitive dye, counter electrode (CE), an electrolyte; the bulk interfaces and various complex processes occurring in a DSSC.

1.5   Motivation for the work

The conventional energy resources (petroleum, coal, natural gas, fossil fuel etc.) are present in limited quantity on the earth and are being used for a long time. Conventional energy resources are used extensively by mankind and its demand of usage is so high that the reserves have got depleted to a great extent. Fossil fuels (coal, petroleum, and gas) containing carbon dioxide (CO_2) and other greenhouse gases (climate change drivers) are primarily part of present and past energy systems. Fossil fuel depletion and its environmental effects contribute to raising global awareness of the immediate need to identify alternative renewable energy options in

order to fulfill the world's requirements to sustain a high quality of life. The main pillar for human well-being, economic growth and poverty alleviation is access to electricity. Ensuring that everyone has enough energy access is a continuing and pressing problem for global growth.

Very much exploitation and research for new power source has been done not only in the areas of nuclear power generation but also in the area of unlimited renewable energy sources such as solar power generation, wind power generation etc. Sustainable renewable energy development is considered to be one of the most critical scientific and technological problems facing humankind in the globe. The renewable energy sources like solar and wind have shown promise as possible cost efficient alternatives to fossil fuels. The Sun is the source of energy available to mankind which is pervasive, readily available and renewable. Unlike fossil fuels, which are found only in a few areas, solar energy is freely available in every part of the world. Thus, all countries can benefit significantly from solar energy, regardless of their geographical position. Compared to wind energy, the most effective and harmless energy source is solar energy.

Photovoltaic (PV) technology is a simple and productive method to harnessing the sun's energy to produce electricity. In addition with the Silicon (Si) based PV technology, one of the emerging solar cells based on natural and synthetic photosensitive dyes called as Dye sensitized solar cells (DSSC) which can be considered as subject of increasing interest in the PV field during the last few decades. Though a DSSC consists of multiple materials, yet it is a highly realized next-generation potential photovoltaic device that has been widely investigated due to its several advantageous competencies features like working even under a dim/low light and an achievable high value of efficiency (η) using a straightforward, cost-effective and eco-friendly manufacturing process.

1.6 Objectives

The key objectives of this thesis work are:

1. To fabricate the electrode and its characterization for physicochemical properties using different experimental techniques (XRD, SEM, BET).

2. To optimize the electrode parameters to achieve better photovoltaic performance for Dye sensitized solar cells (DSSCs).

3. To propose the new explanatory theoretical models or to improve the (incorporation of parameters) known models of DSSCs.

4. Analysis of various charge transport properties by Electro-chemical impedance spectroscopy (EIS).

1.7 Thesis Organization

The completed research work is compiled in the following chapters:

1.7.1 Chapter 2: Literature Review

Almost all the aspects focused on previous work relevant to the research study of Dye sensitized solar cells are put together in this chapter. It also consists of theoretical, realistic, and application-based assumptions as a result of previous studies on DSSCs. In order to compile information on the earlier research carried out in the field of DSSCs, a comprehensive literature survey is conducted along with its complete architecture. In addition to the analysis centered on working electrode scaling, various morphologies of nanoparticles and their structural effect on dye solar cell performance are also presented along with the different methods of synthesis. The complete set of drift and diffusion process coupled with continuity and Nernst equations are also presented and discussed to describe the working principle of the DSSC. The various characterization techniques in order to investigate the material, physiochemical and photovoltaic properties (J-V) of DSSC required for explain the performance is also included.

1.7.2 Chapter 3: Facile one-pot hydrothermal synthesis of nanorice-like TiO_2 for an efficient dye sensitized solar cell (DSSC)

In this chapter a highly crystalline TiO_2 powder consisting of morphologically rice-like nanoparticles is synthesized by a simple hydrothermal process using a premixture

of titanium isopropoxide, ethanol and aqueous ammonia. The PV performance of assembled DSSC is also compared with P25 based DSSC to analyse the charge transfer properties in order to investigate the impact of morphological and crystalline nature of the working electrode (WE).

1.7.3 Chapter 4: Optimizing photovoltaic efficiency of a dye-sensitized solar cell (DSSC) by a combined (modelling-simulation and experimental) study

In this chapter a comparative investigation involving experimental and modelling-simulation is carried out to maximize the photovoltaic conversion efficiency (η) of a DSSC device assembled using N719 dye, an iodide redox liquid electrolyte and TiO_2 electrode. The measured current density-voltage (J-V) characteristics under 1 sun condition of a pre-assembled DSSC is simulated in a tiberCAD based microscopic model (TCMM) along with single-diode based macroscopic model (SDMM). The calibrated model parameters are then utilized for predicting a maximum η of a DSSC belonging to an unknown electrode's thickness (L).

1.7.4 Chapter 5: Analysis of charge transport properties of dye-sensitized solar cell (DSSC) with TiO_2 working electrode by employing electrochemical impedance spectroscopy (EIS)

The theoretically modeled equations defining various bulk and interface impedances are incorporated with EIS spectrum analyzer software to fit the simulated EIS curves with experimentally measured EIS curves to evaluate the charger transfer and recombination properties of the assembled DSSCs (as mentioned in chapter 3). EIS fitting parameters investigated to study the impact of WE thickness on the charge transport properties of assembled DSSC.

1.7.5   Chapter 6:Conclusion and Future Work

Here the outcomes of the research work are summarised and concluded along with
its future aspects.

Chapter 2

Literature Review

2.1 Introduction

In 1991, O'Regan and Grätzel invented a new, functional version of TiO_2 (metal oxide) based dye-sensitized solar cells (DSSCs), which were previously unsuitable for real world applications. DSSCs can be scrutnized as potential photo-electrochemical energy device with additional flexibility characteristics and a low production cost due to its simple fabrication process.

2.1.1 Architecture of DSSC

DSSC has a sandwiched like architecture as show in Figure 2.1 includes the following key components which plays important role to achieve optimized photovoltaic (PV) performance.
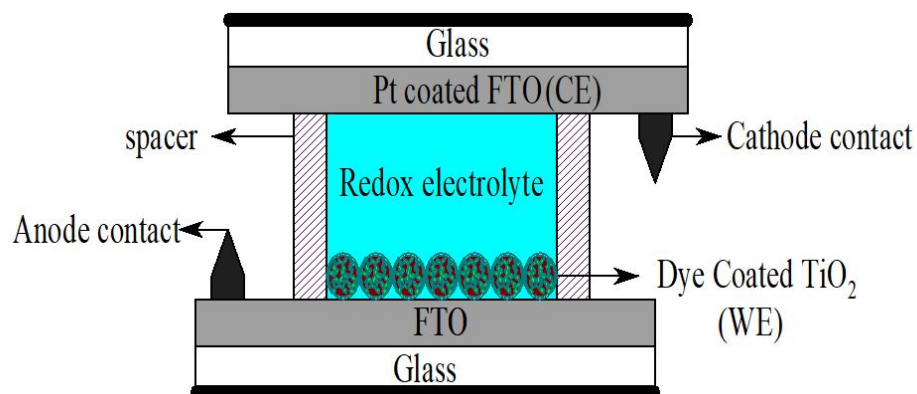
Figure 2.1: Architecture of Dye solar cell (DSSC)

2.1.1.1 Working electrode (WE)

A layer of nanostructured semiconductor (metal-oxide) material adsorbed with photosensitive dye of suitable energy band gap is deposited at the surface of glass coated on one side with a thin transparent conducting oxide (TCO) layer of fluorine-doped tin dioxide (FTO) or indium doped tin oxide (ITO). In comparison with other tested TCO, such as indium tin oxide (ITO), FTO demonstrated to have the higher work function (i.e. 4.9 eV in contrast with 4.8 eV of ITO); in addition, the best thermal stability, the least toxicity and low cost made FTO the most performing one for transparent conducting layer. The indium scarcity and the consequent increasing price the sensitivity to different environments both acids and basics and the patterning complications make FTO a better choice. Some more carbon-based materials (carbon nanotubes, nanomaterials, graphene) has been tested but values of sheet resistance and transmittance are below the requirement for application in PV (i.e. Rs = 10 Ωcm^{-2} and Tr = 90%).

The semiconductor (metal oxide) layer can be deposited by means of a variety of methods including spraying, spin coating, dip coating, screen printing or the simple doctor blade technique followed by sintering process at a temperature of 450 °C.

TiO_2 has all along been the preferred semiconductor in DSSCs by other metal oxides like ZnO, SnO_2 and Nb_2O_5. Apart from traditional pigment applications, nanocrystalline TiO_2 intrinsically possesses multifunctional attributes enabling it to be deployed in environmental photocatalysts (for treating polluted air or wastewater, self-cleaning windows, antimicrobial coatings); and in efficient electrodes for photovoltaic cells, photo-electrochromics and gas sensing devices.

In the natural environment, TiO_2 is mainly present in three crystalline forms: brookite, anatase (used in DSSC) and rutile. TiO_2 bandgap fits better (3.2 eV in anatase form; absorbs only below 388 nm) with the most successful commercial dyes allowing an efficient electron injection; moreover, it permits a higher dye loading due to the high surface area. Lower chemical stability and higher dark current of rutile form made it less efficient than anatase form. The WE is composed of a mesoporous layer of TiO_2 nanoparticles (10-20 nm) on which the dye molecules are anchored. The high surface area of the particular mesoporous semiconductor (metal oxide) film is important for the efficient device performance, as it allows absorption

of the solar radiation by employing only a monolayer of adsorbed photosensitive dye. Usually, the metal oxide film (ex. TiO_2, ZnO) is deposited by the screen printing technique, a reproducible system, of easy application for large area device and for spreading out in the PV market.

2.1.1.2 Photosensitive Dye

It injects electrons in the semiconductor electrode (WE) upon illumination; the photosensitive dye is regenerated by the redox electrolytes. The adsorbed dyes act as light-harvesting intermediates in DSSCs; they absorb visible and near-infrared solar radiation and inject the resulting excited electrons into the semiconductor conduction band. After light absorption, the separation of the charge is normally initiated at dye/TiO_2/electrolyte interface. Generally, the overall performance of DSSCs also depends on photo sensitizers and electron-transfer kinetics across the interfaces. On the basis of accumulated knowledge of dyes used for DSSCs, the photosensitive dye molecule should posses the following characteristics to generate charge carriers and their injection in the CB of WE efficiently:

- Strong binding between dye molecules and TiO_2 nano particles by means of an anchoring group for efficient electron injection.

- Dye should absorb maximum portion of light spectrum and should also posses high molar extinction coefficient (ε, $M^{-1}cm^{-1}$) for efficient light harvesting with thinner TiO_2 electrodes.

- The lowest unoccupied molecular orbital (LUMO) of the dye should be located near the anchoring group and above the CB edge of the semiconductor electrode (usually TiO_2) to achieve efficient electron injection into the CB of TiO_2.

- The dye's highest occupied molecular orbital (HOMO) should lie below the redox mediator 's energy level to allow the oxidized dye to regenerate.

The above requirements can be fulfilled by controlling photophysical, electrochemical properties of the dyes and the molecular orientation and arrangements of dyes on the TiO_2 surface. Many polypyridine complex of transition metals and several molecules

such as porphyrins, phthalocyanins, vegetable and artificial bio-inspired pigments
have been investigated for being sensitizers for DSSC.

2.1.1.3   Redox electrolyte

The function of the redox electrolyte is to regenerate the oxidized dye molecules by
transferring the electrons from the counter electrode (CE) to the oxidized dye and
completes electric circuit by mediating electrons between WE and CE. There are two
kinetic limitations for a successful redox electrolyte, it must reduce the dye cation
before the dye cation recombines with an electron in the CB of TiO_2 and it should
not allow the oxidized form of redox ions to recombine with an electron in from the
CB of TiO_2. The dual criteria of fast dye regeneration and slow recombination place
a very challenging constraint on identifying effective redox systems.

Literature also reports that for efficient DSSCs, I_3^-/I^- based redox couple is a suit-
able choice of redox electrolytes. In order to avoid problems (like dye desorption,
solvent evaporation and sealing degradation) due to the liquid electrolytes several
non-traditional electrolytes like ionic liquids, quasi-solid state and solid state elec-
trolytes have been used in DSSC.

2.1.1.4   Counter electrode:(CE)

The role of CE is to catalyzing the reduction process of the oxidized form of redox
electrolytes by the back transfer of electrons, arriving from the external circuit, to
the redox system. It acts as cathode for the DSSC. The most used material for
making the CE is a thin layer of few nanometers of platinum (Pt) that is deposited
on the FTO coated glass and acts as a catalyst. In the last years, the research
effort was focused on testing carbon materials such as amorphous carbon, CNTs, or
graphite, GNPs, or graphene oxide (GO) for another material for CE preparation.
Necessary features for an efficient counter electrode are following:

- The charge-transfer resistance at the electrolyte and Pt CE interface must be
  low.

- The exchange current density must be high in order to have an efficient elec-
  trolyte generation

- High specific surface area

2.2   Working principle of DSSC
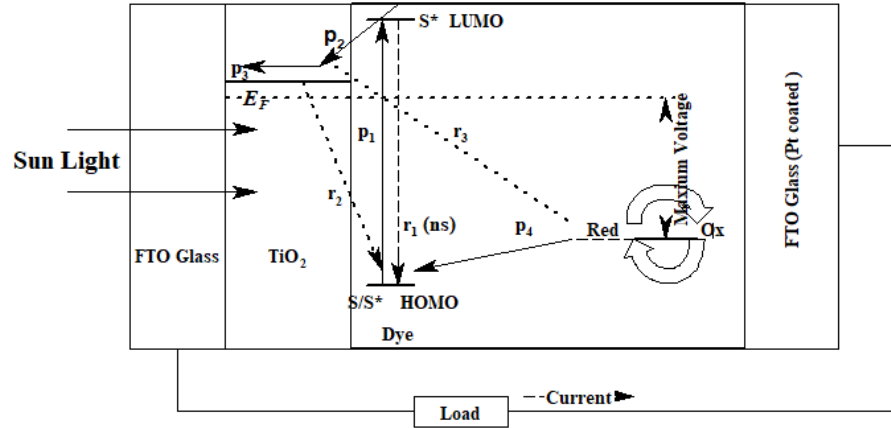
Figure 2.2: Energy band diagram of DSSC and various generation and recombination kinetics

From the Figure 2.2 it can be depicted that the adsorbed photosensitive dye molecules get excited (path p_1) upon light illumination from its ground state (S) to its excited state (S*) as given by eqn. (2.1). Charge separation occurs through photoinduced electron injection (path p_2) from (S*) into the CB of the WE (semiconductor layer of metal oxide, TiO$_2$), which results in the oxidation of the dye (S$^+$) as given by eqn. (2.2). The injected electron diffuses through electrode (interconnected network of TiO$_2$ nanoparticles) until it reaches the back FTO glass (path p_3) or recombines (path r_2, r_3). The excited dye (S$^+$) anchored on TiO$_2$ surface is then reduced back to its original state (S, through path p_4) by the redox electrolyte (I$_3^-$/I$^-$) as shown by eqn. (2.3). This reduction process changes the equilibrium concentrations of redox electrolytes and creates a concentration gradient, which tend to diffuse towards Pt electrode (CE) to preserve the equilibrium concentration of the redox electrolytes and completes the closed circuit shown by eqn. (2.4). Charge transport between the CE and the dye molecules is accomplished by means of iodide /triiodide redox electrolyte.

$$S(dye) + h\upsilon = S^* \tag{2.1}$$

$$S^*(dye) = S^+(dye) + e_{cb}(TiO_2) \tag{2.2}$$

$$2S^+(dye) + 3I^- = 2S(dye) + I_3^- \tag{2.3}$$

$$e(Pt) + \frac{1}{2}I_3^-(electrolyte) = \frac{3}{2}I^- \tag{2.4}$$

Excited dye molecule may relax directly to its ground state (S) by the electron from LUMO to HOMO level through recombination path r_1 (Figure. 2.2) as given by eqn.(2.5) and this process may be responsible for the electron loss but the electron injection rate constant (for path p_2) is 1000 times to dye relaxation rate constant (for path r_1) and dye relaxation can be neglected for electron loss mechanism. CB electrons may be captured by oxidized dye-molecules through recombination path r_2 and given by eqn. (2.6). The neutralization of excited dye should ideally occur via the redox species only and since the dye neutralization rate constant in 100 times higher than conduction band electron captured rate so we can also neglect this electron loss process. CB electrons may also be captured by of the electrolyte (see Figure. 2.2) by following recombination path r_3 as given by eqn. (2.7) and can be considered as dominant path of electron capturing.

The loss of the photoinjected electrons from any recombination process leads to degrade the PV performance of the DSSC. In principle for efficient DSSCs, the regeneration of the dye by I^- ions should be much faster than the recombination of electrons.

$$S^+(dye) + e = S(dye) \tag{2.5}$$

$$S^+(dye) + e_{cb}(TiO_2) = 2(dye) \tag{2.6}$$

$$I_3^-(electrolyte) + 2e_{cb}(TiO_2) = 3I^- \tag{2.7}$$

Indeed, understanding the kinetics of charge-transfer processes is fundamental in order to select the right materials for the optimization of the DSSC structure.

2.3   Techniques for Characterization of DSSC

The DSCC can be characterized to investigate the material properties of each key
component or as complete set of solar cell:

2.3.1   For complete DSSC

In this characterization technique, the final assembled DSSC is considered as a main
sample to analyze its performance.

2.3.1.1   Incident photon-to-current conversion efficiency (IPCE)

IPCE is a calculation of the solar cell's efficiency at various wavelengths to transform
the incoming photons to photocurrent. When illuminated by monochromatic light,
it is achieved by calculating the solar cell's net photocurrent. The IPCE is computed
as the number of electrons generated by irradiation in the external circuit divided by
the number of incident photons and is calculated by using the following eqn. (2.8),
where J_{SC} (mAcm^{-2}) is the short circuit current density generated by the monochro-
matic light; λ (nm) and ϕ_{ph} (mWcm^{-2}) are the wavelength and the incident light
intensity of the monochromatic light, respectively. IPCE can also be expressed as
the product of light-harvesting efficiency (LHE (λ)), the quantum yield of electron
injection ($\Phi_{inj(\lambda)}$), the efficiency of regeneration ($\Phi_{reg(\lambda)}$) and the efficiency dye of
collecting the injected electron ($\Phi_{coll(\lambda)}$) at the back contact or FTO. The LHE (λ)
can be expressed as $LHE(\lambda) = 1 - 10^{ABS(\lambda)}$, where ABS($\lambda$) is absorbance of the
dye adsorbed on nanocrystalline TiO$_2$ as given by eqn. (2.9). The equations (eqn.
2.8-2.9) emphasize the direct relation between the light absorption properties of the
dye, the amount of adsorbed dyes on the TiO$_2$ surface, $\Phi_{inj(\lambda)}$ and the $\Phi_{coll(\lambda)}$ on
the IPCE of the DSSCs. The maximum IPCEs for DSSCs are limited to 80-90 %
range; they do not reach 100 % experimentally, probably due to the reflection and
absorption losses (10-15 %) of the TCO glass.

$$IPCE(\%) = \frac{1240}{\lambda\phi_{ph}}J_{SC}.100 \tag{2.8}$$

$$IPCE(\lambda) = LHE(\lambda)\Phi_{inj(\lambda)}\Phi_{reg(\lambda)}\Phi_{coll(\lambda)} \tag{2.9}$$

2.3.1.2 Current density voltage characteristics (J-V)

J-V characteristics are monitored under the standard intensity of illumination (AM 1.5 G, 100mWcm^{-2}) by applying an external voltage between the WE and CE by tracing the current for a given points of external voltage. J-V curve can also be measured under dark conditions (zero light intensity) to analyse the recombination process taking place inside the cell.

2.3.1.3 Electro Chemical Impedance spectroscopy (EIS)

EIS is an effective technique for characterizing the electrical properties across the bulk and the interfaces of materials such as for DSSC to analyse the charge transport properties at TiO$_2$/electrolyte interface, CE/electrolyte interface etc and inside the bulk of TiO$_2$ electrode.

2.3.2 Characterization of DSSC components

2.3.2.1 UV-visible spectroscopy

UV-vis spectroscopy is a widely used technique for analyzing dyes and their ability to absorb the photons at different wavelengths. In this technique, a front side of the sample is irradiated with an intensity of UV-Vis (ultraviolet visible) light and the intensity at the back side of the sample (see Figure. 2.3) is measured. Absorbance is defined by eqn. (2.10), where I$_o$ is the intensity of light at the front side of the sample and I is the intensity to the detected at the back side of the sample. Transmission (T) reflects how much light intensity is transmitted by the sample instead of absorbed and defined by eqn. (2.11). Absorbance (A) is related to the concentration of the sample (C), the molar extinction coefficient (ε),and the path length of the light travelled (L) which are expressed by Lambert Beers law and given by $A = C\epsilon L$. Moreover the combined Lambert beers law and UV-vis spectroscopy can be used to investigate the dye coverage (molcm^{-2}) on the TiO$_2$ nanoparticles.

$$A = log_{10}\frac{I_o}{I} \tag{2.10}$$

$$T = \frac{I_o}{I} = 10^{-A(\lambda)} \tag{2.11}$$
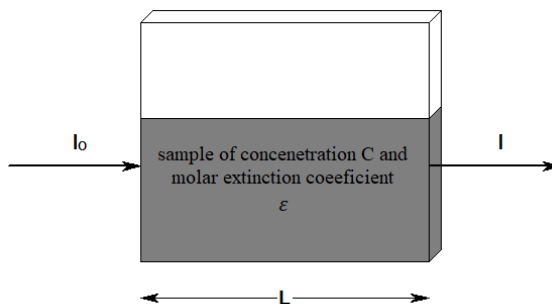
Figure 2.3: Light illumination across the sample to measure the absorbance

2.3.2.2 Fluorescence spectroscopy

As a function of wavelength, fluorescence spectroscopy calculates the emitted photons upon illumination. Photons are absorbed and electrons excited to higher energy levels by illuminating molecules. Molecules emit photons of lower energy than the first absorbed energy when they relax down to the ground state. In DSSC, the difference between the level of the ground state and the excited level of a dye can also be considered as a possible component for the absorption of the solar cell, so the energy gap between the dye's LUMO and HOMO can be determined from the absorption intercept and the dye's fluorescence spectra.

2.3.2.3 X-ray Diffractometry (XRD)

XRD is a rapid analytical technique primarily used for phase identification of a crystalline material and can provide information on unit cell dimensions. This research method is carried out as a function of the outgoing direction by directing an x-ray beam at a sample and calculating the scattered intensity. The scatter, also known as a diffraction pattern, indicates the crystalline structure of the sample once the beam is separated. In order to describe the crystal structure that most likely produced the observed pattern, the Rietveld refinement method is then used. For DSSCs, XRD is employed to investigate the crystallinity (single or multi-crystalline structure) and phase (rutile, anatase and brookite) of the synthesized TiO_2 nanoparticles.

2.3.2.4 Transient absorption spectroscopy (TAS)

TAS is a pump probe technique by using a lazer diode (Nd:YAG) with a 10 ns pulse
width to analyze and investigate kinetics of DSSCs in order to estimate the dye
regeneration rate constant and the time constants for the dye regeneration over any
instant of time. Decay characteristics achieved by TAS technique is further used to
measures the decay of the absorption of the oxidized dye with and without redox
couple to evaluate efficiency of the dye regeneration (η_{reg}), which is given by eqn.
(2.12), where k_{reg} and k_{rec} are the rate constants for the regeneration and recombi-
nation respectively. The time constants $\tau_{1/2(redox)}$ and $\tau_{1/2(inert)}$ are the half-times
with and without redox mediator, giving the regeneration and recombination half-
times.

$$\eta_{reg} = \frac{k_{rec}}{k_{rec} + k_{reg}} = 1 - \frac{\tau_{1/2(redox)}}{\tau_{1/2(inert)}} \tag{2.12}$$

2.3.2.5 Scanning electron microscopy (SEM)

SEM is a technique uses a focused beam of high-energy electrons to generate a
variety of signals at the surface of solid specimens. The electron-sample interaction
signals reveal sample information, including external morphology (texture), chemical
composition, and crystalline structure and orientation of the sample materials. Data
is collected over a selected area of the sample surface in most applications, and a
2-dimensional image is generated that shows spatial variations in these properties.
For DSSCs, SEM technique is applied to characterize the micro structural surface
morphology (shape, size) of TiO_2 nanoparticles coated on FTO glass.

2.3.2.6 Brunauer, Emmett and Teller (BET) Analysis

BET technique is applied to investigate the desired the physicochemical properties
of the material (synthesized or commercially available). The BET properties can
be measured by N_2 adsorption-desorption at 77 K. Specific BET surface area, pore
size and pore volume can b determined by N_2 adsorption isotherms using BET and
Barrett-joyner-Halenda (BJH) methods. For DSSCs, BET is applied to evaluate the
physicochemical properties of the TiO_2 nanocrystalline powder.

2.3.3 Photovoltaic (P-V) parameters of DSSCs

The P-V performance of any DSSC can be explained in terms of the parameters: (i)
photocurrent–voltage curve (JV curve), (ii) open-circuit voltage (V_{OC}), (iii) short-
circuit current density (J_{SC}), (iv) Fill factor (FF), and (v) overall conversion effi-
ciency (η). These photovoltaic parameters explained below:

2.3.3.1 Photocurrent voltage (J–V) curve

The J–V curves represent, in general, the most important and most direct charac-
terization method for DSSCs and for solar cells. A typical J–V curve is shown in
Figure. 2.4. Analysis of the J–V curves includes the determination of the following
parameters: V_{OC}, (J_{SC}), fill factor (FF), maximum power point (MPP, (V_{opt}) and
(J_{opt})); and overall conversion efficiency (η).
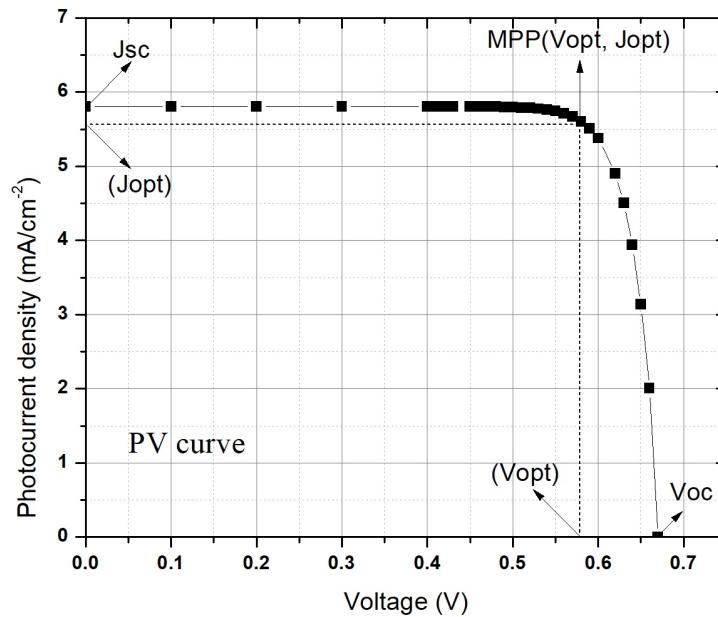
Figure 2.4: J-V characteristics of DSSC listing performance parameters

2.3.3.2 Open circuit photo voltage (V_{OC})

V_{OC} is usually measured when the current flow in the cell is zero (i.e. open circuited
condition, see Figure. 2.4) and defined as the difference in electrical potential be-
tween two terminals of a cell under illumination. The maximum V_{OC} of a DSSC
corresponds to the absolute difference between the Fermi level ($V_F = E_F/q$) of the

CB of TiO$_2$ and the redox potential ($V_{red} = E_{red}/q$) of the redox system, I$_3^-$/I$^-$, where E_F and E_{red} are the fermi levels of TiO$_2$ and redox electrolyte respectively.

2.3.3.3   Short-circuit photocurrent density (J$_{SC}$)

J$_{SC}$ (mAcm^{-2}) is measured for DSSC under irradiation at an applied potential of zero volt (i.e. short-circuited condition, see fig. 2.4). It is well associated with the interaction of photosensitive dye molecules and TiO$_2$ nanoparticles result in significant impact on absorption coefficient of dye and electrode injection process from LUMO level of dye to CB of TiO$_2$.

2.3.3.4   Maximum Power Point (MPP)

It represents maximum power density generated by the any solar cell. The points corresponding to MPP (mWcm^{-2}) on the PV curve are given by V$_{opt}$ (optimum voltage, V) and J$_{opt}$ (optimum current density, mAcm^{-2}) respectively and computed as $MPP = V_{opt}.J_{opt}$ (see fig. 2.4) The MPP majorly depends on the sharpness (slope) of non linear region of PV curve.

2.3.3.5   Fill factor (FF)

The fill factor (FF) of a solar cell is the ratio of the maximum power output ($MPP = V_{opt}.J_{opt}$) to the product of V$_{OC}$ and J$_{SC}$. This parameter indicates the deflection of the J-V characteristic from a square like curve as shown in Figure. 2.4 and expressed by eqn. (2.13).

$$FF = \frac{J_{opt}V_{opt}}{J_{SC}V_{OC}} \tag{2.13}$$

2.3.3.6   Photovoltaic efficiency (η)

The overall conversion efficiency of a DSSC is defined as the maximum output electrical power of the DSSC divided by the energy of the incident sunlight (I) on the active surface area of solar cell. This is also called as solar energy to electricity conversion yield. The overall η of the photovoltaic cell is calculated from J$_{SC}$ (mAcm^{-2}), V$_{OC}$, (V), the FF and the intensity of the incident light (ϕ_{ph}, mWcm^{-2}), using the eqn. 2.14

$$\eta(\%) = \frac{J_{opt}V_{opt}}{\phi_{ph}} = \frac{J_{SC}V_{OC}}{\phi_{ph}}.FF.100 \tag{2.14}$$

The efficiency is a function of J_{SC}, V_{OC} and FF of the DSSC. Consequently, improvement of the overall conversion efficiency is the result of the optimization of these three parameters. However, a gradual increase in the overall conversion efficiency has been recognized in the past decade. In order to achieve higher photovoltaic conversion efficiency, the key components of DSSC's architecture should be design and synthesize in order to achieve favorable photo physical and electrochemical performance.

2.4   Development in Photosensitizers

The role of dye as a photo sensitizer is unique in DSSC as compared to other solar cells. Dye increases the conversion η of the photo electrochemical cells with photo electrode (PE) of wide band gap semiconductors. The PE itself maybe in transparent to visible and infrared (IR) light spectrum; therefore dye is also one of the component which is responsible for driving the efficiency of the cell. The ability to absorb the wide light spectrum enhances the conversion of photons into electricity.

The techniques like molecular engineering of several organic dyes, metal complexes and natural dyes are widely studied and focused in order to enhance the role of dye for light absorption to improve the η of DSSC. The dye for DSSC are categorized and discussed below:

2.4.1   Complex dyes based on Metal-composites

Dyes composed of chromophores of ruthenium (Ru) complexes which are widely used for the DSSC applications as effective sensitizers [13]. Several complexes of Ru dye eg. Ru poly pyridyl complexes are used as a charge transfer sensitizers and have shown the $\eta \sim 11$ % under AM 1.5 (100 mWcm^{-2}) conditions. The improvement in the η is noticed because of their efficient charge transfer process and better absorption over a wide visible range [14].

The one of the famous Ru-complex photo-sensitizers is known N3 or red dye which

is developed by Grätzel and his group. Two other dyes reported in the literature
are N749 (black dye) and N719. These are most effective sensitizers and because
the carboxylate groups attracted to the bipyridyl moiety decrease the ligand π^* or-
bital's energy and further enhances the absorption spectrum (visible to near infra
red region) [15]- [19].

A new kind of ruthenium sensitizers, i.e., JK-91 and JK-92 are synthesized on sub-
stitution of one of the 2,2'-bipyridyl-4,4'-dicarboxylate groups in the sensitizer N719
into the conjugated bipyridine of the ancillary ligand to reach the η to 6.22 % and
6.75 %, respectively for DSSCs.

Researchers also synthesized a new Ru(II) sensitizer (A597) and describes its op-
tical, photo voltaic and electrochemical characteristics by employing it for DSSC
applications and investigated $\eta = 7.25$ % due presence of ligands (bipyridine and
thiocyanateco) to anchor the dye molecules at the TiO_2 surface.

DSSCs based on sensitisers containing supplementary bipyridine ligands (contains,
carbazole, fluorene, etc.) tethered to a hydrophobichexyl substituent were fabri-
cated and exhibit an impressive $\eta = 5.94 - 6.91$ % more than ($\eta = 6.36$ %) and
are shows comparable performance for dye N719 ($\eta = 7.13$ %) [20]. The impact
of ligand structure over photovoltaic performance (PV) of DSSC is also investi-
gated by designing and synthesizing three thiocyanate free cyclometalated Ru-II
complexes as sensitizers for absorbing near IR regions and producing η of 5.53 %,
3.81 % and 3.43 %, respectively [21]. Few of the PV parameters of DSSCs based on
metal complexes that have been evaluated as photosensitisers are listed in Table 2.1.

Table 2.1: PV parameters of DSSCs based on metal complexes that have been
evaluated as photosensitisers

S.No	Dye	J_{SC} mAcm^{-2}	V_{OC}(V)	FF	η	Reference
1	C101	5.42	0.74	0.83	11.3	[22]
2	N719	17.73	0.84	0.74	11.2	[23]
3	C106	18.28	0.74	0.77	10.57	[24]
4	C104	17.87	0.86	0.77	10.53	[25]
5	N749	20.53	0.72	0.7	10.4	[13]
6	IJ-1	19.2	0.74	0.72	10.3	[26]
7	Z910	17.2	0.77	0.76	10.2	[26]
8	N3	18.2	0.72	0.73	10	[26]
9	N945	16.5	0.79	0.72	9.6	[27]

10	HRS-1	20	0.68	0.69	9.5	[28]
11	AB-1	19.1	0.66	0.72	9.1	[29]
12	SJW-E1	21.6	0.66	0.62	9.02	[30]
13	K73	17.22	0.74	0.69	9	[31]
14	CYC-B7	17.4	0.78	0.65	8.9	[32]
15	LXJ-1	16.5	0.71	0.74	8.8	[33]
16	HRS-2	17.47	0.69	0.71	8.65	[34]
17	K8	18	0.64	0.75	8.64	[35]
18	KC-8	17.12	0.67	0.72	8.3	[36]
19	Z955	16.37	0.7	0.69	8	[37]
20	CYC-B11	16.1	0.71	0.69	7.9	[38]
21	K51	15.4	0.73	0.68	7.8	[31]
22	KC-7	16.11	0.67	0.7	7.62	[36]
23	KC-6	15.47	0.67	0.71	7.42	[36]
24	Z907	14.6	0.72	0.69	7.3	[26]
25	K19	14.61	0.71	0.67	7	[39]
26	HC-1	13.9 1	0.52	0.57	5.2	[40]
27	DS	11.9	0.66	0.68	5.1	[26]

2.4.2   Metal-free organic dyes

Metal-free organic donor–acceptor (D–A) dyes have high extinction coefficients to
absorb more irradiation with less dye coating thickness [41]. This makes organic
dye suitable for TiO_2 films. More over due to their ecofriendly nature and relatively
low cost, research has been grown to synthesize metal free organic novel sensitizers
in recent years. Due to phototherapeutic and photochemical application, many
organic dyes, such as perylenes, indoline dyes, hemicyanine dyes carbazole dyes
triphenylamine dyes, porphyrin dyes, coumarin dyes, and phthalocyanine dyes, have
been intensively investigated as sensitizers and some have achieved efficiencies more
than 10 % [42]. Employing co sensitization with an organic dye (NKX 2553 or
D131) to improve the η of black dye based DSSCs. In addition to this the η was
further enhanced up to 11.6 % by employing co adsorbent (deoxycholic acid, DCA)
in DSSC [43]. A new metal-free organic dye is also synthesized for DSSCs with η of
5.1 %.

2.4.3 Natural dyes

The promising alternative photosensitizes for DSSCs are natural dyes because it is cheap, versatile, plentiful, and sustainable. Natural dyes exhibit very less consumptions of noble metals which make them important are of study for research. Flowers, leaves and fruits have different colors in nature producing pigments for DSSC application [44]. Many pigments have been investigated as listed in Table 2.2. Pigment molecules and dyes, which are primarily derived from plants (sometimes from animals or minerals) with or without chemical treatment, are natural colourants. If it is possible to manufacture an alternative dye, such as a plant dye, as well as ruthenium complex dyes or organic dyes, it would be of interest for both economic and environmental reasons. A aim of research on plant-based dyes for photo electrochemical solar cells is to produce a dye that can be used with reasonable efficiency for the same purposes as ruthenium dyes. Many natural dyes, including anthocyanins [45], tannins [46], carotenoids, cyanines [47], flavonoids [48] and chlorophylls [14]- [49], have been used as sensitizers in DSSCs.

Table 2.2: PV parameters of natural dye based DSSCs

S.No	Dye	J_{SC} mAcm^{-2}	V_{OC} (V)	FF	η (%)	Reference
	Flowers					
1	Begonia	0.63	0.53	72.2	0.24	[50]
2	Hibiscus sabdariffa L	1.63	0.5	0.57	0.37	[51]
3	Hibiscus rosasinesis	5.45	0.39	0.54	1.14	[26]
4	Red Bougainvilleaglabra	2.34	0.26	0.74	0.45	[52]
5	Ixora	6.26	0.35	0.44	0.96	[53]
	Fruits					
6	Tangerinepeel	0.47	0.59	63.1	0.28	[50]
7	Raspberry	0.26	0.42	64.8	1.5	[26]
8	Cheries	0.46	0.3	38.3	0.18	[26]
9	Blue berry	0.48	0.61	0.58	0.16	[26]
10	Hylocereuspolyrhizus (Dragonfruit)	0.2	0.22	0.3	0.22	[54]
11	Wild Sicilian Prickly Pear	8.2	0.38	0.38	1.19	[55]
12	Ivy gourdfruits	0.24	0.64	0.49	0.09	[56]
13	Melastoma malabathricum	1.5	0.43	0.43	1.37	[57]
14	Canarium odotophyllum	2.45	0.38	0.62	0.59	[54]

15	Nephelium lap-paceum	0.38	0.4	0.35	0.56	[26]
	Leaves					
16	Herba artemisiaesco-pariae	1.03	0.48	68.2	0.34	[50]
17	Vernoniaamygdalin	0.07	0.34	0.81	0.69	[26]
18	Spinach	0.47	0.55	0.51	0.13	[45]
19	Festuca ovina	1.18	0.54	0.69	0.46	[26]
20	Bougainvillea	3.23	0.5	0.41	0.61	[58]
21	Sweet potatoleaves	0.57	0.59	0.41	0.14	[26]
22	Brassicaolercea (Redcabbage)	0.5	0.37	0.54	0.13	[26]
23	Punica granatum (Pomegranate)	2.05	0.56	0.52	0.59	[54]
24	Shiso	3.56	0.55	0.51	1.01	[26]
25	Jathopha curcas Linn (Botuje)	0.69	0.05	0.87	0.12	[26]
26	Lawsonia inermis (Henna)	1.87	0.61	0.58	0.66	[26]
27	Ficus reusa	7.85	0.52	0.29	1.18	[59]

2.5 Development in electrolytes

The electrolyte is considered as performance driving components in Dye sensitized solar cells (DSSCs). It provides inner charge transport between electrodes and effectively regenerates the dye and itself during operation of DSSC. Moreover it has immense influence on the photo conversion efficiency (η) and stability of the device for long duration. In order to achieve rapid dye regeneration, iodide should be present in sufficient concentration or diffusion of iodide ion should be fast. The non viscous electrolyte solution provides free path for diffusion of electrolyte ions effectively. Hence, required low electrolyte concentration is enough for dye regeneration for non viscous electrolyte solutions. For viscous electrolyte solutions, high concentration of electrolytes hinders the diffusion process results decreases the dye regeneration rate. An optimized viscosity for electrolyte solution is required for proper diffusion of iodide to achieve better dye regeneration rate.Transport of triiodide to the counter electrode is mostly driven by diffusion; can be limited by lower concentration of triiodide or by high viscous solvent causes an over potential results lowering the open circuited voltage (V_{OC}) of the DSSC.

The performance of the DSSC is determined by its Photovoltaic parameters (PV) parameters (J_{SC}, FF, V_{OC}, η) which are significantly affected by the type electrolytes and their interaction with electrodes in DSSCs. For instance PV parameters can be significantly affected by redox couple transport process, diffusion of electrolytes and the charge transfer resistance across electrolyte/electrode interface and redox potential of the electrolyte respectively. Wide research has been carried out on the electrolytes in order to improve the PV performance of the DSSCs [60]. Various electrolytes utilized to develop the DSSCs are further classified on the basis of their compositions, physical states and formation mechanisms named as liquid electrolytes [61]- [62], quasi-solid electrolytes [63]- [64] and solid-state conductors [65].

2.5.1 Liquid electrolytes

In 1991, O'Regan and Gratzel pioneered a successful DSSC using a very rudimentary liquid electrolyte (LE) consisting of an organic solvent and a dissolved I^-/I_3^- redox pair without additives. Liquid electrolytes (LEs) should be chemically and physically stable in DSSCs. Due to the excellent characteristics, such as smooth preparation, better conductivity, superior wetting property at electrode and electrolyte interface and low viscous property (for efficient redox reactions), liquid electrolytes have been continuously preferred for the DSSC applications to produce efficient devices as listed in Table 2.3.

Table 2.3: PV performance of DSSCs based on liquid electrolytes using ionic liquid as solvents

Electrolyte composition	Dye	J_{SC} mAcm^{-2}	V_{OC} (V)	FF	η (%)	D(I_3^-) (x10^{-7} cm^{2}s^{-1}	Ref.
0.2 M I$_2$, 0.5 M NMBI in PMImI/EMImTCM (vol ratio 1/1)	Z907Na	12.8	0.752	0.764	7.4	6.3	[66]
0.2 M I$_2$, 0.14 M Guan-SCN, 0.5 M TBP in PMImI/EMImSCN (vol ratio 13/7)	Z907	13.3	0.746	0.72	7.0	2.95	[67]
0.1 M I$_2$, 0.1 M LiI, 0.45 M NMBI in PMImI/EMImDCN (vol ratio 13/7)	Z907	12.8	0.707	0.727	6.6	4.4	[68]

0.2 M I$_2$, 0.5 M NMBI, 0.1 M GuanSCN in PMImI/EMImB(CN)4 (vol ratio 13/7)	Z907Na	13.55	0.736	0.698	7.0	3.42	[69]
0.2 M I$_2$ in PMImI/EMImTFSI/ EMImTf (vol ratio 2/2/1)	D149	D149	0.612	0.676	6.67	2.48	[70]
0.2 M I$_2$, 0.5 M NMBI in PMImI	K19	13.07	0.678	0.71	6.27	1.9	[71]
0.2 M I$_2$, 0.5 M NMBI, 0.12 M GuanSCN in PMImI/EMImSCN (vol ratio 13/7)	K19	13.99	0.707	0.71	7.05	3.0	[72]
1 M DMII, 0.15 M I$_2$, 0.5 M NBB, 0.1 M GuNCS, 50 mM NaI in BN	C106	17.9	0.733	0.76	10	4.6	[73]
1 M DMII, 0.15 M I$_2$, 0.5 M NBB, 0.1 M GNCS in MPN	C103	17.51	0.771	0.709	10	–	[74]

2.5.2 Quasi solid state liquid electrolytes (QSSELs)

The DSSC achieves great growth by using LEs as charge transporters. The use of
LEs, however, causes some practical problems, such as solvent leakage and volatiliza-
tion, dye photo degradation and desorption, CE corrosion and cell sealing for long
time application. These kinds of drawbacks can be solved by employing QSSELs in
DSSCs. Although the efficiencies of DSSCs with QSSELs are often lower than those
of DSSCs with LEs, due to improved stability and better sealing efficiency, QSSELs
can become viable alternatives to LEs [63], [75], [64]. QSS or semisolid-state is a
special state between solid and liquid-state substances. Few of the DSSCs based on
QSSELs are listed in Table 2.4

Table 2.4: PV performance of DSSCs based on QSSELs

Electrolyte composi-tion	Dye	J$_{SC}$ mAcm^{-2}	V$_{OC}$ (V)	FF	η (%)	σ mScm^{-1}	Ref.
0.12 M I$_2$, 0.5 M KI, 0.9 M BMIMI, in GBL, 35 wt % of PVP	N3	15.72	0.626	0.55	5.41	2.3	[72]

CH$_3$CO$_2$H, TMOS, 0.5MPMImI, 0.04 mM-NMBI, 20 mM I$_2$ in PC/Triton (mol ratio 4/1)	N3	12.9	0.65	0.66	5.4	0.36	[76]
0.1M I$_2$, 0.5 M NBB, 0.1 M GNCS, EMII/PMII/EMISCN (vol ratio 6/6/7) in poly[BVIm][HIm][TFSI] (25 wt %)	N3	12.92	0.676	0.678	5.92	5.83	[77]
PMAPII (16.wt %) 0.05 M I$_2$, 0.05 M TBP in GBL	TBA	14.7	0.79	0.70	8.12	4.9	[78]
0.1 M LiI, 0.45 M NMBI, 0.4 M DMPII, PEO/PVDF-HFP (2:3 wt %) 20 wt % in MeCN	N719	14.12	0.68	0.72	6.97	21.18	[79]
0.1 M LiI, 0.9 M EMII/SN, 0.1 M I$_2$, 0.5 M TBP in ACN/MPN (vol ratio 1/4)	N719	14.8	0.674	0.75	7.46	1.272	[80]
0.5 M LiI, 0.05 M I$_2$, 0.5 M NMBI, 10 wt % P(MOEMImCl) in HMImI/EMImBF$_4$ (vol ratio 2/1)	N719	15.50	0.618	0.64	6.1	0.4	[81]
poly(1-ethyl-3-(acryloyloxy)hexylimidazolium iodide) (PEAII)	N3	9.75	0.838	0.65	5.29	0.363	[82]
poly((1-(4-ethenylphenyl)methyl)-3-butyl-imidazolium iodide) (PEBII) in AN (10 wt %)	N719	18.1	0.643	0.51	5.93	0.2	[83]

Macromolecular or supramolecular nanoaggregate systems characterized by remarkable ionic conductivity, typically higher than 10^{-7} S for DSSCs, usually higher than 10^{-3} S, are termed as QSSELs. Moreover QSSELs have both the solid cohesive property and the liquid diffusive property, namely along with greater long-term stability than LEs. Other than DSSC applications, QSSELs are also employed in other electrochemical and electronic applications, such as fuel cells, actuators and sensors, secondary batteries, fuel cells, electrochromic displays and supercapacitors, and because of their exceptional properties [84]- [94].

For the preparation of QSSELs, three methods are sometimes used: (i) solidification of LEs to form thermoplastic polymer electrolytes or thermosetting polymer

electrolytes by using organic polymer gelators; (ii) solidification of LEs to form
composite polymer electrolytes by using inorganic gelators, such as SiO_2, nanoclay
powder; (iii) by using organic polymer or inorganic gelators for the solidification of
ionic LEs [62]- [95].

2.5.3 Quasi state transport materials (SSTMs)

Stability is also the key issue for QSSELs, as the electrolytes still contain solvents
and are usually thermodynamically unstable. Solvent exudation is inevitable during
long storage or exposure to air. All SSTMs have more advantages over LEs and
QSSELs in this respect, especially in the actual large-scale application of DSSCs.
Several materials, including ionic conductors, inorganic hole-transport materials and
organic hole-transport materials have been developed to substitute LEs or QSSELs
with SSTMs [96]- [97].
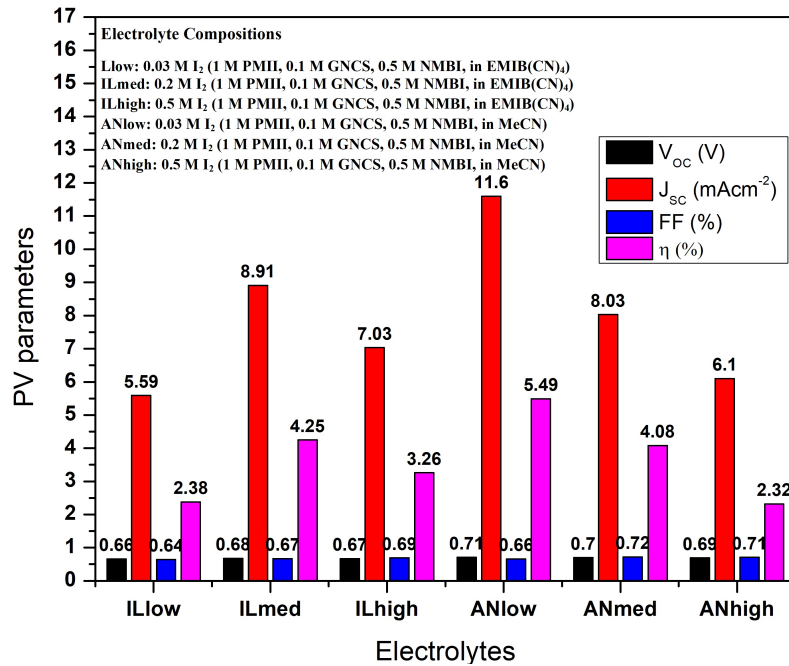
Figure 2.5: PV performmance of DSSC based on electrolyte compositions [98]

Moreover few of the researcher's work also investigated the effects on DSSCs based
on low-viscous, binary ionic liquids (IL) and organic liquid solvents with varying
iodine concentrations ($[I_2]$) and iodine-to-iodide ratios in electrolytes. Using inter-
mediate and low $[I_2]$ in ionic liquid-based and acetonitrile (AN) based electrolytes
respectively; optimum J_{SC} and η were achieved. Photo electrochemical and Raman-

spectroscopic measurement results show that the optimal [I_2] needed in these two types of electrolytes is influenced by both I_3^- mobility and chemical availability. The higher [I_2] required for the IL-based electrolytes partly compensate for these effects, although negative effects from higher recombination losses and light absorption of I_2 containing species start to become significant [98].

2.6 Synthesis routes for Metal Oxides (TiO$_2$)

2.6.1 Circular shape TiO$_2$

By the sol-gel process, hierarchically ordered titanium dioxide nanoparticles were successfully synthesised. Powder X-ray diffraction, UV-Vis spectroscopy, (BET) Brunauer Emmett Teller method, Barrett Joyner Halenda (BJH) analysis, field emission scanning electron microscopy, high-resolution transmission electron microscopy and energy-dispersive X-ray analysis were subjected to the synthesized nanoparticles.

The pattern of powder X-ray diffraction shows that the particles obtained are of good crystallite quality in the anatase process. The isotherms of nitrogen adsorption and desorption show that the prepared material has an area of 31,71 m^{2}g^{-1} and the study of pore size distribution shows that the average pore diameters of mesoporous TiO$_2$ nanostructures are 7.1 and 9.3 nm. In the ultraviolet field, the UV-Vis DRS spectrum shows that the TiO$_2$ nanoparticles are absorbed. The nanoparticles' optical band gap is 3.2 eV. Morphological experiments indicate that the particles' morphology is circular in shape. Energy-dispersive X-ray spectrum study confirmed the elemental compositions of TiO$_2$ nanoparticles. With open circuit voltage (V$_{OC}$), short circuit current (I$_{SC}$) and fill factor (FF) of 0.607 V, 13.206 mA cm^{-2} and 42.56 %, the conversion efficiency of the solar cell was 3.415 % [99].

2.6.2 TiO$_2$ microsphere

For a lot of applications, especially in the field of solar cells, TiO$_2$ microspheres (MS) are of great interest. TiO$_2$ microsphere based solar cells often exhibit superior photovoltaic performance due to their unique microstructure and light scattering

effect. Hence it is important to explore new suitable TiO_2 microspheres for high-efficiency solar cells. The simple one-pot solvothermal method for synthesizing TiO_2 microspheres using acetone as a solvent is synthesized by the researchers. The TiO_2 microspheres as prepared are made of densely intertwined nanocrystals and have a high specific area of up to 138.47 m^2g^{-1}. The TiO_2 microsphere-based DSSC, like the photoanode, provides greater dye loading and light adsorption capability, longer electron lifetime, resulting in higher short circuit current value and superior efficiency of power conversion compared to Dyesol (DSL) 18 nm TiO_2 nanoparticles paste. Finally, the DSSC based on the TiO_2 microsphere was optimised by adding a sublayer of TiO_2 nanocrystals and post-treatment $TiCl_4$, giving a 10.32 % high power conversion efficiency. Comparison of the photovoltaic properties measured under 1 sun illumination and dye adsorption capacities for TiO_2 MS and DSL-18 based DSSCs is listed in Table 2.5 [100]

Table 2.5: TiO_2 MS and DSL-18 based DSSCs PV performance [100]

Cell	Thickness	Dye loading $(10^{-8}molcm^{-2})$	J_{SC} $mAcm^{-2}$	V_{OC} (V)	FF	η
TiO_2 MS	7 μm	9.69	13.89	0.761	73.77	7.80
DSL-18	7 μm	8.82	11.88	0.759	74.81	6.76

2.6.3 Spherical TiO_2

The spherical titanium glycolate precursors are subjected to a rapid microwave treatment via ethylene glycol-mediated sol gel process to synthesize porous anatase TiO_2 spheres ranging from 150 to 250 nm in size. It explored the effects of different experimental conditions on the formation of precursors of titanium glycolate and final spheres of TiO_2. A dye-sensitized solar cell (DSSC) assembled as photoanodes with the as-synthesized porous TiO_2 spheres exhibits 5 % energy conversion efficiency, almost 40 % higher than that provided by the standard commercial Degussa P25 TiO_2 nanopowders [101].

2.6.4   TiO$_2$ Anatase powder

Dye sensitized solar cells (DSSC) may be an alternative to solar cells based on silicon that is economically feasible and technically simpler. The most effective photoelectrode for DSSC is known to be films of nanocrystalline titanium dioxide (TiO$_2$). TiO$_2$ anatase phase powder, synthesized in an acidic environment, was used for this analysis. The average nanoparticle diameter was nearly 20 nm and the surface area of the BET was 64.68 m^2/g. By varying the proportion of TiO$_2$ powder, α-terpineol and ethyl cellulose (EC) in their composition, different TiO$_2$ pastes were prepared. Using the doctor blade, the TiO$_2$ paste was cast on the fluorine doped tin oxide (FTO) coated glass surface to prepare TiO$_2$ film photo-electrodes. By comparing the conversion efficiencies of the DSSCs produced with the 18 µm thick photo-electrode, the composition of the paste ingredients was optimized. The outcome of this study may be crucial for the easy preparation of reliable TiO$_2$ paste for use in DSSC. Composition of different pastes of TiO$_2$ nanoparticles used for the fabrication of DSSC as listed in Table 2.6. The pure EC content was only 15 % in the EC gel whereas rest of the 85 % was α-terpineol [102].

Table 2.6: PV performance of DSSC prepared from different TiO$_2$ by varying proportion of TiO$_2$ powder,α-terpineol and ethyl cellulose (EC) in their composition [102]

S.No	TiO$_2$	ethyl cellulose (EC)(wt.%)	Total ethyl cellulose (EC)(wt.%)	Total α-terpineol (wt.%)	Pure EC (wt.%)	η (%)
1	20	20	60	77	3	4.6
2	23	17.5	59.5	74.38	2.63	5.18
3	26	15	59	71.75	2.25	7.27
4	29	12.5	58.5	69.13	1.88	6.25
5	32	10	58	66.5	1.5	5.1

2.7   Improvements in photoanode

The main function of the WE is to harvest the incident photon efficiently and to provide transportation path for the charge carriers with minimum recombination centers. WE should also capable to bind the dye molecules at TiO$_2$(metal oxide)

surface in order to collect photo generated efficiently at near the Dye/TiO_2 interface upon light illumination. The metal oxide layer of WE should inherit the following characteristics to achieve excellent electron generation and transportation process.

- Surface area of metal oxide nano particles should be large in order to increase the dye loading capacity of WE

- Follow the transparency for visible spectrum (400nm – 700 nm) so that losses of incident photon can be minimized

- LUMO level of the dye molecules must lie above the CB of the TiO_2 (metal oxide) for electron injection efficiently

- Sufficiently high electron mobility to achieve effective electron transportation process across network of TiO_2 nano particles

- Inactive to electron recombination across TiO_2/electrolyte interface

The photoanode is considered as a imperative component of DSSC for anchoring dye molecules for electron transfer upon light illumination. The better electron transport is required to minimize the electron recombination to obtain efficient DSSCs. Faster electron injection process (dye to TiO_2 CB) results high performance DSSCs with rapid electron transport. An efficient research has been continuously carried on high specific surface area, light scattering effect, enhanced charge-collection η and rapid charge transport for improving the performance of TiO_2 based photo-electrodes. The spatial distribution of semiconducting particles of WE such as microstructure, particle size, pore size and porosity plays an vital role in modulating the PV characteristics of DSSC. The screen printing method and doctor blade technique can be employed to coat the oxide film on the FTO glass of WE. The nature of deposited oxide film critically depends on the technique of film coating as well as on the physical properties of the respective slurry paste (e.g., viscosity, binder type, solvent type, etc) which may further affects the performance of DSSC. Increasing electrode thickness also enhances the light absorption hence increases the charge generation which impact on the cell performance. Few of the works done in this area are listed below.

2.7.1 Improvements in nano structures of photoanode

A simple solution deposition method without the need of seed or fresh deposition solution was used to synthesize ZnO micro-flowers for the application DSSC fabrication with ZnO PE. The ZnO micro-flowers/nanoparticles bilayer film-based DSSC reports much higher light harvesting light harvesting efficiency, lower resistance and longer electron lifetime as compared with the ZnO nanoparticles film-based DSSC. Moreover 47 % of improvement in η is observed for monodispersed aggregates ZnO layer alone due to the scattering effect of ZnO micro-flowers layer [103].

Dye-sensitized solar cells were synthesized and applied to Echinoid-like particles (DSSCs) to enhance the Dye-loading by increasing their surface. In addition, diffuse reflectance showed that the micron size of echinoid-like particles caused a scattering effect. The increase in J_{SC} resulting from the increase in dye loading compensated for the reduction in V_{OC} and resulting improvement in η from 6.63 % to 6.74 % [104]. Work in DSSC's Titania photoanode has successfully assimilated carbon nanotubes (CNT) with a hierarchical porous structure synthesized by process called controlled phase separation [105]. The results showed lower series resistance, efficient charge injection, and improved electron life time. For effective DSSCs, the charge transport and separation properties are desirable. Moreover, the addition of CNTs to the Titania matrix increased the critical thickness with which the cell could achieve maximum performance.

DSSCs were fabricated using photoanodes made from graphene TiO_2 nanocomposites to investigate the dependency of the size of graphene sheets on the cell performance. It is reported that smaller graphene sheets improved the dye adsorption, leading to higher. The DSSC incorporated with graphene sheets of 184 nm exhibited the largest enhancement in efficiency (increased by 49 %) as compared to the cell without grapheme [106].

A TiO_2 film of double layered nano structure employed for the development of photo anodes for DSSCs [107]. The performance of the DSSCs fabricated of composite photoanodes of TiO_2 nanoparticles (NPs)/NPs (TiO_2 P-P), TiO_2 NPs/nano-belts (NBs) (TiO_2 P-B), TiO_2 NBs)/NBs (TiO_2 B-B) is also investigated. It is observed that TiO_2 NB layer improves the light scattering and the TiO_2 NP layer improves the dye absorbing capacity of the film which further improves the overall η of DSSC

to 4.81 %, 3.55 % and 0.36 % for TiO$_2$ P-P, TiO$_2$ P-B and TiO$_2$ B-B respectively.
Various research works discussed the growth mechanism of zinc oxide (ZnO) samples
of different morphologies. It reports electrochemical deposition (ECD) technique to
grow ZnO samples by controlling the concentration of precursors. The influence of
the morphology of ZnO samples on the performance of the assembled DSSCs based
on ZnO working electrode (WE) by investigating their PV characteristics, quantum
efficiency (QE) and electrochemical impedance spectrum (EIS).

By using ECD technique along with controlling the concentration of precursors, ZnO
sample of different morphologies eg. film, nanowire and nanosheet are studied and
employed for the DSSCs applications. It is reported that the DSSC fabricated with
ZnO nanowire array as WE shows improvement in dye absorption and also enhanced
the rate of photon utilization which further provides the rapid collection channels
for the photo-excited carriers. Therefore, the PV improves the PV performance and
η of the DSSC based on ZnO nanowire (WE) [108].

Table 2.7: Summary of performance parameters on improvements in
nanostructures of photoanode.

S.No	Proposed idea	J_{SC} mAcm^{-2}	V_{OC} (V)	FF	η	Ref.
1	Application of ZnO micro-flowers as scattering layer for ZnO based DSSCs with enhanced conversion efficiency					[103]
Type	ZnO nanoparticles film based cell	8.03	0.49	0.56	2.31	
	ZnO bilayer film-based cell	10.30	0.53	0.55	3.20	
2	Echinoid like particles with high surface area for DSSCs					[104]
Type	Single layer film using echinoid particles	10.2	0.747	0.67	5.15	
	Single layer film using beads particles	3.58	0.797	0.70	2.02	
	Double layer film using echinoid particles	13.6	0.741	0.67	6.74	
	Double layer film using beads particles	13.1	0.749	0.67	6.63	
3	Hierarchical porous titania/CNT composite photoanode synthesized by controlled phase separation for DSSC					[105]
CNT wt%	0.16	3.60	0.681	0.53	1.29	
	0.32	10.12	0.680	0.56	3.85	
	0.64	5.82	0.685	0.52	2.18	

	1.28	4.44	0.680	0.55	1.66	
4 Graphene thick-ness	Performance enhancement of DSSCs by incorporating graphene sheets of various sizes					[106]
	1.2 μm	11.87	0.68	0.63	5.09	
	444 μm	12.92	0.68	0.66	5.31	
	292 μm	13.75	0.68	0.60	6.15	
	184 μm	14.66	0.68	0.66	6.62	
5 Type	DSSCs based on TiO$_2$ nano particles/nano belts double layered film with improved PV performance					[107]
	TiO$_2$ P–B	14.1	0.557	0.61	4.81	
	TiO$_2$ P-P	11.2	0.505	0.62	3.55	
	TiO$_2$ B-B	0.97	0.637	0.58	0.36	
6 Type	ZnO photo anodes with different morphologies grown by electro-chemical deposition					[108]
	ZnO film	0.1855	0.449	0.18	0.018	
	ZnO nano sheet	0.2501	0.553	0.22	0.025	
	ZnO nano wire	1.5743	0.668	0.30	0.320	
7 Type	Hydrothermal synthesis of oriented ZnO nanorod nanosheets hierarchical architecture on zinc foil as flexible photoanodes for DSSCs					[109]
	Nano-rods	1.321	0.538	0.49	0.35	
	NR-NS	3.041	0.524	0.42	0.67	
8 Type	Improving photo electric conversion efficiency of DSSC using ZnO/ZnP composite nano- rods					[111]
	Composite ZnO/ZnP on FTO	15.4	0.51	0.20	1.58	
	Composite ZnO/ZnPon ZnO film	15.9	0.55	0.20	1.76	
	ZnO nanorods on FTO	5.51	0.65	0.38	1.37	
9 Type	Controllable synthesis of rutile TiO$_2$ nano-rodarray,nano-flowers and microspheres directly on fluorine doped tin oxide for DSSCs					[110]
	Nano-rodarray	4.64	0.81	0.51	1.90	
	Nano-flower	4.04	0.75	0.50	1.53	
	Microsphere	5.12	0.78	0.48	1.94	

The hierarchical architecture of ZnO nanorods-nanosheets (NR-NS) consisted of long nanorod backbones, and thin nanosheet branches were synthesized by using a two-step hydrothermal growth process for the application of DSSCs on the zinc foil substrate. The photovoltaic results showed that the ZnO NR-NS hierarchical architecture-based DSSC short-circuit current density increased significantly com-

pared to that of DSSC based nanorods, which was due to higher dye loading and superior light scattering within the photoanode of the NR-NS hierarchical architecture. As a result, the η of the hierarchical architecture based DSSC based on ZnO NR-NS increased by 90 % compared to that of the DSSC based on nanorods [109]. Using a simple hydrothermal process, TiO_2 films with various morphologies directly grown on fluorine-doped tin oxide (FTO) substrates were prepared. Assembled DSSC with TiO_2 microsphere films grown as a photoanode on the FTO substrate achieves an overall photoelectric conversion efficiency of 1.94 % and I_{SC} of 5.12 $mAcm^{-2}$ due to the rough surface, which is higher than that of the nanorod array and DSSCs based on nano flower [110] (see summary in Table 2.7).

2.7.2 Seed layer and preparation methods

Application of mesoporous TiO_2 for DSSC is widely preferred in order to implant high density of dye molecules onto the surface of TiO_2 nano particles for enhancing the photon absorption. DSSC sometimes also suffers from problem of short circuit between TCO and liquid electrolyte due to highly mesoporous property of TiO_2. This undesirable phenomenon can be regulated by employing a compact layer of sol-gel processes TiO_2 nano particles of size 5-10 nm. Later sol-gel processes were replaced by RF sputtered TiO_2 films.

A vital component for improving the η of DSSCs based on of ZnO nanorods array is the dye adsorption which can be investigated by the dye adsorptivity factor of single nanorod and the density of nanorod arrays.

With increasing seed layer thickness, the density of the nanorod arrays gradually increases, further forming large surface area for dye adsorption efficiently. Furthermore, the increased dye loaded molecules on the surface is the result of continuous increasing the number of desorption/adsorption cycles. As a result, it is noted that the photocurrent densities (J_L) and η of ZnO nanorod array-based DSSCs have significantly improved [112].

By combining the commercial titanium powder P-25 with a titanium sol gel, the TiO_2 photoanode was prepared. Two monolayer photoanodes with ultrasonic and without ultrasonic TiO_2 pastes of approximately the same thickness were prepared and their results were compared with the overall performance of the DSSC cells. The

ultrasonic TiO$_2$ photoanode was efficient for DSSCs where the improvement of the overall energy conversion efficiency is achieved for the sonicated TiO$_2$ photoanode with the presence of PEG was almost double that of the non-sonic film [113].Few of the key improvement reported in the seed layer deposition are listed in Table 2.8.

Table 2.8: PV performance of DSSC with respect to experiments conducted on seed layer (SL).

S.No	Fabrication of Photo-anode	J_{SC} mAcm^{-2}	V_{OC} (V)	FF	η (%)	Ref.
1	ZnO nano rod based DSSC					[112]
thickness of SL	10 nm	1.85	0.55	0.37	0.38	
	20 nm	1.95	0.55	0.37	0.39	
	50 nm	2.05	0.55	0.36	0.40	
	75 nm	2.10	0.55	0.36	0.42	
	100 nm	2.08	0.55	0.36	0.42	
2	Monolayers photoanodes, with and without ultra sonic treatment					[113]
Type	With ultrasonic treatment	7.25	0.71	0.516	2.67	
	Without ultrasonic treatment	3.68	0.63	0.561	1.31	
3	Optimized spin coating process for seed layer formation					[114]
Combination	Bare-FTO+DT51	5.88	0.444	0.47	1.21	
	SC2+DT51	6.90	0.515	0.63	2.23	
	SC4+DT51	6.94	0.494	0.55	1.87	
	SC6+DT51	6.08	0.496	0.58	1.76	

Using an alcoholic TiCl$_4$ solution, an optimized spin coating method was created and correlated to the final properties of the layer. To achieve a uniform layer, the physicochemical features of the precursor solution and the spin coating parameters have been optimized. The results were compared with those obtained using a traditional dip coating technique, showing that blocking layers are produced by the newly developed spin coating process, resulting nearly 84 % of improvement in η [114].

Using tetrabutyl titanate as the starting material, nanocrystalline TiO$_2$ was prepared through hydrothermal synthesis. The reaction temperature changed from 120 °C to 160 °C with a constant reaction time of 12 h, and the pH value of the reaction medium ranged from 1 to 9. The experimental results showed that the pH value influenced the phase of the powder, while the particle size depended on the temper-

ature of the reaction. Pure TiO_2 anatase was obtained at a pH of 3. The DSSC's
solar energy conversion efficiency provided with pure TiO_2 anatase prepared at 140
°C was reported to 3.64 %, which was higher than that prepared under any other
conditions with TiO_2 as listed in Table 2.9. The TiO_2 (P25) purchased was used for
comparison to make a DSSC. It turned out that the efficiency of all TiO_2 DSSCs
prepared by hydrothermal synthesis was greater than that of P25 [115].

Table 2.9: PV parameters of assembled DSSCs from TiO_2 prepared at 140°C under
different pH values [115]

S.No	Samples	Anatase content, (%)	V_{OC} (V)	J_{SC} mAcm^{-2}	FF	η (%)
1	pH = 1	81	0.71	4.62	0.66	2.17
2	pH = 3	100	0.71	8.17	0.62	3.64
3	pH = 5	89	0.68	7.20	0.62	3.02
4	pH = 7	87	0.69	7.33	0.66	3.31
5	pH = 9	85	0.72	6.44	0.64	2.98
6	P25	75	0.68	5.65	0.55	2.12

Graphene–titania films were developed by aerosol deposition with varying graphene
concentration from 0.1 to 1.0 wt % to produce G–TiO_2 films for DSSC applica-
tion as listed in Table 2.10. The optimal concentration was reported at 0.3 wt %,
which reduced the rate of recombination, favoring the formation of pairs of photo-
generated electron-holes. The conversion efficiency decreased owing to higher ab-
sorption of light by graphene present on the surface, thus reducing the generation
of electron–hole pairs for concentrations higher than 0.3 wt % [116].

Table 2.10: Parameters for DSSCs based on different graphene concentrations [116]

S.No	Sample (wt %)	V_{OC} (V)	J_{SC} mAcm^{-2}	FF	η (%)
1	Pure	0.68	7.20	64.26	3.14
2	0.1	0.75	8.92	60.95	4.08
3	0.3	0.75	10.93	61.26	5.02
4	0.5	0.74	10.90	59.12	4.77
5	0.7	0.72	9.27	60.14	4.00
6	1.0	0.69	8.67	60.47	3.62

For parallel modules, flexible dye-sensitized solar cells (FDSSCs) are introduced
with varying numbers of arrayed TiO_2 WE. Instead of a single cell, FDSSCs are

typically manufactured as a module type to improve the PV characteristic parameters and η are listed in Table 2.11. The general modules of the FDSSCs are designed as parallel strip-shaped and parallel forms of interconnection, and there are some advantages, such as simple production, low cost and simple structure. The active areas of FDSSCs are the same (0.48 cm^2) in this recorded study and have different amounts of thin TiO$_2$ films.

The single strip-shaped (TSP) WE of TiO$_2$ have a higher internal resistance than thin films of TiO$_2$. The best way to solve the problem, higher internal resistance than single TiO$_2$ thin film, is therefore to produce the different quantities of arrayed flexible TiO$_2$ WE. As a result, the FDSSC, which has the WE of the TSP TiO$_2$, has a higher η (0.25 %) than other TiO$_2$ thin films [117].

Table 2.11: Performance parameters of FDSSCs with different quantities of TiO$_2$ thin films [117]

S.No	Different quantities of TiO$_2$ thin films	V$_{OC}$ (V)	J$_{SC}$ mAcm^{-2}	FF %	η (%)
1	single strip shaped	0.78	0.56	35.06	0.15
2	double strip shaped	0.70	0.86	36.19	0.22
3	triple strip shaped	0.71	1.11	31.67	0.25

TiO$_2$ films of about 100 nm thickness were RF-sputtered at room temperature on indium-tin-oxide coated glass substrates and used as the compact layer for fabrication of DSSCs. The PV characteristics of the DSSCs with AM 1.5 illumination showed a very high V$_{OC}$ of 780 mV, a high R$_{SH}$ of 400 KΩ, J$_{SC}$ = 12.3 mA/cm^2 and FF = 61 %, while the V$_{OC}$, R$_{SH}$, J$_{SC}$ and FF of the DSSCs manufactured with traditional sol-gel processed TiO$_2$ compact layers were 520 mV, 463 KΩ, 5.4 mA/cm^2 and 46 % respectively [118].

2.7.3 Experiments with semiconductor materials

It is observed that absorption of visible light spectrum can be increases by doping narrow band gap semiconductor to TiO$_2$. When a narrow-band meso-porous TiO$_2$ electrode to enhance the light harvesting η of DSSCs. Few of the metal chalcogenide semiconductors such as cadmium sulfide (CdS), cadmium selenide (CdSe), lead sulfide (PbS), and CdS/CdSe are used to fabricate quantum dot-sensitized solar cells

(QDSSC).

The various working electrodes based on quasi-core–shell TiO_2/PbS composites are fabricated by a simple hydrolysis process. Results investigated that apportion spectra is shifted from UV to visible range. Various experimental works (samples F1-F11) were carried out consisting different proportions of the elements (by weight) and performance of the various associated DSSCs is listed in Table 2.12 [119].

Table 2.12: PV parameters of DSSCs from different experiments. [119]

S.No	Experimental substrate	V_{OC} (V)	J_{SC} mAcm^{-2}	FF	η (%)
1	F1	0.65	13.86	0.57	5.11
2	F2	0.64	13.72	0.54	4.85
3	F3	0.71	11.07	0.54	4.26
4	F4	0.69	10.19	0.57	4.03
5	F5	0.71	6.19	0.67	3.56
6	F6	0.67	6.87	0.71	2.96
7	F7	0.62	16.55	0.56	5.75
8	F8	0.61	15.42	0.60	5.70
9	F9	0.71	16.37	0.52	6.05
10	F10	0.77	9.48	0.60	4.35
11	F11	0.71	8.89	0.60	3.82

A new idea for improving the efficiency of TiO_2 DSSC by proposing of a double-layer film doped with various Zinc (Zn) ions, with a variety of morphologies and phase arrangements. The light absorption and scattering is improved by low energy bandgap. The PV parameters of DSSC assembled for TiO_2 mono layer (compositions of Anatase and Rutile) and TiO_2 double layer (as light scattering layers) with various Zn atomic % along with dye loading are listed in Table 2.13 and Table 2.14 respectively [120].

The thickness dependent performance of TiO_2 passivated DSSC grown by sputter technique on F-doped SnO_2 (FTO) electrode as listed in Table 2.15. The idea of implementing this technique is to investigate the optical transparency, surface roughness and passivation properties of the TiO_2 layer passivating the FTO electrode which are the function of thickness of the TiO_2 passivating layer. More over it is reported that the η of the cell is critically dependent on the thickness of RF sputtered TiO_2 layer inserted between FTO electrode and nanoporous TiO_2 layer. Hence 50nm thick TiO_2 passivating FTO electrode showed the maximum power η

of 4.42 % due to effective prevention electron back reaction (electron/electrolyte recombination) as shown in table below [121].

Table 2.13: PV parameters for fabricated mono layer DSSC [120]

S.No	Experimental substrate	V_{OC} (V)	J_{SC} mAcm^{-2}	FF	η	Zn at%	Adsorbed dye (10^{-8}cm^{-2})
1	ZT0	0.70	11.98	0.61	5.18	0.00	8.82
2	ZT2	0.69	12.74	0.60	5.32	0.257±0.01	9.05
3	ZT5	0.66	14.29	0.60	5.73	0.507±0.01	9.41
4	ZT7	0.65	13.95	0.59	5.45	0.757±0.01	9.32
5	ZT10	0.64	12.88	0.59	4.95	0.107±0.01	9.16

Table 2.14: PV parameters for fabricated double layer DSSC [120]

S.No	Experimental substrate	V_{OC} (V)	J_{SC} mAcm^{-2}	FF	η	Zn at%	Adsorbed dye (10^{-8}cm^{-2})
1	ZT5/N0	0.68	14.77	0.60	6.14	0.50±0.01	7.95
2	ZT5/N5	0.67	13.48	0.60	5.50	0.50±0.01	7.42
3	ZT5/NM0	0.68	16.02	0.60	6.58	0.50±0.01	8.39
4	ZT5/NM5	0.66	14.61	0.59	5.85	0.50±0.01	7.9

Table 2.15: DSSC PV performance fabricated on TiO$_2$/FTO/glass substrate with different thickness of TiO$_2$ passivating layer [121]

	PCE (%)	J_{SC} mAcm^{-2}	V_{OC} (V)	FF (%)
FTO/glass	3.8	7.78	0.79	61.0
TiO$_2$-10 nm	4.18	8.82	0.79	64.5
TiO$_2$-20 nm	4.20	9.00	0.78	59.0
TiO$_2$-50 nm	4.42	10.38	0.78	54.2
TiO$_2$-100 nm	4.13	9.38	0.79	55.3

2.8   Improvements in counter electrode (CE)

Various researches to develop Platinum (Pt) free counter electrode (CE) are carried out in order to minimize the fabrication cost of DSSC. In this research area CEs were produced using graphene nanoplatelets (GNPs) or multi-wall carbon nanotubes (MWCNTs) or various weight % of hybrid GNPs and MWCNTs mixtures. These materials have been dispersed using PEDOT: PSS polymer and then deposited on

FTO glass as well as on a non-conducting glass substrate by a drop casting method. Results show the improvement in η and life of CE (see Table 2.16).

Researchers also examine DSSCs incorporated with carbon nano-onions as CE. The candle flame deposition technique is carried out to deposit synthesized carbon nano-onion nanoparticles on Cu sputter coated glass substrates (see Table 2.16). DSSCs performances indicated that the carbon nano-onion based CE exhibit comparable performances to conventionally used Pt and could be scaled up in industrial production [122].

Table 2.16: PV performance of DDSC by modification in CE.

S.No	CE Proposed idea	J_{SC} mAcm^{-2}	V_{OC} (V)	FF	η (%)	Ref.
1	Counter electrodes using nano particles					
Type	C hybrid/glass type CE	8.275	0.64	0.47	2.48	
	PEDOT:PSS/glass type CE	0.686	0.4	0.4	0.11	
	GNPs/glass type CE	2.46	0.6	0.34	0.51	
2	Carbon nano onion CE	7.65	0.68	0.65	3.39	
						[122]
3	Fabrication of transparent CE					
						[123]
Type	Pt nano particle based CE	11.24	0.82	0.67	6.17	
	Sputtered Pt based CE	10.84	0.815	0.72	6.36	

It is reported that a highly transparent Pt CE can be achieved by spray coating of Pt nano-particles (NPs) on pre heated substrates and 86 % reduction in the consumption of Pt is observed during the experimental work which further reduces the cost of fabrication of DSSC [123].

A composite photo electrode with Pt nanoparticles (NPs) is deposited on three dimension FTO glass. This 3D FTO conductive grid was fabricated as the CE of DSSC, which exhibits larger electrochemical active surface area (9.54 m^2/g) and lower charge transfer resistance (2.1 Ω) in iodide/triiodide (I$^-$/I$_3$$^-$) redox electrolyte than the conventional planar CE which further results 14 % higher η [124].

A nano-structure-based Pt counter electrode was manufactured to increase the performance of the DSSC by assembling silver (Ag) NPs on glass substrates and depositing a thin Pt layer. DSSCs with nano-particulate structure have improved the overall PV characteristics [125].

2.9 Effect of annealing on PV response

The improvement in the photoelectrochemical properties of the manufactured cell sintered at elevated temperatures can be due to (1) an increase in crystallinity which is beneficial in the geometry of anchoring dyes leading to faster electron injection [126], (2) an increase in the size of the grain leading to an improvement in the scattering of light and a decrease in the interconnection between particles [127]. In addition, the increase in annealing temperature increases the injection of electrons by enlarging the coefficient and lifetime of electron diffusion. At more than 500 °C, the overall photovoltaic characteristics were drastically reduced (see Table 2.17). This may have been caused by the reduction of the substrate's conductivity due to conductive film degradation [128].

Table 2.17: Impact of annealing temperature variation on DSSC PV performance [128]

Annealing temperature (^{o}C)	V_{OC} (mV)	J_{SC} mAcm^{-2}	FF	η (%)
350	522	0.43	0.36	0.081
400	496	0.52	0.32	0.084
450	564	0.66	0.29	0.11
500	525	0.59	0.24	0.082
550	522	0.58	0.24	0.079

2.10 Encapsulation of DSSCs

UV radiation and environmental deterrents can degrade semiconductor photoelectrodes, photosensitive dyes (synthetic pigments and complexes), and other nanomaterials used in photocatalytic water splitting.The equipment's encapsulation requires the appropriate non-corrosive (with electrical exposure), non-conducting, extremely transparent barrier material Therefore, the barrier material should possess some of the crucial properties which help the effective functioning of these devices to be used in the previously discussed specific applications [129]- [130].

- Flexibility: The encapsulant material, as well as the device substrate, must be flexible enough to prevent cracks formtion.

- Hermetic: The device must be totally sealed from the outside environment, safeguarding it from external degradants such as O_2, H_2O, chlorofluorocarbons, and UV rays.

- Extremely low gas permeability: The encapsulant should act as a barrier against penetrating gases such as oxygen and moisture.

- Stability: The encapsulant must be stable in terms of dimensions, chemical properties (non-corrosive), thermal properties, and electrical properties.

- Processing ease: Processing compatibility with the final product for integration is a critical criterion in terms of energy and economic savings.

As a result, several organic and inorganic materials are being studied for their usage as encapsulants in order to meet these specific requirements.

A new family of $Fe_{1-x}S/Fe_3C$-NCNTs hybrids, with the architecture of "$Fe_{1-x}S$ loading on Fe3C-encapsulated and N-enriched carbon nanotubes", was strategically established by a facile in-situ carbonization-sulfurization process and developed as CE catalysts in DSSCs. The electrochemical results showed that the hybrids delivered an excellent catalytic activity for I_3^- reduction with a low charge transfer resistance of 1.56 Ω, and the $Fe_{1-x}S/Fe_3C$-NCNTs CE based DSSC achieved a high power conversion efficiency of 8.67%, which is superior to 7.75% of the device based on traditional Pt CE. Furthermore, the DSSC with $Fe_{1-x}S/Fe_3C$-NCNTs hybrid CE also showed an extraordinary electrochemical stability in long-term operation.

The impact of cellulose nanocrystals (CNCs) made from bacterial cellulose (BC) and nanofibrillated cellulose (NFC) on the structural properties of polyurethane (PU) composites are also investigated [131] . The feasibility of using the polymer composite to encapsulate dye sensitised solar cells piqued the researchers' curiosity. Both CNCs were esterified before being mixed with the polyurethane in a solution method. In this study, the strongest PU nanocomposite. film was obtained when 2 wt % of the esterified BCNCs was applied to the polymer matrix. The results from thermal analysis indicate that the onset temperature for decarboxylation step of the polymer increased after adding the modified CNCs. The water vapor transmission rate of the PU films was rapidly dropped by 56% when 0.5 wt % of the esterified BCNCs was added. Percentage visible light transmission through the polymer com-

posite films was above 80%, regardless of the type and concentration of the CNCs. By encapsulating dye sensitized solar cells with the polymer/esterified B-CNC composites, it was found that the lifetime of the devices can be extended by more than 336 h without losing its initial power conversion efficiency.

Hence from the literature survey it is understood that the optimum electrolyte concentration and type of electrolytes are two vital electrolyte parameters in order to control and optimize the performance of the DSSC. Improving the Dye regeneration capability of electrolytes and recombination kinetics enhances the dye regeneration efficiency of the solar cell. Electrode thickness can be considered as critical component which determines the light harvesting capability of DSSC device. EIS curve fitting technique can be one of the efficient methodology to investigate the charge transport properties for the evaluation of electron recombination kinetics and their life time across TiO_2/electrolyte interface.

Controlling the electrode (WE) thickness, slurry or paste preparation and composition, particles shape, size, porosity and its distribution in the oxide film can be treated as major factors which have significant potential in order achieve optimum performance of DSSC. The discussed modifications can be considered in order to modulate the physical and chemical properties of WE to enhance PV performance of DSSC.

The variations of morphology, size and crystal phase of TiO_2 micro/nanostructures have potential to enhance the performance of the DSSC by improving dye loading, superior light scattering ability, and/or faster electron transport and longer electron lifetime. Hence by finding the high yielding routes for synthesis of various morphologies for TiO_2 nanoparticles with suitable band gap can be considered as another approachable method to improve the cell performance and same is discussed in chapter 3.

Chapter 3

Facile one pot hydrothermal synthesis of nanorice-like TiO$_2$ for an efficient dye sensitized solar cell (DSSC)

3.1 Introduction

Apart from traditional applications, nanocrystalline TiO$_2$ intrinsically possesses multi-functional properties such as environmental photocatalysts (polluted airs, wastewaters, self-cleaning windows having antimicrobial activity); efficient electrodes for photovoltaic, photo-electrochromics and gas sensing devices etc. In this matter, several physical techniques and chemical approaches have been successfully used to prepare various crystal forms and anisotropic shape nanosize crystalline TiO$_2$ materials [132]- [134]. Among these chemical approaches, a low temperature hydrothermal (HT) reaction is widely preferred because of its simplicity, low-cost, and ability to readily control the physicochemical properties of material need to be synthesized e.g. crystallinity, size and morphology of particles, and textural Brunauer-Emmett-Teller (BET) features (surface area; pore's shape/size and volume). Such controlled desired physicochemical properties of material can be achieve by making a tailored combination among the reaction variables viz. time, temperature, type of precursors (pristine or chemical modification), type of solvent and pH

controlling agent etc.

Here, in this chapter, we report a simple and facile low temperature HT synthesis of high crystalline nanorice-like TiO_2 powder, whose pore's size and volume are though relatively larger than to a commonly exploited model (Degussa, P-25) powder, yet both these TiO_2 powders have more or less comparable average particles' size and BET surface-area. As the nanoparticles of these TiO_2 powders differs in their shape (P-25 is nearly spherical) so such shape dependent superior charge transfer properties of nano-rice like TiO_2 is highly reflected in an easily implemented a low cost DSSC device technology, which could fulfil our future needs of clean energy [135]. Under global light illumination (1 sun, AM 1.5 G), and identical electrode fabrication and DSSC assembling conditions, cell made of nanorice-like anatase TiO_2 easily gave a solar to electric conversion efficiency (η) ca. 6.49 %, an enhancement of ca. 19 % with respect to that of a reference cell made of a commercially available and commonly exploited benchmark TiO_2 (Degussa, P-25).

3.2   Adsorption of a gas on the material's surface by BET Analysis

The basic element of the theory of BET is the adsorption of a gas (adsorbate) on the surface of the material. The physical adsorption due to the Vander Wall forces existing between the gas molecules and adsorbing surface and chemical adsorption due to formation of resultant products by chemical reaction solid surface and gas molecules are the two major type of adsorption phenomenon [136]- [138]. All the adsorbed molecules forming the layer are in contact with the surface of the adsorbent [139]- [142], [144]- [145]. In addition to this it is possible to compare the net amount of gas adsorbed with its surface area of the adsorbent material [143]. In a closed-packed structure, this coverage can happen when molecules are close to each other or when scattering across the surface as well. Solid and gas interacting force keeps the gas molecules on the surface of the adsorbent material.

On the other side, more than one layer of gas molecules is generated with multilayer adsorption, so it can be easily stated that all the gas molecules are not available to make the contact with the top surface adsorbent layer. Therefore, gas molecules

start interacting to each other in their vapor phase. These interaction energies of the vapor phase are close enough to match the energies in solid-gas interaction that contributes to the gas adsorption at the top of gas molecules that are already adsorbed on a solid's surface. As a consequence, a gas condenses into a liquid phase [146]. When the temperature of the absorbent surface is lower than the critical temperature of gas molecules, multilayer adsorption is a common phenomenon.

The pressure increases until it reaches to a value close to the bulk vapor pressure during the formation of adsorbate molecules [146]. After monolayer (ML) and subsequently ML adsorption on the pore walls, capillary condensation signify that pores are filled with condensed gas. The increased Vander Waals interactions between gas molecules at confined space of pores leads to vapor-liquid phase transitions below the bulk liquid's saturation vapor pressure (P_{sat}) [137]- [147]. From BET analysis its can be assumed that each adsorbed layer is not interfering to it next layer during the ML adsorption. Hence Langmuir equation can be applied on each adsorbed layer [148]- [149]. Molecules act as absorption sites in the layers below the initial one The BET equation is established as given by eqn. 3.1 [147].

$$\frac{P/P_0}{n(1 - P/P_0)} = \frac{1}{n_m C} + \frac{C - 1}{n_m C} \left(\frac{P}{P_0} \right) \tag{3.1}$$

3.2.1 N_2 gas Adsorption Technique

Adsorption can be defined as the "tendency of one component of the system to have a higher concentration at the interface than it has in either of the adjacent bulk phases". Considering a solid-fluid type system where the fluid density continuously increases near the region of solid fluid interface. Adsorption phenomenon is further categorized into physisorption and chemisorptions illustrating whether the gas molecules and the surface layer are interacting through chemically interactive forces or physically interactive forces in nature. Experiments to analyze the physisorption process are carried out with various gases and under various sets of pressure-temperature conditions. Conditions like low temperature and higher pressure are also preferred for efficient adsorption and these experiments are capable to investigate the surface area and pore's structure of the porous sample material (textural properties).

Now day's nitrogen gas (N_2) at 77 K is normally used for characterize the textural properties and to analyze mesoporous nature of the sample (TiO_2 etc). Gases like carbon dioxide at 273 K, argon at 87 K, and krypton gas at 77 K may also be used for the characterization to study the adsorption process. Moreover analysis of adsorption taking place at higher pressures, where the gas is in the supercritical stage, provides the information on the nature of the surface of the sample and its gas adsorption potential, as well as information on the surface area and surface properties of the sample (TiO_2 etc.).

3.2.2 Experimental Procedure and fundamentals principles of BET

In this procedure, a discontinuous static volumetric method is used to investigate the amount of gas adsorbed on the sample by conducting experiments on Micromeritics ASAP 2010™ instrument after the preparation of sample. Prior to the analysis, degassing of the sample (1-2 gm) inside the tube is done by creating vacuum (<10 μm Hg) and then heating it at 200 ^{o}C for 24 Hrs. Further heat treatment under vacuum conditions is done until the sample out–gassing rate reach below to 0.005 Torr/min over a 15 minute interval ($\sim$16–24 hours). The dead volume of the tube is measured volumetrically by using helium before performing experiment for adsorption isotherm. The helium evacuation is performed from the sample tube and the tube is then kept in cryogenic liquid nitrogen (LN_2). Afterwards, the sample tube is dosed with N_2 (of known amount) with precisely controlled pressures. The amount of adsorbed gas on the solid surface at constant temperature is measured at discrete pressure (P) steps over the relative equilibrium pressure P/P_0 range of 0.0075 to 0.995.

After increasing the pressure up to condensation pressure (branch of adsorption), the pressure reduces from the pressure point P_0 (branch of desorption). During this operation data sets are collected and reported as the profile of isotherm related to adsorption process. This results in the characteristics where quantity of gas adsorbed per mass (moles or volume (cm^3/g) is plotted as a function of P/P_0.

3.2.3 Qualitative Interpretation of N_2 Isotherm Profile

Combined analysis of isotherm's shape and its hysteresis pattern is considered as vital characteristics for the interpretation the nature of physisorption mechanism and solid-gas interaction which are capable for the qualitative prediction of the variety and type of pores present in the adsorbent. Along with four types of hysteresis patterns (H1-H4), IUPAC further estimates six types of adsorption isotherms (Type I-VI) [19] where three are discussed in detail in this chapter which are particularly critical reason behind the formation of isotherms for unconventional gases and oils as shown in (Figure 3.1) [150]- [151]. Different mesopore shapes are characteristic of the various hysteresis patterns H1-H4.

3.2.3.1 Isotherm: Type I

A microporous (MP) adsorbent shows a concave-shaped isotherm for the ranges $P/P_0 < 0.01$ until it reaches a plateau. For this range of relative pressure relative pressure isotherm shows very high adsorption (see Figure 3.1(a)). The small micropores result in overlapping the possible adsorption fields of opposite walls. This overlapping potential energy creates an increased interaction of absorbent-adsorbate resulting in high uptake of adsorption at low relative pressures. This phenomenon is called as the filling of micropores. The limited uptake (plateau) depends on the sample's cumulative accessible volume of micropores.

3.2.3.2 Isotherm: Type I

A fully reversible isotherm (Figure 3.1(b)) can be exhibited by a non-porous or macroporous (MaP) substance where adsorption and desorption follow exactly the same direction. At lower ranges of relative pressures ($P/P_0 < 0.2$), these isotherms initially have a concave form followed by a linear area and eventually a convex form similar to the P/P_0 axis at higher relative pressure ($P/P_0 > 0.4$). This isothermal profile reflects a mechanism of gas monolayer-multilayer adsorption on the open and stable solid surface.

3.2.3.3 Isotherm: Type IV

A characteristic hysteresis loop would have prominent mesoporous (MeP) content
(Figure 3.1(c)), which is consistent with capillary condensation and evaporation tak-
ing place in mesopores. The isotherm profile is identical to Type II isotherms at
lower ranges of relative pressure ($P/P_0<0.4$), representing a monolayer to multi-
layer adsorption process on mesopore and macropore walls. The gas condenses in
the mesopores into bulk liquid at higher relative pressures at pressures below the
saturation vapor pressure with the formation of a gas-liquid meniscus (capillary con-
densation). The profile of isotherms indicates a plateau with decreased adsorption
at high P/P_0. The restricting adsorption plateau at high P/P_0 suggests complete
filling of mesopores and subsequent adsorption on the external surfaces.

The hysteresis loop is a feature of mesopores present in the Type IV isotherms. Sev-
eral models exist to describe the phenomenon of hysteresis in adsorption isotherms
[152]. Hysteresis could be predicted from non-connecting cylindrical mesopores due
to variations in shapes of meniscus during capillary condensation (adsorption) and
evaporation (desorption) [153].

In mesoporous materials with non-connecting cylindrical pore systems such as meso-
porous silica SBA-15, such phenomena generate hysteresis profiles [152]. The pore
network and pore communication effects are other mechanisms that lead to hystere-
sis [152], [154]- [155]. The path dependence in such interconnected pore-network
systems is due to different sequences in which the molecules of the probe encounters
the pores during the process of adsorption and desorption, resulting in hysteresis.

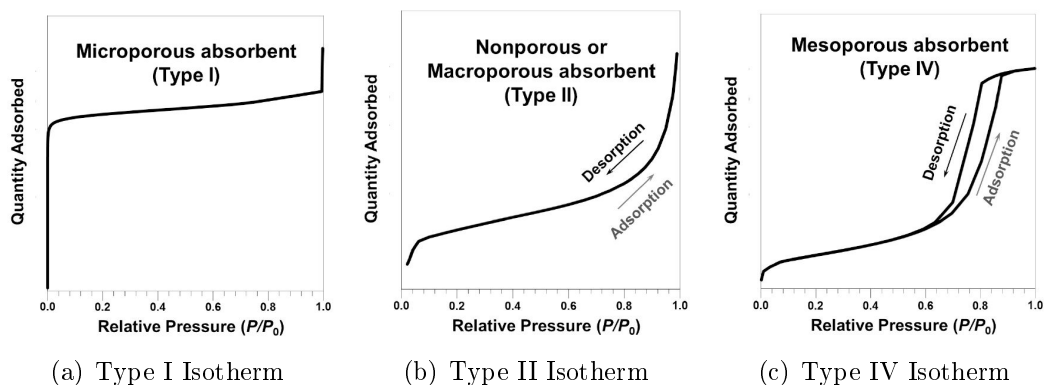(a) Type I Isotherm   (b) Type II Isotherm   (c) Type IV Isotherm

Figure 3.1: Isotherm profiles of various materials (a) purely MP (Type I) (b) MaP
(Type II) and (c) purely MeP (Type IV) [150]

The variation in mesopore shapes results different characteristic for H1 to H4 hysteresis patterns (Figure 3.2). The materials which have the property of narrow distribution of cylindrical or tubular pores are exhibiting the H1 hysteresis pattern (see Figure 3.2). The H2 (Figure 3.2) types indicate a complex, interconnected pore structure with narrow pore openings. The H3 hysteresis loop (Figure 3.2) types are mostly found in materials with platy particles having slit-shaped pores. The H4 hysteresis loop (Figure 3.2) types also result from slit-shaped pores, but are associated with micropores in general.

Figure 3.2: Hysteresis shapes of adsorption isotherm usually formed in subcritical N_2 adsorption [150].

3.3 X-ray Diffraction (XRD)

An effective non-destructive technique for characterizing crystalline materials is X-ray diffraction (XRD). It includes information of structures, phases, orientations of crystals (texture), and other structural parameters, such as average of grain size of, crystallinity, strain, and crystal defects. XRD is based on constructive monochromatic X-ray interference and a crystalline sample. XRD peaks are produced by constructive interference in a sample by a monochromatic beam of X-rays dispersed from each set of lattice planes at specific angles. Consequently, in a given material, the XRD pattern is the fingerprint of periodic arrangement of atoms.

In 1912, it is also discovered that crystalline substances behave close to the spacing of planes in a crystal lattice as three-dimensional diffraction gratings for X-ray wavelengths [156]. A cathode ray tube, filtered to emit monochromatic radiation,

collimated to concentrate, and directed towards the sample, produces these X-rays. When conditions satisfy the Bragg's law, the interaction of the incident rays with the sample produces constructive interference (and a diffracted ray) as shown in Figure 3.3 and given by eqn. 3.2.
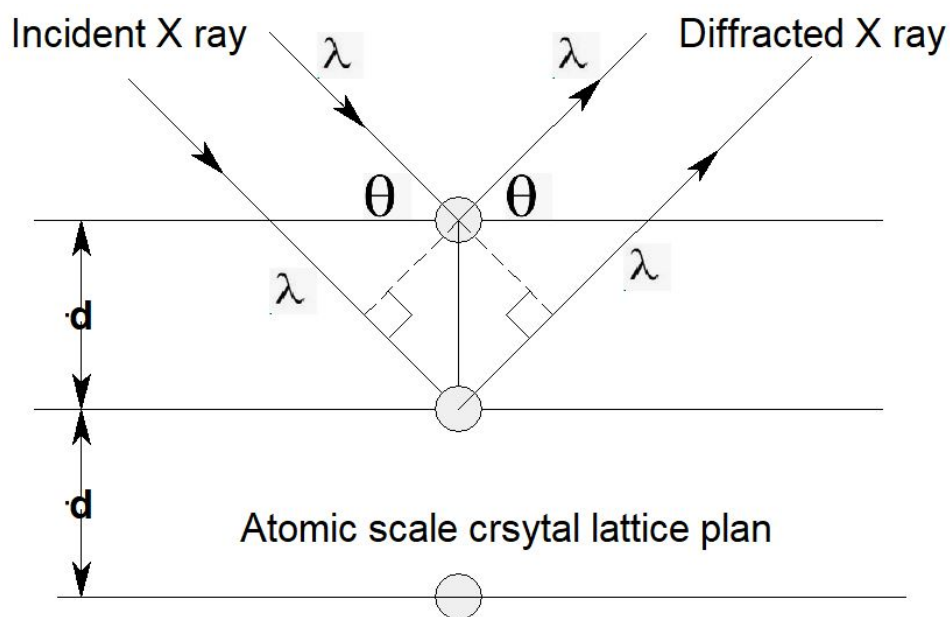
$$n\lambda = 2dSin\theta \qquad (3.2)$$

Figure 3.3: Bragg's Diffraction patters of Incident Rays for estimating interatomic distance (d)

Where "n" is representing integer numbers, "λ" is X-ray wavelength of, "d" is the diffraction producing interplanary spacing, and "θ" is the angle of diffraction. In a crystalline sample, this law relates the wavelength of electromagnetic radiation to the diffraction angle and lattice spacing. It is also necessary to analyze the powdered material for all possible diffraction directions of the lattice by scanning the sample through the set of 2θ angles, all should be achieved.

Each sample or compound follows the uniqueness for the set of d-spacing. Therefore these diffracted peaks finally transformed d-spacings for the identification of the sample by contrasting the d-spacings to the reference patterns. Three fundamental elements are composed of X-ray diffracto-meters (see Figure 3.4): an X-ray tube, a

sample holder and an X-ray beam detector [157]. By heating a filament to produce electrons, accelerating the electrons towards a target by applying a voltage, and bombarding the target material with electrons, X-rays are produced in a cathode ray tube (see Figure 3.4(a) and Figure 3.4(b)).
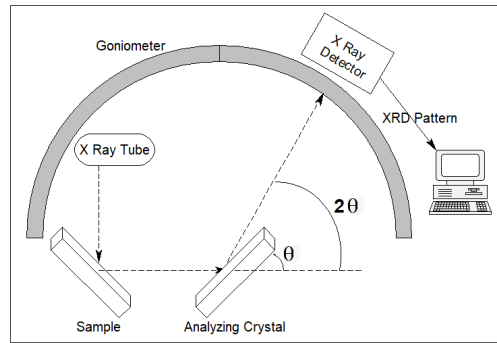
(a) Schematic diagram of a diffractometer system
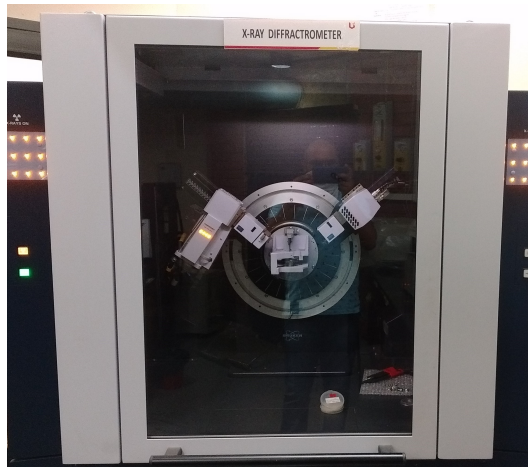
(b) XRD Instrument for analyzing crystal phases and crystallinity

Figure 3.4: XRD system

When the electrons have enough energy to dislodge the target materials inner shell electrons, a characteristic X-ray spectrum are formed. In order to generate monochromatic X-rays necessary for diffraction, filtering is needed by foils or crystal monochrometers. Copper, with CuKa radiation D 1.5418 Å, is the most common target material for single-crystal diffraction. These X-rays are collimated and the sample is targeted. The intensity of the reflected X-rays is registered as the sample and detector are rotated. As Bragg's law is met by the geometry of the incident

X-rays impacting the sample, positive interference occurs and a peak of intensity
appears. This X-ray signal is captured and analyzed by a detector and the signal is
converted to a count rate, which is then sent to a system such as a printer or com-
puter monitor. The X-ray diffractometer geometry is such that the sample placed
at goniometer which rotates at an angle θ along the direction of the collimated X-
ray beam while the X-ray detector is placed on an arm to absorb and rotate the
diffracted X-rays at an angle of 2θ . Data is obtained at 2θ from 5° to 70°, angles
preset in the X-ray scan, for standard powder patterns. For certain research stud-
ies in geology, environmental sciences, material science, engineering, and biology,
determination of unknown solids is important. For the analysis of a wide range
of materials including semiconductors , polymers, fluids, metals, plastics, minerals,
thin film coatings, catalysts, pharmaceuticals, solar cells, microelectronics, and ce-
ramics, XRD characterization technique is also globally adopted [158]. Strength and
limitations of X-ray powder diffraction (XRPD).

Strengths

1. Efficiently recognize ($<$ 20 min) the unknown sample (material)

2. Provides unambiguous mineral identification in most situations

3. Broad availability of units of XRD

4. Reasonably easy analysis of data

Limitations

1. Access to the standard inorganic compound reference file is required.

2. Material must be processed into a powder in amounts of tenth of grams

3. Detection limit for mixed materials is 2 % of the sample.

4. Indexing of patterns for nonisometric crystal systems is complex for unit cell
determinations.

3.4   Scanning electron microscope (SEM)

A scanning electron microscope (SEM) is used to investigate the external morphol-
ogy (texture), chemical composition, and crystalline structure and orientation of

materials making up the sample. Significant amounts of kinetic energy are carried by accelerated beam of incident electrons in a SEM. When these accelerated electrons interacted with electrons of the solid sample material, they starts decelerating and loses their energies which further transform into the generation of variety of signals.These type of generated signals comprise of secondary electrons (SEs), backscattered electrons (BSEs), diffracted BSEs are used to determine crystal structures and mineral orientations), photons, visible light (cathodoluminescence -CL), and heat. For imaging samples, SEs and BSEs are commonly used. The SEs is most valuable for showing morphology and topography on samples and backscattered electrons in multiphase solid samples are most valuable for illustrating contrasts in composition. The inelastic collision between electron in the sample's atomic orbital (shell) and incident beam of electrons occurs. Electron releases energy in the form of X-rays during its transition from higher energy level (HEL) to the lower energy levels (LEL). The wavelength associated with the X-rays highly depends on the energy separation between HEL and LEL. Therefore every X-ray created is the characteristics of the element present in the sample. During the SEM analysis X-rays produced through the electron interactions do not lead to sample loss, therefore SEM is also stated as "non-destructive" sample characterization technique so that sample materials can be repeatedly analyzed.

In order to allow the sample to be imaged in a SEM, it is often necessary to prepare the sample with additional processing steps before a sample can be observed in the SEM. This method often makes the sample conductive, more stable under the electron beam and in a vacuum, or optimizes the geometry between the surface of the sample, the electron, and one (or more) of the SEM-attached detectors.

Nano-sized materials, in particular, have the problem of agglomerating or aggregating, and special treatment of the samples is required for proper imaging of these samples [159]. The type of sample preparation depends on the material type. Conductive nano sized materials such as metal oxides need little preparation, are very vacuum-stable, and under the electron beam are often stable. Sample preparation often consists of attaching them to a stub by using conductive tape for these types of samples. Due to their conductive nature, they often do not need to be coated with a metal or carbon sputter to help dissipate the accumulation of charge on the

sample surface. In order to enable good images and proper particle size analysis of nano-sized materials, sample preparation is therefore critical. In order to obtain accurate dimensions of nano-sized materials, understanding of the sample is crucial.

3.5 Materials and Methods

Ti-isopropoxide (TTIP, 97 %), ethanol (EtOH, 99.9 %) and ammonia solution (NH$_3$, 28-32 wt % in water) were obtained from commercial sources and used as received. A premixture was made by simply diluting pristine TTIP with EtOH (1:6 molar ratio) inside a Teflon vessel ($\sim$100 mL), and after 10 minute of mild magnetic stirring ca. 70 ml of aqueous solvent (pH$\sim$12; adjusted by NH$_3$ of tripled deionized water; Millipore, 18 MΩ_{-1}) was carefully poured to this premixture. Within few seconds, white slurry was formed, which was kept at stirring for ca. 10 min. Then reaction was carried out at 150 °C for 12 hr as shown in Figure 3.5.
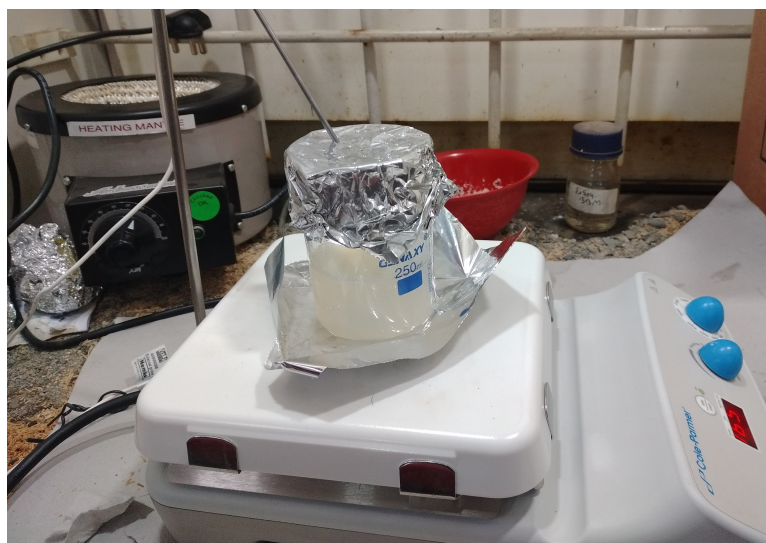

Figure 3.5: Magnetic stirring of white slurry

The resulted white products were collected by centrifugation (see Figure 3.6(a)) and excessive washing with deionized water (Figure 3.6(b)). The final TiO$_2$ powder was obtained by drying the white product at 100 °C for 4 hr (Figure 3.6(c)). and followed by the grinding (see Figure 3.6(d)).

(a) The sample of white slurry solution is centrifuged for 20 min. at 12000 rpm

(b) centrifugation seperated the white precipate collected at the botton of the vessel

(c) The white precipitate is collected and heated overnight at 100 ℃

(d) Final TiO_2 powder is collected after manually grinding process.

Figure 3.6: Slurry to TiO_2 powder formation

Crystalline-phase and average particle size of the processed sample (see Figure 3.6) were measured by using X-ray diffraction (XRD, PRO-MPD, Philips diffractometer) for the sample shown in Figure 3.7. BET properties were measured by N_2 adsorption-desorption at 77 K (Micromeritics ASAP-2010). Specific BET surface-area ((S_{BET})), pore-volume (V_P) and pore-size (D_P) were determine from N_2 isotherms using BET and Barrett-Joyner-Halenda (BJH) methods respectively. Morphological features were examined by field-emission Scanning electron microscopy (SEM; XL30S FEG, Philips Electron Optics B.V).

Figure 3.7: Sample preparation for XRD analysis

The TiO$_2$ and/or Platinum (Pt) counter electrodes were prepared by screen printing the mesoscopic TiO$_2$ paste made with the procedure given in reference [160] and/or by depositing the hexachloro-platinic acid-based paste onto conducting FTO glass substrates (TEC-10). TiO$_2$ and Pt-electrode were sintered at 500°C and 400°C for ca. 30 min respectively. The redox electrolyte consisted of 0.5 M 1-butyl-3-methylimidazolium iodide, 0.05 M I$_2$, 0.5 M 4-tert-butylpyridine in acetonitrile.
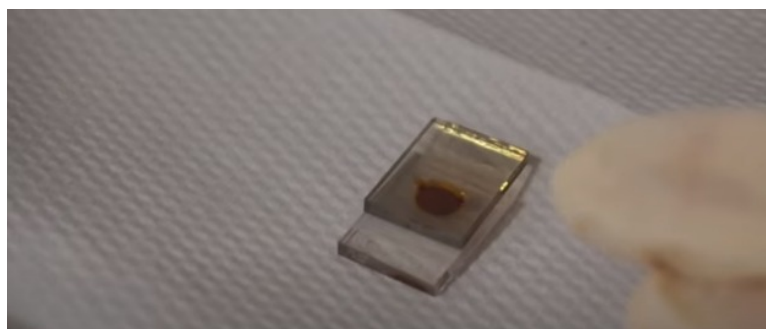

Figure 3.8: DSSC filled with electrolyte

The N719 dye adsorption capacity of electrodes were measured by immersing them overnight into 0.1 M NaOH solution (EtOH to water ratio 1:1) and calculating the concentration of N719-dye (extinction cofficient $\sim$1.41$\times$10^4 L.mol^{-1} cm^{-1}) by its light absorbance (peak at 515 nm) using UV-Vis spectroscopy (UV-2401PC, Shimadzu Corp.) The current-voltage characteristics of the assembled DSSC (see Figure 3.8 and 3.9)with Peccell solar simulator (Model: PEL-L11) were measured

under dark and 1 sun (100 mW.cm^{-2}, AM 1.5 G) illumination (see Figure 3.10). Using a Reference 600 Potentiostat (Gamry Instruments), electrochemical impedance spectra (EIS) were measured under 1 sun bias light at open-circuit conditions.
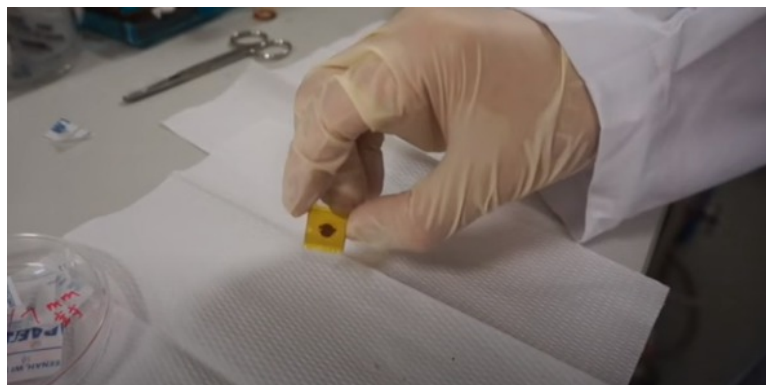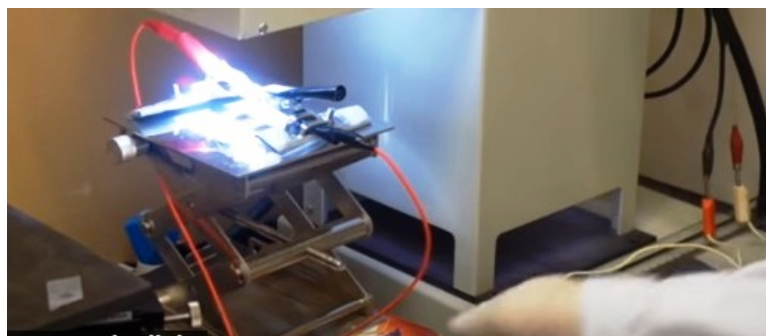

Figure 3.9: Assembled DSSC

Figure 3.10: J-V Characterization of assembled DSSC

3.6   Results and Discussion

Several crystalline TiO$_2$ powders were synthesized, however here we present one typical TiO$_2$ (obtained by a premixture of 1 mole of TTIP with 3.5 moles of EtOH), which is closely comparable to P-25 in its average particle size, BET surface area and pore's characteristics, and show much better parametric performance as an electrode film for a DSSC.
In the XRD pattern (Figure 3.11(a)), it is clearly seen that synthesized TiO$_2$ is highly crystalline with pure anatase (JCPDS Card No. 04-0477), whereas P-25 is a typical

biphasial in nature and consisted about ca. 73 % anatase ($\sim$27 % rutile) as estimated by the intense 101 peaks of its anatase and rutile phases respectively [161]. The average particles' size of prepared TiO_2 is comparable with P-25 (see Table 3.1), which was estimated by XRD(101) peak using well known Scherrer's equation [34]. Both TiO_2 and P-25 powders were found mesoporous in nature (see Figure 3.11(b)) with comparable BET surface areas (see Table 3.1). The mesoscopic nature of powders is clearly indicated by their N_2 adsorption-desorption (H3-type, IV-type; BDDT classification) hysteresis loops, and such kinds of loops and BJH pore-size distributions (see inset, 3.11(b) are typical to the nanoparticles having unordered cylindrical type pore-structures. As shown in Figure 3.11(b), N_2 capillary cohesion of as prepared TiO_2 powder occurred relatively at higher pressure indicating its larger pore features than that of a P-25 powder (see Table 3.1).

Table 3.1: Structural, textural BET features and DSSC parameters of an isotropic Degussa P-25 and rice-like anataseTiO_2

	Particle Size (nm)	S_{BET} (m^2g^{-1})	V_P (ccg^{-1})	D_P (nm)	V_{OC} (V)	J_{SC} $(mAcm^{-2})$	FF	η (%)	Dye loading (nano molcm^{-2})	f_p (Hz)
P-25	19.52	42.26	0.1211	13.05	0.788	9.45	73.2	5.45	0.569	20.58
TiO_2	18.86	43.59	0.1952	21.94	0.845	10.78	71.3	6.49	0.571	15.52

Microscopic SEM images (see Figure 3.12(a)) show the porous nanoparticles in prepared anatase TiO_2 and biphasial P-25 powders, respectively. It is clearly noticed that P-25 nanoparticles are nearly isotropic in shape, whereas TiO_2 nanoparticles are rice-like in their shape, and such anisotropic morphological growth of particle is highly expected from ongoing hydrolysis-polycondensation reactions of a molecularly modified pristine monomeric i.e. Ti-precursor $(Ti(OPr)_4)$ reacted with EtOH. When pristine $Ti(OPr)_4$ was mixed with EtOH, it is possible that some of the less electronegative OPr ligands are replaced by the more electronegative OEt ligands, hence forming a new chemical precursor $Ti(OPr)_{4-x}(OEt)_x$ [162]- [163]. Thus difference in electronegativity of two ligands should promote an efficient decoupling between hydrolysis and polycondensation reactions [162]. Inevitably, a lesser electronegative ligand is removed quickly by OH^- group during hydrolysis, whereas a higher elec-

tronegative ligand is mainly replaced by OH^- group during the polycondensation process, and consequently, a decoupling between hydrolysis and condensation reactions had played a key role in formation of anisotropic shape of nanoparticles, which is concluded from Figure 3.12(b).
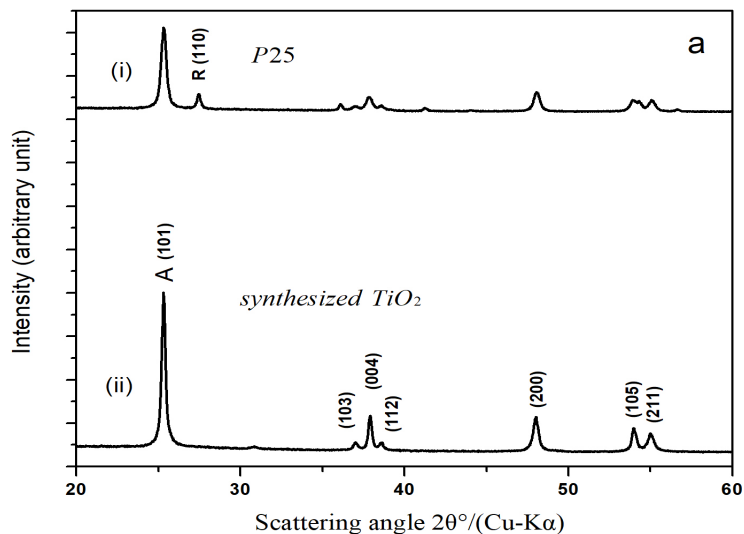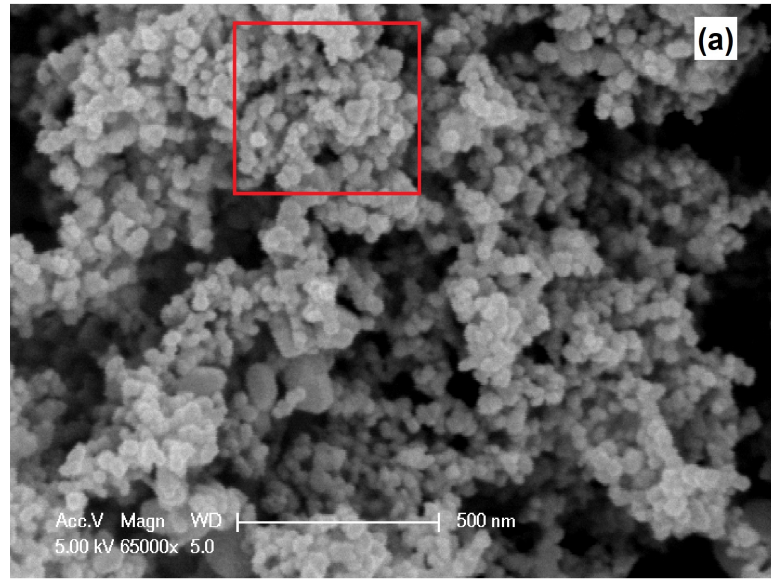

(a) XRD patterns of Degussa P-25 (i) and prepared TiO_2 (ii). R (2θ=27.460) represents the rutile-phase)
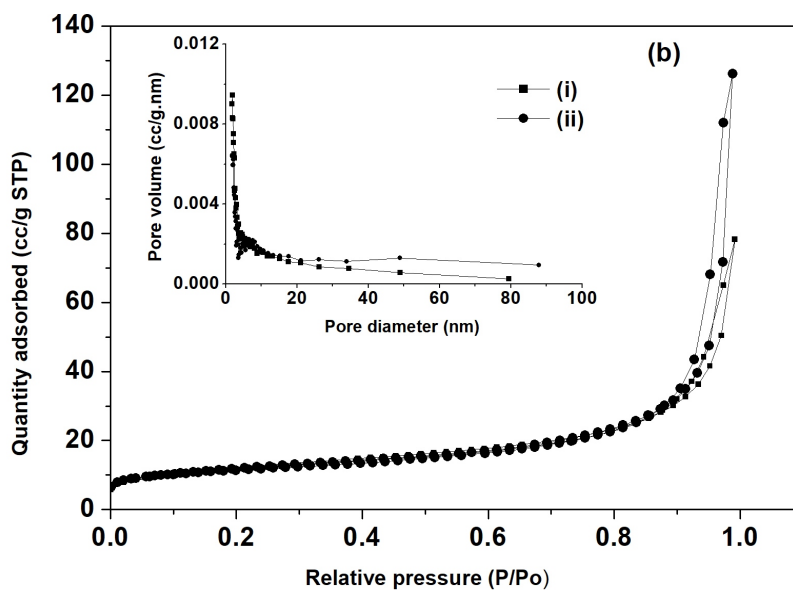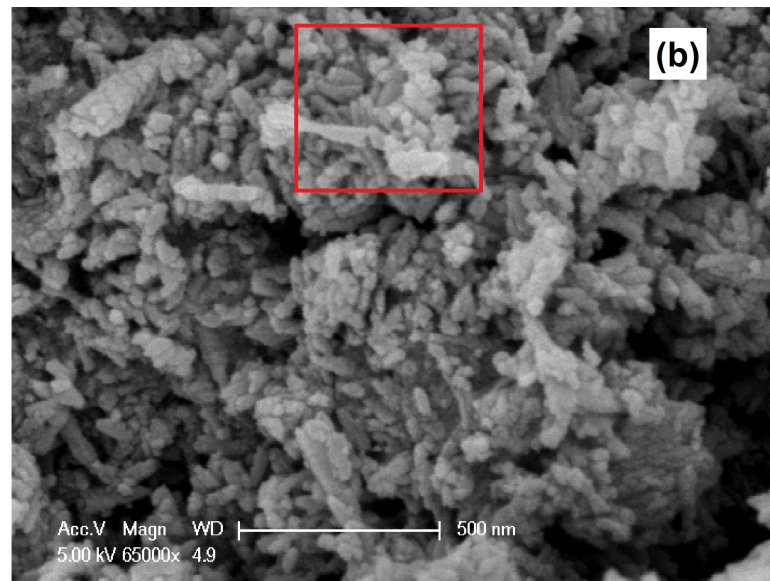

(b) N_2 adsorption-desorption BET curves (insets; pore-size distributions) of Degussa P-25 (i) and prepared TiO_2 (ii)

Figure 3.11: XRD and BET characteristics of P25 nd rice like TiO_2

(a) Degussa P-25

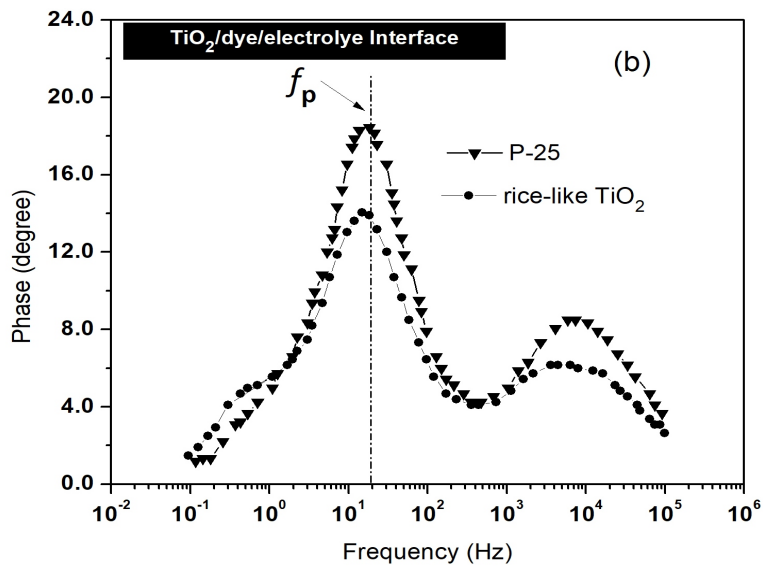(b) nanorice-like anatase TiO$_2$

Figure 3.12: Microscopic SEM image of powder samples

Though having comparable S$_{BET}$ and average particles' sizes (see Table 3.1) to that
of a routinely exploited biphasial and isotropic P-25 powder material, yet, in any
suitable potential application, nanorice-like TiO$_2$ powder material should demon-
strate better performance due to its high crystallinity, pure phase, and more impor-
tantly a distinct anisotropic shape of its nanoparticles (see Figure 3.11 and Figure
3.12). In this view, we have tested the performance of DSSC made of a nanorice-like
TiO$_2$ powder and a reference P-25 TiO$_2$ powder. It is worthwhile to mention that

DSSC assembling parameters are first optimized for spherical shape P-25 TiO_2, and
such conditional parameters are also further taken as a reference for nanorice-like
TiO_2 [160].
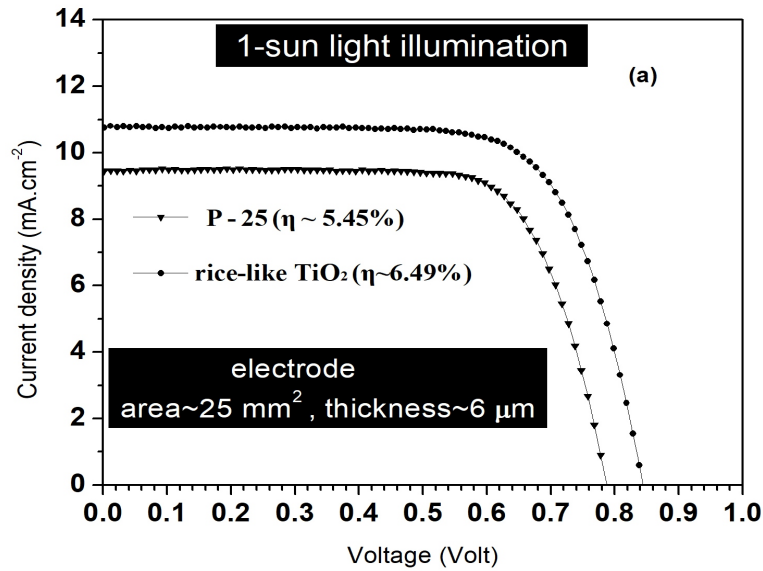
(a) Photocurrent-voltage characteristics nanorice-like anatase
TiO_2 and P-25 (see Table 1)

(b) Bode plots nanorice-like anatase TiO_2 and P-25 (see Table 1)

Figure 3.13: J-V and EIS characteristics of the samples

Figure 3.13(a) shows the measured photocurrent-voltage (V-I) characteristics of
cells. It evident that under identical standard 1 sun light illumination and fab-
rication condition of electrode; open-circuit voltage (V_{OC}) and short-circuit pho-
tocurrent density (J_{sc}) of nanorice-like TiO_2 electrode are much improved to that

of a reference P-25 electrode. Though reference P-25 showed a relatively better fill factor (FF) due to its advantageous compact electrode film made of nearly spherical shape nanoparticles, however η of nanorice-like TiO$_2$ electrode was much higher (ca. 20 % enhanced) in contrast to biphasial and isotropic P-25 TiO$_2$ electrode.

As evident in Figure 3.13(a), higher V$_{OC}$ of nanorice-like TiO$_2$ electrode could be attributed to its aforementioned pure phase and an enriched crystallinity i.e. sharp and intense XRD peaks. On the other side, along with crystallinity, enhanced J$_{sc}$ of nanorice-like TiO$_2$ electrode might have initiated with factors like larger dye-adsorption amount and a better electronic conductivity. However, a very little difference was observed for adsorbed amounts of photosensitizer (N719-dye) (see Table 3.1) in the interconnected mesoporous network of both isotropic P-25 as well anisotropic nanorice-like TiO$_2$, which could be understood in terms of a comparable BET surface area of the powder samples employed for electrode fabrication (see Table 3.1).

Therefore, in contrast to isotropic and biphasial P-25 electrode, it obvious that a higher J$_{sc}$ of nanorice-like TiO$_2$ electrode is expedited from an enriched crystallinity, pure phase and more importantly anisotropic shape that could possess a better charge conductivity in relation with a higher life-time (τ_{el}) for dye-injected electrons into CB of mesoporous oxide film structure to the back conducting FTO glass substrate [164]. The τ_{el} was estimated from Bode-phase plots of EIS measurements of respective electrodes (see Figure 3.13(b)). The peaks of characteristic frequency (f$_p$=1/2$\pi\tau_{el}$) of oxide/dye/electrolyte interface for anisotropic and isotropic electrode film were situated at 15.52 Hz and 20.58 Hz respectively, thus indicated an improved τ_{el} (ca.25 %) of dye-injected charge carriers in an anisotropic rice-like anatase TiO$_2$ film to that of a biphasial and spherical P-25 film. Such an improved τ_{el} is obvious as any well crystalline anisotropic charge conducting geometry provides a suppressed charge recombination due to lesser defects and traps in the electron film [160].

The reported HT synthesis can be considered as convenient and readily scalable process to synthesized nanorice-like TiO$_2$ nano particles for the application of efficient DSSCs. Moreover scaling TiO$_2$ electrode thickness is another methodology to improve PV performance of the cell. Microscopic simulations are preferable approach

for investigation of generation and recombination kinetics involved in the cell in order to achieve optimized electrode thickness with minimizing the fabrication cost. In chapter 4 a detailed analyses of microscopic simulated results are reported along with experimental results to describe the mismatched performance of the cell by adopting hybrid micro macroscopic simulations.

Chapter 4

Optimizing photovoltaic efficiency of a dye-sensitized solar cell (DSSC) by a combined (modelling-simulation and experimental) study

4.1 Introduction

The photovoltaic solar energy is one of the most growing industries which is continuously focusing on new techniques to enhance the global efficiency of the cells and also relating the cell performance with environmental conditions [165]- [170]. According to literature survey mentioned in [171]- [173], there is a wide variety of photovoltaic cell technologies in the marketplace today, using different types of materials and can be categorized into three generations, depending on the raw material used and the level of commercial maturity. First generation photovoltaic systems use the technology of crystalline as well as multi crystalline silicon solar cells. Second generation photovoltaic systems are based on thin film amorphous silicon; cadmium telluride (CdTe); copper indium selenide (CIS) and copper, indium gallium dieseline (CIGS). Third generation photovoltaic systems include organic photovoltaic technologies that are still in progress or have not been widely marketed and new concepts in development. Dye sensitized solar cells (DSSC) are one of the suitable example of light harvesting devices falls in third generation photovoltaic technology. The

first dye sensitized solar cells (DSSC) were proposed in 1991 by Michael Gratzel and Brian O'Regan. These cells belong to the group of hybrid solar cells, since they are formed by organic and inorganic materials. DSSCs have been extensively studied to minimize problems related to efficiency, cost of production and environmental issues [174]- [177]. The main difference of this type of cell compared to conventional solar cells is that the functional element which is responsible for the absorption of light (the dye) is separated from the transport mechanism of the charge carriers. Thus impure raw materials and simple cell processing techniques reduces the cost of the device.

Though a DSSC consists of multiple materials, yet it is a highly realized next-generation potential photovoltaic device that has been widely investigated due to its several advantageous competencies features like working even under a dim/low light and an achievable high value of η using a straight forward, cost-effective and eco-friendly manufacturing process. To obtain a higher η, the key challenges are thus to enhance specific role of individual components of a DSSC viz. working electrode (WE), counter electrode (CE), an electrolyte; the bulk interfaces and various complex processes occurring in a DSSC [178]. Among these components, WE (charge facilitator) is the heart of a DSSC, which is a dye (photosensitizer) coated porous nanostructured thin film of TiO_2 nanoparticles or other types oxides or nano-morphologies (wire/rod/rice/tube etc.) directly or indirectly fabricated onto an optically transparent conducting oxide (FTO) substrate [179]. On light irradiation, an excited dye injects electrons into film, which diffuses or recombines until finally collected at the back of FTO substrate [180]. Since a total charge collection depends on its generation, recombination and transportation, hence a dye of suitable energy band gap with a larger optical absorbance is required. Further, losses of charge carriers needed to mimicked by optimizing kinetics role of WE, light absorptivity/energetics of dye, transportation of redox ions and charge transfer at electrode/dye/electrolyte interface [181]- [183].

Interestingly, rather than optimized DSSC performance (J-V characteristics and η) by unwieldy cost-time consuming repeated fabrication/assembling processes, one could predict an optimum η in advance using much faster, safer, inexpensive and reliable alternative methods like modelling and simulation techniques [184]- [186].

In particular, an optimum J-V characteristic and a maximum achievable η of any logical circuit based theoretical DSSC model (ideally capturing all the underlying physical processes of a real time DSSC device) could be theoretically predicted as long as necessary experimental input data of at least one pre-assembled DSSC are available for initializing the simulation process. Based on well-calibrated theoretical models, the input or output simulated results along with controlled tuneable parameters can then be used as a reference for optimizing the performance of DSSC, which help in reducing the time and the fabrication/assembling cost, as only one more post-assembling process is required to achieve an optimum DSSC device.

Here in this chapter, the assembling and J-V characteristics of a sandwiched type DSSC assembled by a WE (L~3.0 μm) made from commercially available and nearly spherical shape TiO_2 nanoparticles (Degussa, P-25), an iodide /triiodide redox liquid electrolyte and photosensitizing dye N719 is reported. The measured J-V curve of assembled DSSC was generated by simulating a theoretical DSSC by TCMM-simulation (drift-diffusion of collective charge carriers) and SDMM-simulation in MATLAB (single p-n junction diode; Lambert W-function technique) [187]. The correlated and calibrated input model parameters (microscopic model: L, porosity, recombination kinetics, light absorbance of a N719 dye etc.; macroscopic model: shunt resistance $\sim R_S$, series resistance $\sim R_{SH}$ etc.) were further utilized in controlled simulation to achieve a maximum L corresponds to an optimum η of a DSSC device. The validation of correlated simulation and experimental output parameters (V_{OC} - open-circuit voltage; J_{SC} - short-circuit photocurrent density; FF- fill factor; η; P_{MAX}- maximum power density; V_{OPT} - voltage at P_{MAX}; J_{OPT} - current density at P_{MAX}) of DSSC are discussed together with pro and cons of input parameters of theoretical models.

4.2 Electrode fabrication, DSSC assembling and J-V measurements

Electrode fabrication and DSSC assembling were done according to the procedure as given in reference [160]. A homogenous paste was made by mixing P-25 powder, α-terpineol and ethyl-cellulose. This paste was screen printed on commercially

available F-doped SnO$_2$ (FTO; TEC 8) glass substrate. The TiO$_2$ electrode (active
area $\sim$0.25 cm^2; L$\sim$3.0 μm) was soaked in a 0.5 mM solution of N719 dye (ace-
tonitrile and tert-butanol 1:1 volume ratio) for 24 hours. As received N719 dye
from Solaronix has been used (no purification was done). The counter electrode
was Pt-coated FTO glass substrate. Dye coated electrode were rinsed in anhydrous
ethanol, dried in N$_2$ flow and a sandwich type DSSC has been assembled by stacking
and sealing electrodes (spacer of 60 μm thickness; thermoplastic Surlyn frame) filled
with a redox couple electrolyte (0.5 M 1-butyl-3-methylimidazolium iodide, 0.05 M
I$_2$, 0.5 M 4-tert-butylpyridine (TBP) in acetonitrile).

Electrical contacts were made by silver (Ag) soldering and Copper (Cu) wires. J-V
characteristics of an assembled DSSC were measured under 1 sun (100 mW/cm^2,
AM 1.5G) illumination with Peccell solar simulator (Model: PEL-L11). The mea-
sured output parameters (V$_{OC}$; J$_{SC}$; FF; η; P$_{MAX}$; V$_{OPT}$; J$_{OPT}$) of a DSSC are
listed in Table-4.2.

4.3 Theoretical modelling and simulation of a DSSC structure

With the current assembling and fabrication processes of a DSSC structure, the im-
pact of TiO$_2$ (L) on J-V characteristics curve is predicted and studied by a TCMM-
simulation under a static 1 sun light illumination. Further, it is assumed that a
total charge neutrality is maintained in modelling and simulation work. The results
of microscopic and macroscopic simulations are compared with the results of a real
time experimental work.

One-dimensional microscopic modelling-simulation is performed in multiscale *tiber*-
CAD software in which a set of drift-diffusion equations, continuity equations (eqn.4.1-
4.4), and Poisson's relation are used for facilitation of charge carriers (electrons, holes
and redox ions) describing the kinetics involved in the operation of DSSC and fur-
ther used to understand the kinetics involved in DSSSC (see Figure. 4.1) [188].

$$\Delta.(\mu_e n_e \Delta.\phi_e) = (G - R) \tag{4.1}$$

$$\Delta.(\mu_{I^-} n_{I^-} \Delta.\phi_{I^-}) = \frac{3}{2}(G - R) \tag{4.2}$$

$$\Delta.(\mu_{I_3^-} n_{I_3^-} \Delta.\phi_{I_3^-}) = (G - R) \tag{4.3}$$

$$\Delta.(\mu_c n_c \Delta.\phi_c) = 0 \tag{4.4}$$

Where $\mu_{I_3^-}$, μ_{I^-}, μ_e and μ_c are the mobility of I_3^-, I^-, electrons and cation; $n_{I_3^-}$, n_{I^-}, n_e and n_c are the concentrations of I_3^-, I^-, electrons and cation. G and R represent the generation and recombination rate of carriers as given by eqn. (4.10,4.12). The purpose to consider cation is to maintain charge neutrality of the device and there will be no current contribution due to cation. We assume valid Einstein's relation (eqn.4.5) between mobility (μ) and diffusion coefficient (D), where k is Boltzmann constant, T is temperature and e is charge on electron.

$$D = \frac{kT}{e}\mu \tag{4.5}$$

The concentration of the various species in a cell is governed by Maxwell–Boltzmann distribution and given by eqn. (4.6-4.9) under equilibrium condition.

$$n_e = N_{CB}exp(-kT(e\varphi - e\phi - E_c)) = \bar{n}_e exp(-kTe(\varphi - \phi)) \tag{4.6}$$

$$n_{I^-} = \bar{n}_{I^-} exp(-kTe(\varphi - \phi_{I^-})) \tag{4.7}$$

$$n_{I_3^-} = \bar{n}_{I_3^-} exp(-kTe(\varphi - \phi_{I_3^-})) \tag{4.8}$$

$$n_c = \bar{n}_c exp(-kTe(\varphi - \phi_c)) \tag{4.9}$$

where E_c is the conduction band (CB) edge in TiO$_2$, φ is the electrical potential, N$_{CB}$ is the effective density of states in TiO$_2$ conduction band and ϕ is the electrochemical potential. The barred quantities in chemical equation refer to the equilibrium concentrations at no sunlight condition. The generation term (G) related to the flux of photons which absorbed by the dye coated active TiO$_2$ regions. The generation rate (G) is evaluated by considering the dye absorption spectrum (N719) in the present study of DSSC [189]- [191] and defined by the eqn. (4.10).

$$G(x) = \int_{400\,nm}^{800\,nm} (\alpha(\lambda)\psi(\lambda)e^{-\alpha(\lambda)x})dx \tag{4.10}$$

where $\psi(\lambda)$ is the spectral power flux simulating a standard solar illumination on at 1 sun. Parameter $\alpha(\lambda)$ is the absorption coefficient of the dye chemisorbed on the TiO_2 . Above 800 nm, the absorption of the dye is quite small.

The recombination depends on the loss mechanisms at the electrolyte/TiO_2 interface [192]. The principal losses occur when an electron from the CB of TiO_2 recombines with the triiodide. In the case of a DSSC, the charge transfers occur at the interfaces of the electrolyte with the Pt contact and with the TiO_2. The total reaction of I_3^-/I^- redox electrolyte is a two-electron reaction (eqn. 4.11) [193].

$$I_3^-(electrolyte) + 2e(TiO_2) = I^- \tag{4.11}$$
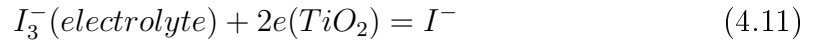
The recombination rate, R is governed by the eqn. (4.12) and mainly affected by recombination constant rate k_e (for recombination path r_3), concentration of electrolytes, electron density and β is the exponent for the electron density.

$$R = k_e \left(n_e^{\beta} \sqrt{\frac{n_{I_3^-}}{n_{I^-}}} + \bar{n}_e^{\bar{\beta}} \sqrt{\frac{n_{I_3^-}}{n_{I^-}^{-3}}} n_I^- \right) \tag{4.12}$$

Beside drift-diffusion equations, the Poisson's equation (eqn. 4.13) is considered for the internal potential drop in the cell with dye generation rate G and k_3 (dye regeneration rate constant) for oxidized dye molecule concentration,N_D^+ (eqn. 4.14).

$$-\varepsilon\Delta\varphi = e(n_c - n_{I_3^-} - n_{I^-} - N_D^+ - n_e + \bar{n}_e) \tag{4.13}$$

$$N_D^+ = \frac{G}{k_3} \tag{4.14}$$

Redox energy level of the electrolyte is expressed by the Nernst equation and given by eqn. (4.15). The I_3^-/I^- boundary conditions at the cathode are related to a Butler–Volmer (BV) eqn. (4.16-4.18) and controlled by the concentration of redox species. $j_{cathode}^0$ is the exchange current density, which describes the charge transfer between Pt and I_3^- at equilibrium; Δn_{I^-} and $\Delta n_{I_3^-}$ are the diffusion over potential. All the barred terms represents respective quantities in dark condition. E_0^{redox} is the standard redox potential; where L is the length of the electrode and represents the current density.

$$E_{redox} = E_{redox}^0 + \frac{kT}{2} ln \left(\frac{n_{I^-}^{-3} n_{I_3^-}^-}{n_{I^-}^3 n_{I_3^-}^-} \right) \tag{4.15}$$

$$j = j_{cathode}^0 \left(\exp^{\frac{\beta e}{kT} \Delta n_{I_3^-}} - \exp^{\frac{-(1-\beta)e}{kT} \Delta n_{I^-}} \right) \tag{4.16}$$

$$\Delta n_{I_3^-} = \frac{kT}{e\beta} ln \left(\frac{n_{I_3^-}(L)}{n_{I_3^-}} \right) \tag{4.17}$$

$$\Delta n_{I^-} = \frac{kT}{e(1-\beta)} ln \left(\frac{n_{I^-}(L)}{n_{I^-}} \right) \tag{4.18}$$

The BV equation fixes the total current density that must split between I_3^- and I^- species. Beside the boundary conditions (eqn. 4.19-4.21), simulations also included two other constraints for these two ionic species (eqn. 22-24).

$$\int_0^d (n_{I^-}(x) + 3n_{I_3^-}(x))dx = (n_{I^-}^- + n_{I_3^-}^-)L \tag{4.19}$$

$$\int_0^d n_c(x)dx = \bar{n}_c d \tag{4.20}$$

$$\Delta.(\mu_{I^-} n_{I^-} \Delta.\phi_{I^-}) = \frac{1}{2e}j \tag{4.21}$$

$$\Delta.(\mu_{I_3^-} n_{I_3^-} \Delta.\phi_{I_3^-}) = -\frac{3}{2e}j \tag{4.22}$$

All the above equations (eqn. 4.1-4.22) are implemented in a finite-element solver *tiber*CAD by considering equivalent 1 D structure of DSSC as shown in Figure. 4.2, that produced the several DSSC results viz. I-V characteristic curves, density profiles, total recombination etc. [194].

In this microscopic model (see Figure 4.1), all injected electrons are considered from the excited state of dye only, and not from TiO$_2$ band gap excitation. The trapping and de-trapping of dye-injected electrons is neglected in an electrode irrespective to

its L value [195]. This model consisted of two regions: 1) mesoporous electrode of TiO_2 nanoparticles surrounded by a liquid electrolyte; and 2) a liquid electrolyte in contact with a counter-electrode (covered by a thin Pt-layer) [196]- [198]. Optical losses caused by a liquid electrolyte are not included and it is assumed that each absorbed photon injected one electron into conduction band of TiO_2. Moreover, it should be noted that only one dominant electron recombination loss mechanism ($r_3 \rightarrow$between TiO_2 and electrolyte; see Figure 4.1) is considered in the present microscopic model [199].
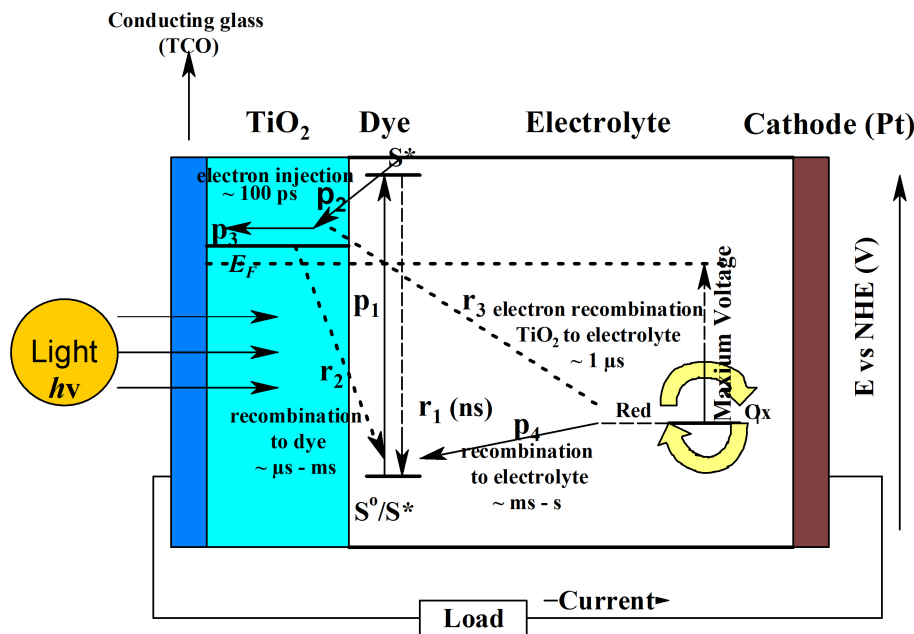

Figure 4.1: Illustration showing the working principle and the components of a DSSC structure, where dash arrows represented the various paths (time-scales) for electron loss.

Macroscopic modelling-simulations are performed in MATLAB tool. A non-ideal single-diode model is used (see Figure 4.3; eqn. 4.23) for keeping the simplicity and an accurate representation of simulation results (minimum error in a nonlinear J-V curve) of a DSSC structure. This model consist of: 1) a photocurrent source (J_L; depends upon light irradiance) connected in parallel with a non-ideal diode (n, ideality factor; J_0, saturated dark current density) 2) a series resistance (R_s; capturing total resistive losses within cell) and 3) a shunt resistances (R_{sh}; representing losses due to an increased conductivity at junction/edges of cell) [200]. Based on Schokley

theory of a p-n junction diode, the J-V characteristics curve of such a non-ideal single-diode model [201]- [202] is mathematically expressed by eqn. 4.23, where V_T is the thermal voltage. Due to implicit transcendental form of this eqn. 4.23, it is quite tedious task to extract individual diode parameters by a common least-square curve fitting method, therefore this cumbersome extraction process was made simple by changing the implicit form into an explicit form with the application of a Lambert W-function (see eqns. 4.24 and 4.25) [203].
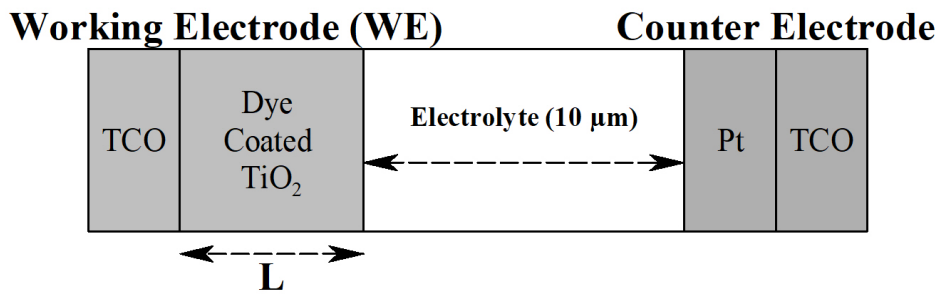

Figure 4.2: 1-D microscopic DSSC model used in *tiber*CAD software (only significant loss mechanism r$_3$ of Figure. 4.1 is used in simulation)
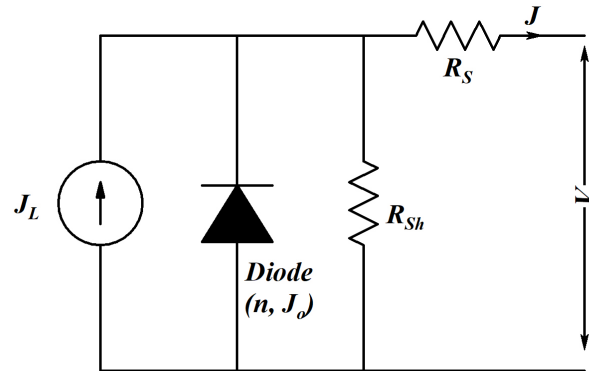

Figure 4.3: 1-D macroscopic electrical DSSC model used in MATLAB simulation

Precautions were taken during simulations, as the accuracy of extracted input parameters (J$_L$, J$_0$, n, R$_s$ and J$_{sh}$) depends on the choice of their initial surmise, which may tend to lead a non-convergence equation. Moreover, as the number of fitting parameters increases, the non-linear fitting method loses their ability to give the accurate results.

4.4 Correlations between Simulation and Experimental Results

By considering the pre assembled DSSC based on a WE (N719 adsorbed nanoparticles based TiO$_2$ electrode, active area $\sim$ 0.25 cm^2, L $\sim$ 3.0 μm), a liquid redox couple electrolyte I$_3{}^-$/I$^-$ and counter Pt-electrode,the J V characteristics obtained experimentally (see Figure. 4.4) is utilized to calibrate the simulation parameters of the *tiber*CAD software by performing TCMM simulations for 1-D microscopic DSSC device model (see fig.4.2) under standard 1 sun light illumination conditions. The calibrated parameters are noted down (Table 4.2) after achieving close fit between the experimental and simulated results (see Figure. 4.4 and Table 4.1).

$$J = J_L - J_o \left(exp\frac{V + JR_{sh}}{nV_T} - 1 \right) - \frac{V + JR_s}{R_{sh}} \tag{4.23}$$

$$J = \frac{R_{sh}(J_L + J_o) - V}{R_s + R_{sh}} - \frac{nV_T}{R_s}W(Q) \tag{4.24}$$

$$Q = \frac{J_o R_{sh} R_s}{nV_T(R_s + R_{sh})} \left(\frac{(R_{sh}(R_s J_L + R_s J_o + V))}{nV_T(R_s + R_{sh})} \right) \tag{4.25}$$

Table 4.1: Experimentally measured results* and simulated** DSSC PV performance parameters

J$_{SC}$ mAcm^{-2}	V$_{OC}$ (V)	V$_{OPT}$ (V)	J$_{OPT}$ mAcm^{-2}	P$_{MAX}$ mWcm^{-2}	FF (%)	η (%)
5.95**	0.812**	0.71**	7.74**	5.495**	84.2**	4.07**
5.94*	0825*	0.66*	5.2*	3.432*	72.5*	3.55*

Along with the experimentally measured results, the simulated output DSSC parameters are listed in Table 4.1. A discrepancy in a FF (and η) among experimental and simulated J-V characteristics curves is clearly observed in Figure 4.4, and such mismatch in FF is more pronounced in a non-linear region of J-V curves. This mismatch can be understood in terms of limitations imposed in model software, particularly neglecting the resistance contribution of a FTO substrate in a WE is one of the key limitations of TCMM (*tiber*CAD) simulations. Despite of an overestimation in FF, however it is clear form Table 4.1 that at-least V$_{OC}$ and J$_{SC}$ obtained through real time experiments and theoretical microscopic model-simulations matches well

for a TiO_2 electrode (L $\sim$ 3.0 μm) and provides motivation to carry out further simulations for various electrode thicknesses.
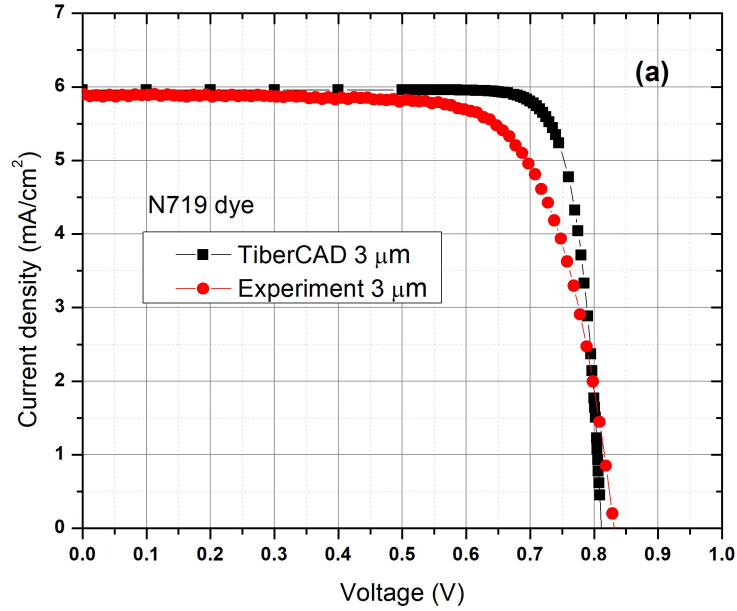

Figure 4.4: TCMM-simulation and experimental J-V characteristic curves of a DSSC at L$\sim$3.0 μm

Table 4.2: Calibrated input parameters obtained by microscopic modelling–simulations of 1D DSSC model at L = 3 μm thick TiO_2 electrode (see Figure 4.4)

S.No	Input parameters (for TCMM simulations)	Calibrated values
1	Electron relaxation rate, k_e	0.07×10^4 s^{-1}
2	Electron mobility, μ_e	0.02 cm^2/V s
3	Iodide difusion constant, D_{I^-}	8.5×10^{-6} cm^2/s
4	Triiodide difusion. constant, $D_{I_3^-}$	8.5×10^{-6} cm^2/s
5	Initial conc. of iodide,$[I^-]$	0.45 M
6	Initial conc. of triiodide,$[I_3^-]$	0.45 M
7	Recombination exponent, β	0.75
8	Cell porosity, P	0.5
9	Cell area, A	0.25 cm^2

By adapting all the calibrated input parameters of Table 4.2 as references, TCMM-simulation is repeated for various L (6.0 $\rightarrow$ 18.0 μm) of a WE, so that more meaningful (qualitative and quantitative) insights could be gain about the L dependency of output parameters.

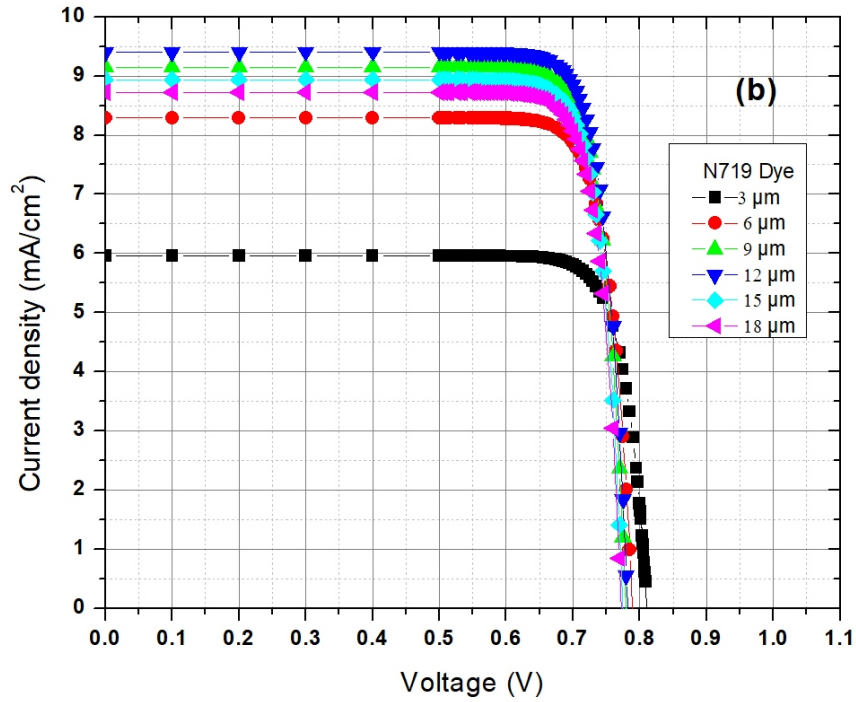Figure 4.5: TCMM-simulation J-V characteristic curves of a DSSC at L (3 → 18 μm)

4.5   Results and Discussion

By considering results of TCCM simulation (see Figure 4.4; Table 4.3), three more DSSC devices for different L (6.0, 9.0 and 12.0 μm) of a WE are fabricated/assembled and characterized (see section 4.2). Experimental values together with simulated output parameters of such devices are listed in Table 4.3, and for quick and simple observations, their L dependency behaviors are plotted in Figures 4.6-4.9 and Figure 4.11.

From Table 4.3 or Figures 4.6-4.9, a systematic WE (L) dependency of various DSSC output parameters (V_{OC}, J_{SC}, FF, η) is clearly noticeable i.e. an increasing J_{SC} ($\sim$5.95→9.4 mAcm^{-2}) with an increasing thickness ($\sim$ 3→12 μm) and then a decreasing J_{SC} for other higher values of thicknesses (above 12 μm). Additionally, η of a DSSC WE follows the similar tendency (see Figure 4.6), while exhibiting its optimum ($\eta \sim$ 6.23 %) for a particular WE (L $\sim$ 12.0 μm). Despite of having a much higher η in simulated J-V characteristics plots, above results suggested that η is indeed essentially determined by J_{SC}, and its trend is fully verified by the experimental measurements (see Figures 4.6-4.9; Table 4.3) [204]. As the light transmitted into the depth of a WE, a gradual decrease in power density of light takes place and

85

excessive electron density becomes lower, therefore results in decrease in V_{OC} (0.812 $\rightarrow$ 0.78 V) in an initial range of L, 3.0$\rightarrow$9.0 μm [205]- [207]. For further increments in L (12.0 $\rightarrow$ 18.0 μm), V_{OC} shows insignificant variation [208] and settled at close to 0.78 V. Moreover, comparison of the simulated parameters with experimental measurements, the significant variation could be easily interpreted in terms of typical L dependent behaviour of J_{SC} caused by two competing simultaneous and contradictory kinetics occurring a WE i.e. generation and recombination of charge carriers in an assembled DSSC structure (See Figure 4.1) [209].
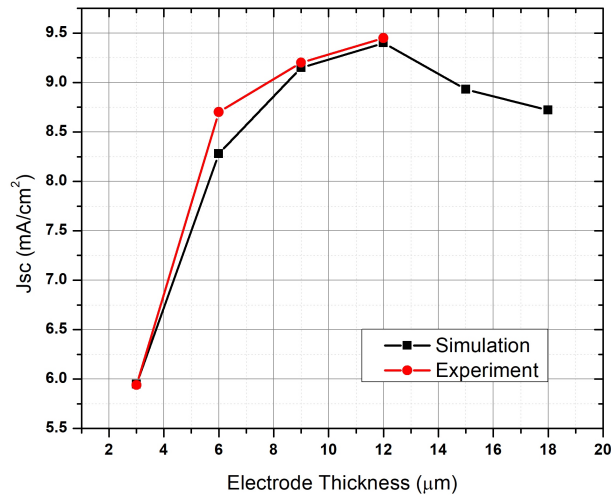

Figure 4.6: TCMM-simulation and experimental output parameter; J_{SC} of a DSSCs obtained under 1 sun illumination for various L of a TiO_2 electrode
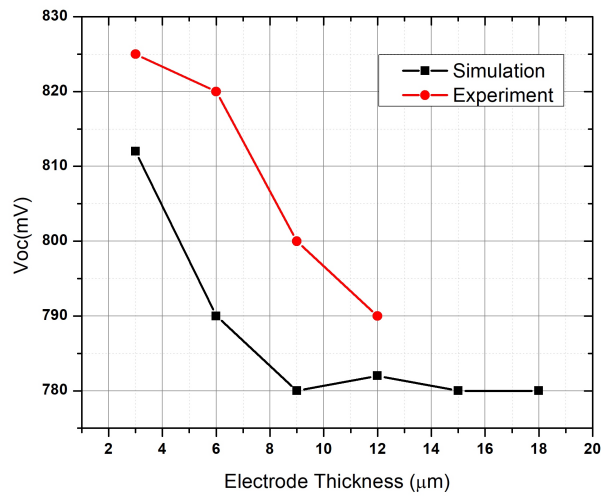

Figure 4.7: TCMM-simulation and experimental output parameter; V_{OC} of a DSSCs obtained under 1 sun illumination for various L of a TiO_2 electrode
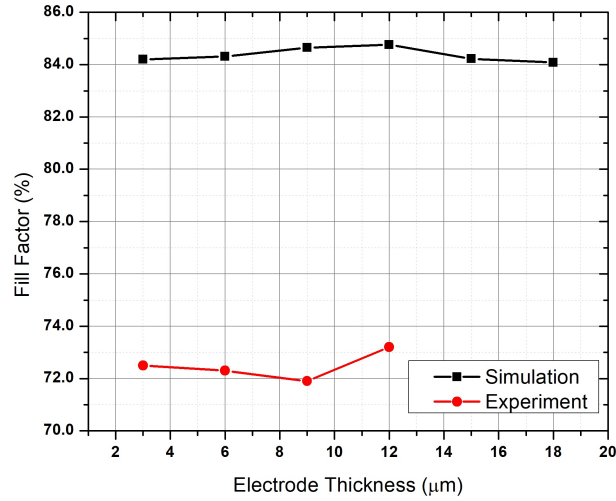
Figure 4.8: TCMM-simulation and experimental output parameter;FF of a DSSCs
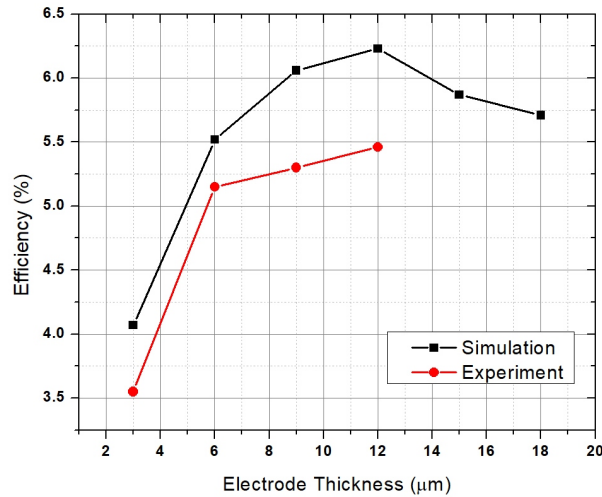obtained under 1 sun illumination for various L of a TiO$_2$ electrode

Figure 4.9: TCMM-simulation and experimental output parameter; η of a DSSCs
obtained under 1 sun illumination for various L of a TiO$_2$ electrode

The incomplete dye covering together with a lack of light intensity deep into
a thicker WE lead a gradual decrease in its J$_{SC}$. Besides this, a thicker WE film
offers more bulk resistance at the interconnected grain boundaries of TiO$_2$ nanoparticles [210]- [211].

Based upon the above discussions i.e. a subtle balance between two opposite charge
transport kinetics (see Figure 4.1) and adopting the calibrated input model parameters of a reference WE (see Figure 4.1; Table 4.2) in microscopic modelling-simulation studies, L $\sim$12 μm (see Figures 4.6-4.9; Table 4.3 and 4.4; FF $\sim$ 84.76
%; V$_{OC}$ $\sim$ 0.782 V; J$_{SC}$ $\sim$ 9.4 mAcm^{-2}; η $\sim$ 6.23 %; J$_L$ $\sim$ 9.49 mA^{-2} and R$_S$ $\sim$

29.37 mΩcm^2 ; see Table 4.3 and 4.4) was estimated as optimum L of a WE, as fully
supported by the aligned parallel experimental measurements. Note that R$_S$ or R$_{SH}$
values (see Table 4.4 of an individual WE are estimated from a slope of J-V curve
using SDMM simulations, while neglecting the contribution (resistance in R$_S$) of a
FTO in J-V curves.

Table 4.3: Experimentally measured results* and simulated** DSSC PV perfor-
mance parameters

Parameter	L= 3 μm	L= 6 μm	L= 9 μm	L= 12 μm	L= 15 μm	L= 18 μm
J$_{SC}$ mAcm^{-2}	5.95** 5.94*	8.28** 8.70*	9.15** 9.2*	9.4** 9.45*	8.93** - -	8.72** - -
V$_{OC}$ (V)	0.812** 0.825*	0.79** 0.82*	0.78** 0.80*	0.782** 0.79*	0.78** - -	0.78** - -
V$_{OPT}$ (V)	0.71** 0.66*	0.695** 0.647*	0.685** 0.63*	0.69** 0.616*	0.685** - -	0.68** - -
J$_{OPT}$ mAcm^{-2}	7.74** 5.2*	7.943** 7.97*	8.82** 8.39*	9.03** 8.8*	8.57** - -	8.41** - -
P$_{MAX}$ mWcm^{-2}	5.495** 3.432*	5.52** 5.15*	6.04** 5.29*	6.23** 5.42*	5.87** - -	5.718** - -
FF (%)	84.2** 72.5*	84.31** 72.30*	84.65** 71.9*	84.76** 73.2*	84.22** - -	84.08** - -
η(%)	4.07** 3.55*	5.52** 5.15*	6.06** 5.3*	6.23** 5.46*	5.87** - -	5.71** - -

Figure 4.6-4.9 and Table 4.4 clearly depict that for a particular WE (L~12 μm), the
high percentage values of FF (~16%) and η (~14%) obtained in TCMM-simulations
as compared to their experimental values, are consequences of assumptions made by
model simulation software (*tiber*CAD), particularly as FTO series resistance could
not be taken into simulations. Therefore, the effects of L on J-V curves are further
investigated in MATLAB using SDMM-simulation with an application of a Lambert
function (see Figure 4.3; eqn. (4.23-4.25)). For SDMM simulations, previously as
resulted TCMM-simulations and experimental J-V curves of various L are taken as
inputs, and a better fitting is achieved by applying a least square fitting method
within a minimum permissible error range (SSE = 8.5×10^{-7} to 5×10^{-6}, R square =
0.9965 to 0.9974, RMSE = $1 \times^{-4}$ to 1×10^{-3}).
The extracted macroscopic model input parameters (J$_L$, J$_0$, n, R$_s$ and R$_{sh}$) for differ-
ent values of L (TCMM simulated J-V characteristics; see Figure 4.5) are reported
and compared in Table 4.4. For all L of a WE, Table 4.4 depicts a much lower

(ca. $\sim 10^3$ fold) magnitude of R_s resulted in TCMM-simulation than to its values
extracted from experimental J-V curves.

Table 4.4: Experimentally measured results* and simulated** DSSC PV performance parameters

L	R_s (mΩcm^2)	R_{sh} (KΩcm^2)	(n)	J_o	J_L
3 μm	106.6**	66.95**	1.389**	1.024**	6.087**
	11.32x10^3*	63.2*	1.432*	1.88*	5.82*
6 μm	67.4*	92.42*	1.35*	1.4*	8.48*
9 μm	37.62*	97.06*	1.292*	0.7*	9.38*
12 μm	29.37**	973**	1.365**	2.55**	9.49**
	7.07x10^3*	82.5*	1.39*	3.4*	9.04*
15 μm	40.11*	151*	1.263*	0.48*	9.04*
18 μm	80.42*	117*	1.365*	3.142*	8.93*

The drastically lowered values of R_S closely reflected a much higher FF and η for
all L of a WE as reflected in all TCMM-simulations. To overcome the limitation
of TCMM-simulation, the FTO resistance is considered through the combination of
TCMM-simulation and SDMM-simulation, and this combined approach is referred
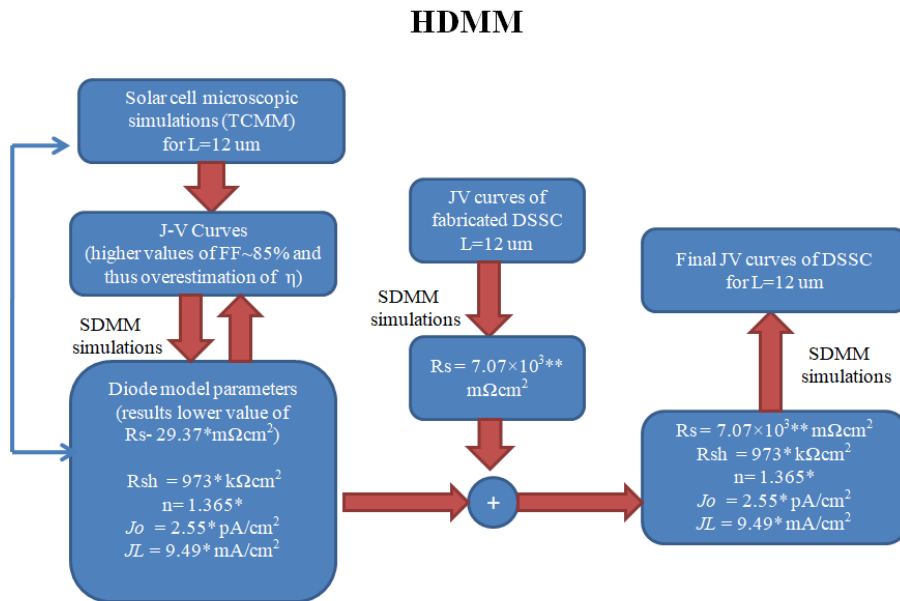as hybrid micro-macroscopic model simulation (HDMM-simulation).
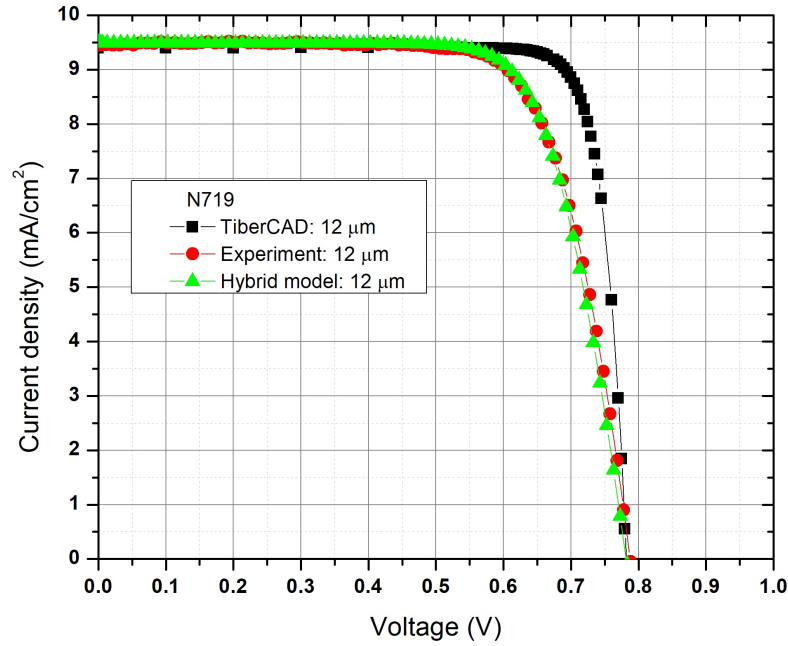

Figure 4.10: HDMM-simulation model

Figure 4.11: Experimental and TCMM-simulation J-V characteristics curves
obtained under 1 sun light illumination for an optimized DSSC (L=12 μm) along
with HDMM simulation curve by considering FTO resistance (7.07×10^3 mΩcm^2)

Figure 4.11 shows the comparison of J-V curves among an experimental, a TCMM-simulation and a HDMM-simulation for a DSSC producing a maximum η for a particular L (ca$\sim$12 μm) of a WE. It is clear that a very close fitting of performance parameters of the solar cell (see Table 4.5) is obtained between J-V curves obtained by a real time experiment and a HDMM-simulation. Moreover, a dramatic influence a FTO resistance in R_s (unaccounted in microscopic model and a counted in macroscopic model) and curve fitting is clearly noticed. The last column in Table 4.5 shows the percentage error in HDMM-simulation with their real time measured experimental values. The maximum percentage error in η and FF is found to be $\eta \sim$ 0.06 % and 0.52 % respectively, between measured experimental values and HDMM simulations.

Additionally, the variation of photocurrent density (J_L) with L is entirely consistent with the dependency of R_S on L value (see Figure 4.12). The R_S is determined to be a minimum for a particular TiO$_2$ electrode (L$\sim$ 12 μm), and this could be explained by considering the two simultaneously competing contradictory mechanisms occurring in an electrode i.e. generation and recombination of charge carriers in an assembled DSSC structure [212]- [213].

Table 4.5: Comparison among TCMM-simulation, Experimental and HDMM-simulation parameters for an optimized DSSC structure consisting a TiO_2 electrode (thickness L=12 μm, 0.25 cm^2).

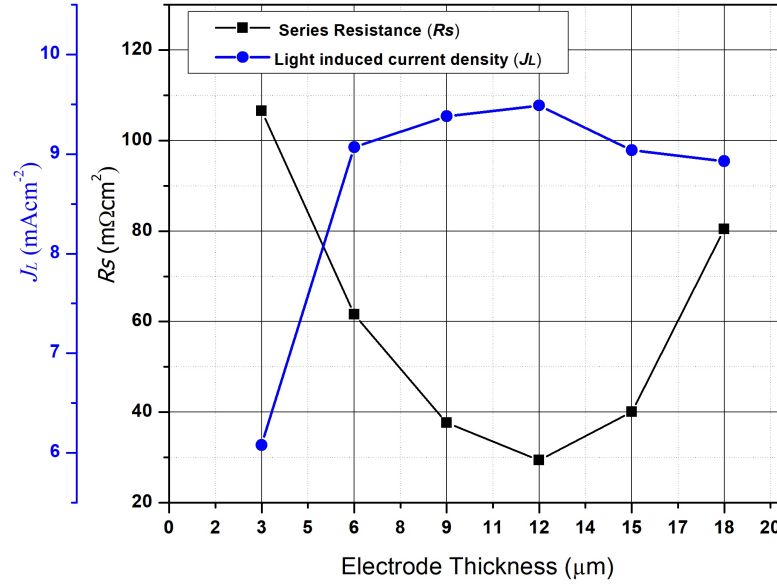| Parameter	Microscopic simulations TCMM	Experimental results (Exp)	Hybrid Model simulations	% error Exp - TCMM	% error Exp–Hybrid model
R_S mΩcm^2	29	7.07x10^3	7.07x10^3	99.58	0
J_{SC} mAcm^{-2}	9.4	9.45	9.49	0.53	0.423
V_{OC} (V)	0.782	0.79	0.783	1.012	0.886
V_{OPT} (V)	0.69	0.616	0.613	12.013	0.487
J_{OPT} mAcm^{-2}	9.03	8.8	8.92	2.613	1.363
FF (%)	84.76	73.2	73.58	15.8	0.52
η(%)	6.23	5.464	5.467	14.02	0.055

Figure 4.12: Thickness dependent output parameter (R_S, J_L) of a DSSC TiO_2 electrodes obtained by SDMM simulations performed in MATLAB

Increasing the thickness of WE increase the dye absorbance in the TiO_2 porous voids thus enhance the light absorbance in the photoanode (WE) and further increases the density of photo- generated carriers. Hence photo current density increases but at the same instant of time, series resistance of the electrode also tends to increase in order to affect the cell performance.

It can be understood from the above results shows that scaling the electrode thickness shows improvement in PV performance of the DSSC. However, the performance of the cell is directly depends on the mechanism of the charge transfer processes oc-

curring inside the cell. Thus it is essential to explore the electron transport properties impacting net charge transportation and accumulation at the various interfaces and bulk regions present in the cell. In chapter 5, electrochemical impedance spectroscopy (EIS) analysis is employed for analyzing these mechanisms describing the relationship between the cell's performance and its architecture.

Chapter 5

Analysis of charge transport properties of dye sensitized solar cell (DSSC) with TiO$_2$ working electrode by employing electrochemical impedance spectroscopy (EIS)

5.1 Introduction

Electrochemical impedance spectroscopy (EIS) is widely preferred technique to elucidate the charge transfer (CT) and transport properties of the DSSCs [214]- [227]. It is a steady state approach that measures the current response as a function of frequency to the application of an AC voltage.

This chapter reports the Electrochemical impedance spectroscopy (EIS) characteristics of a sandwiched type DSSCs assembled by a WE (L= 3 μm $\rightarrow$12 μm) made from commercially available and nearly spherical shape TiO$_2$ nanoparticles (Degussa, P-25), an I$_3{}^-$/I$^-$ redox liquid electrolyte and photosensitizing dye N719 (as discuused in chapter 4). EIS is employed on DSSCs in order to insight on many significant processes taking place inside the cell of in order to investigate the charge transport, transfer, and accumulation in DSSC such as: (i) electron percolation inside TiO$_2$ film through diffusion and I$_3{}^-$/I$^-$ diffusion in the electrolyte solution; (ii) recombination

(e-$I_3{}^-$) at TiO_2/electrolyte (T-E) interface (iii) regeneration of I^- at Pt/electrolyte
(P-E) interface; and (iv) capacitive elements inside cell including interfaces, CB, and
across the TiO_2 network [215], [218]- [222]. The Nyquist diagram usually involves
three semicircles attributed to the Nernst diffusion inside the electrolyte, the electron
transfer at the oxide/electrolyte interface, and the redox reaction at the platinum
counter electrode in the order of increasing frequency. The characterized EIS spec-
trums (nyquist and bode plot) are further utilized to investigate the charge transfer
and transport properties of the DSSC fabricated for electrode thicknesses (L) from
3 μm - 12 μm (discussed in chapter 4) by curve fitting method using EIS spectrum
analyzer software. EIS sectrum were measured using a reference 600 potentiostat
(Gamry Instruments) under 1 sun in the open-circuit condition.

5.2   Fundamentals of EIS

The net impedance over a wide range of frequency ($\omega = 1/2\pi$f) across the circuit el-
ement of the electrical network is computed by measuring the ac current on applying
ac input voltage across the circuit element. The eqn. (5.1) is used to calculate the
resulting impedance Z(ω) of the system [214]- [215], [217] provided that I(ω, t), is
sufficiently small to be linear in relation to V(ω, t) or vice versa. Depending on the
numerous CT process taking place inside the DSSC, V(ω, t) and I(ω, t) may differ
amplitude and phase at a range of certain frequencies (f) resulting in the impedance
for the corresponding CT process. Any electrical network is said to be powered with
dc current when the frequency (f) of the applied voltage source is close to 0 Hz, and
the network's impedance is evaluated by its DC resistance (R_{dc}), i.e. zero phase
impedance is given by eqn. (5.2) [215], [223]:

$$Z(\omega) = \frac{V(\omega, t)}{I(\omega, t)} \tag{5.1}$$

$$Z(0) = \frac{V(0, t)}{I(0, t)} = R_{dc} \tag{5.2}$$

For an small signal AC input voltage described by V(ω, t)= V_0. $e^{-j\omega t}$, generates AC
current which is expressed by I(ω, t) = I_0. $e^{-j\omega(t-\theta)}$. It is clearly shown that there
is a phase difference (θ) appearing between voltage and current. Eqn.(5.1) can be

written as eqn. (5.3).

$$Z(j\omega) = \frac{V_0}{I_0} e^{-j\omega} \tag{5.3}$$

Again, eqn. (5.3) can be also expressed in terms of magnitude of net impedance (|Z|) and given by eqn. (5.4)

$$Z(j\omega) = |Z| e^{-j\omega} \tag{5.4}$$

After applying Euler's theorem eqn. (5.4) can be expressed by eqn. (5.5)

$$Z(j\omega) = |Z|(cos\theta + jsin\theta) \tag{5.5}$$

The total impedance of the electrical network is expressed by eqn. (5.6) [13,16]

$$Z(\omega) = Z_{Re} + jZ_{Im} \tag{5.6}$$

where $Z_{Re} =$|Z|.$cos\theta$ and $Z_{Im} = $|Z|.$sin\theta$ are representing real and the imaginary impedances of Z(jω) respectively. Impedance's magnitude (|Z|) and θ are expressed as eqn. (5.7) and eqn. (5.8) respectively.

$$|Z| = \sqrt{Z_{Re}^2 + Z_{Im}^2} \tag{5.7}$$

$$\theta = \tan^{-1}\left(\frac{Z_{Im}}{Z_{Re}}\right) \tag{5.8}$$

There are various ways to display the computed EIS data to analyze CT characteristics of the DSSC. One of the plots termed as Nyquist plot where is plotted against Z_{Re} in the complex plane. Plotting of other parameters from EIS curves; log|Z| and θ as a function of logf is known as Bode plot. Moreover plotting Z_{Im} against logf also helps to investigate the charge recombination properties inside the cell [214]- [217].

5.3   EIS Spectra of DSSCs

The process involved in CT and electron loss mechanism involved in DSSC is shown in Figure 5.1 where path (1) represents the electron injection process. The charge injection efficiency depends on the energy gap between LUMO level (lowest unoccu-

pied molecular orbital) of dye and CB of TiO_2 and capability of the dye molecules
anchored on the surface of TiO_2 nanoparticles. These properties regulates the elec-
tron injection time at dye/TiO_2 interface. After injection process, electron transport
towards FTO glass by diffusion process through path (2).
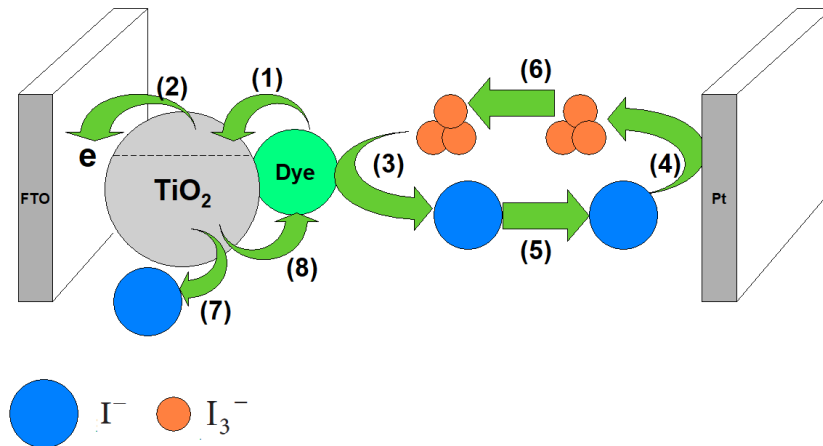

Figure 5.1: Representation of CT kinetics(1) e-injection process, (2) e-diffusion
inside TiO_2 film, (3) dye regeneration (4) regeneration kinetics of I_3^-/I^- (5)
diffusion of I_3^- in electrolyte solution (6) diffusion of I^-, (7)recombination of TiO_2
CB electrons with I_3^- and(8)e-S^+ recombinations

The ability of electron diffuses inside the network of TiO_2 nano particles is governed
by the diffusion resistance offered by TiO_2 network which further depends on the
electron recombination process taking place at the surface of TiO_2 (T-E interface)
or inside the bulk of TiO_2. It can be assumed that electrolytes ions (I_3^-/I^-) present
uniformly in the solution. The triiodide redox electrolyte diffuses towards the oxi-
dized dye molecules and regenerates them through path (3) and gets self oxidized
into iodide ion. This dye reduction process enhances the concentration gradient of
iodide ions which furthers tends to diffuse the iodides towards the Pt coated FTO
glass so that it get reduced to form triiodide ions (path (4)) to maintain the dye
regeneration kinetics in the cell. It can be easily understood that better diffusion
property for path (6) and path (5) of the electrolyte ions are required in electrolyte
solution to maintain the redox reactions in the cell. So in terms of electrical quan-
tity, it can be also understood that electrolyte solution should provide lower diffusion
resistance for the electrolyte ions for faster redox reactions in order to enhance re-
generation of redox mediator (I_3^-/I^-). The oxidized dye molecules may also get

reduced by capturing electron from the TiO$_2$ network through path (8) and this path can be considered as the recombination path. However, the dominant electron loss mechanism can be given by the electron capturing by triiodide ions through path (7) which is further influenced by the charge recombination kinetics involved at the T-E interface. Charge recombination kinetics further decides the charge recombination across the T-E interface i.e. higher the CT resistance at T-E interface lower is the electron recombination through path (7) or vice versa. From the above discussion it can be illustrated that performance of the DSSC fabricated with various electrode thicknesses (L = 3 μm $\rightarrow$12 μm) can be also expressed in terms of impedances in the bulk and at the interface regions present in the cell.

Employing EIS determines the current response as a function of frequency by applying ac input voltage V(ω,t) resulting Nyquist plots usually involves three semicircles (I-III) corresponds to different charge transport process at the interface and inside the components of the DSSC. A DSSC is usually composed of a photosensitive (N719,N3,LEG4) dye adsorbed on FTO glass substrate coated with mesoporous film of nanocrystalline TiO$_2$ which acts as working electrode WE, an I$_3^-$/I$^-$ derived redox couple, and an Pt-FTO glass substrate acting as CE. The photo electrochemical processes, including electronic and ionic processes (diffusion and recombination) taking place in the DSSC has been widely investigated by EIS.

A well frequency distribution of several time constants for the different CT paths (paths 1-8) gives rise to three distinct arcs as shown in Figure. 5.2(a) or representing three distinct peaks in plotted in Bode plot (see Figure. 5.2(a)) of EIS of a DSSC. The theoretical and experimental approach [224]- [228] has been used to assign these semicircles in the EIS spectrum to the corresponding CT processes. The three semicircles are clearly depicted from the Figure. 5.2(a). As traversing towards $\omega = 0$ rad/s, the semicircle - I (near $\omega \sim \infty$ rad/s) representing the CT processes taking place at Pt/electrolyte interface with a characteristic frequency ω_{CE}, the second (II) or middle semicircle corresponds to the electron diffusion in the TiO$_2$ film and electron back reaction with I$_3^-$ at the TiO$_2$/electrolyte interface at characteristic frequency ω_d and ω_k respectively, and the third (III) semicircle plotted near low frequency region corresponds to the diffusion of I$_3^-$ ions in the electrolyte solution with a characteristic frequency ω_D.
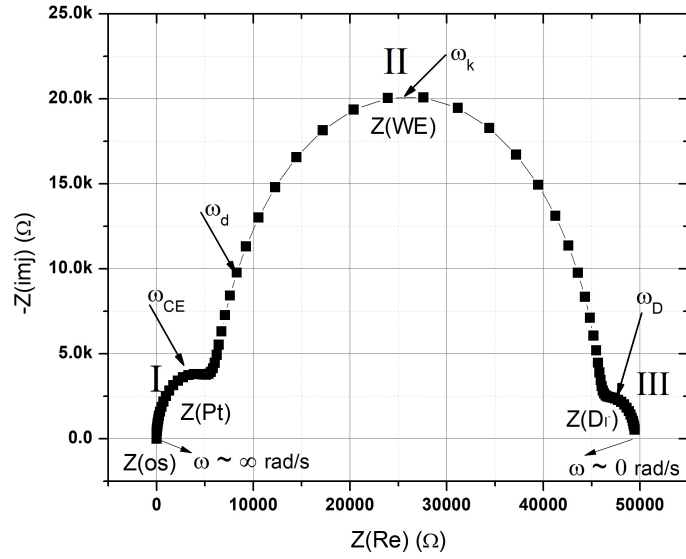
(a) Nyquist Plot of DSSC observed from EIS spectrum representing three semicircles (I-III)
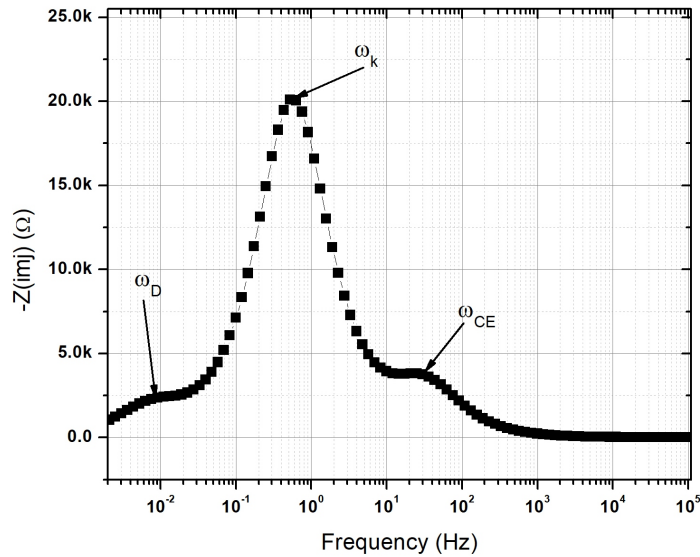
(b) Bode Plot of DSSC observed from EIS spectrum

Figure 5.2: Example of EIS pattern for DSSC

All characteristic frequencies except ω_d are shown in the Bode plot (Figure. 5.2(b)), ω_d. is appearing as a break point as high frequency limit of semicircle II of Nyquist plot (Figure. 5.2(a)) at certain steady-states but not in the Figure.5.2(b). The physical parameters representing the electron transport inside the DSSC can be determined by curve fitting of experimentally measured EIS spectra to an equivalent circuit comprises of resistances and capacitances [225]- [229]. The most preferable equivalent circuit of the complete DSSCs is a represented by transmission line model as shown in Figure 5.3, where r$_{ct}$ represents the CT resistance related to recombina-

tion at TiO_2/I_3^- interface; chemical capacitance of the TiO_2 film is given by c_u; r_t is representing electron transport (diffusion) resistance in TiO_2 film; Z_d corresponds to Warburg element showing the Nernst diffusion of I_3^- in electrolyte; R_{Pt} and C_{Pt} are the CT resistance and double-layer capacitance (DLC) at the Pt CE; R_{ct} and C_{TCO} are the CT resistance and the corresponding DLC at exposed TCO/electrolyte interface; R_{CO} and C_{CO} are the resistance and the capacitance at TCO/TiO_2 contact; Rs_{TCO} is the sheet resistance of FTO glass. It is considered as L is the thickness of the mesoscopic TiO_2 film [218].
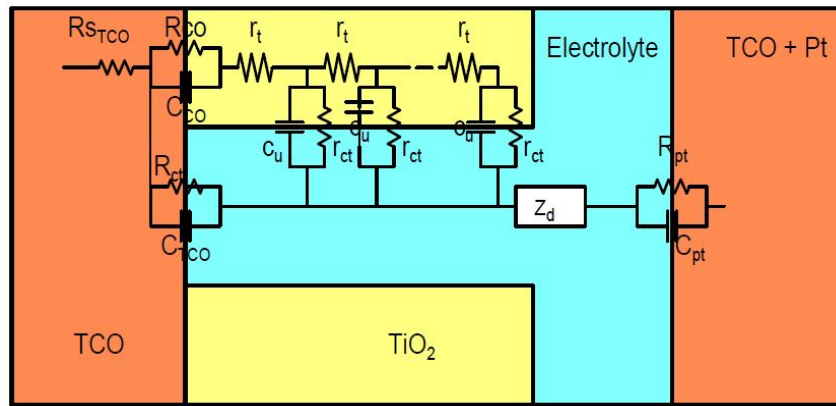

Figure 5.3: Transmission line model: Equivalent circuit representing complete DDSSC

The most significant processes are listed below with the equivalent impedance which is individually responsible for shaping the EIS of complete DSSCs.

5.3.1 Ohmic Series Resistance

For DSSSC, sheet resistance of electrode substrate (TCO glass) and the resistance of the electrolyte solution may be considered as a major contributor to the ohmic series resistance (R_{OS}) in DSSCs. For (R_{OS}), the impedance (Z_{OS}) is given by eqn. (5.9).

$$Z_{OS} = R_{OS} \tag{5.9}$$

5.3.2 Charge transfer (CT) at the CE

R_{Pt} at electrolyte/CE interface (see Figure. 5.3) is related to the redox reaction involving I^- and I_3^- in order to proceed the reaction; $e(Pt) + 1/2.I_3^- = 3/2.I^-$.

R_{Pt} is expressed by Buttler-Volmer equation with exchange current density (j_0) and given by eqn. (5.10) [234].

$$R_{Pt} = \frac{RT}{mFj_0} \tag{5.10}$$

where R (8.31 $Jmol^{-1}K^{-1}$) is the ideal gas constant, F (96485.33 $Cmol^{-1}$) is Faraday constant, T is the temperature (K), and m is number of electrons participated in the reaction. CT process at the counter electrode (CE) can be modeled by considering a parallel R-C circuit (see Figure. 5.3) with the equivalent impedance (Z_{Pt}) which can be expressed by given eqn. (5.11).

$$Z_{Pt} = \frac{R_{Pt}}{1 + j^{n_{CE}} R_{Pt} Q_{Pt}} \tag{5.11}$$

Therefore, ω_{CE} can be determined by eqn. (5.12) and Q_{Pt}, equivalent capacitance (C_{Pt}) can be determined by eqn. (5.13).

$$\omega_{CE} = \frac{1}{R_{Pt} Q_{Pt}^{1/n_{Pt}}} \tag{5.12}$$

$$C_{Pt} = Q_{Pt}^{1/n_{Pt}} R_{Pt}^{1/n_{Pt}-1} \tag{5.13}$$

5.3.3 Electron Diffusion and Recombination at the WE

In DSSCs, electron transport in the TiO_2 is coupled with electron loss mechinism at the TiO_2/electrolyte interface, typically referred as a recombination. Several study groups have thoroughly researched the diffusion and recombination impedances experienced by electrons at the WE of DSSCs [224], [226], [230]- [231]. The equivalent impedances for diffusion and recombination process as given by Z_{WE} (see eqn.(5.16)) which is significantly appears in the semicircle II of EIS spectra of DSSC as shown in Figure. 5.2(a). The characteristic frequencies, ω_k and ω_d are clearly depicted in Figure. 5.2(a)) and given by eqn. (5.14-5.15). In practice, CPE is also considered as a distributed capacitance in order to account the non ideality present in the diffusion-recombination processes in DSSC. For this case, ω_d for Z_{WE} can be also given by eqn.(5.14) [232]- [233].

$$\omega_k = \frac{1}{R_k Q_k^{1/n_k}} \tag{5.14}$$

Similarly, ω_d can be written as eqn. (5.15) [232]- [233]

$$\omega_d = \frac{1}{R_d Q_k^{1/n_k}} \tag{5.15}$$

$$Z_{WE} = \sqrt{\frac{R_d R_k}{1 + (j\omega/\omega_k)^{n_k}}} Coth \sqrt{\left(\frac{\omega_k}{\omega_d}\right) \left\{1 + \left(\frac{j\omega}{\omega_d}\right)^{n_k}\right\}} \tag{5.16}$$

where R_d is the electron transport or diffusion resistance, R_k is the electron transfer resistance related to e/ I_3^- recombination, and Q_k and n_k are the CPE (constant phase element,) prefactor and index, respectively. Additionally, C_u is termed as chemical capacitance formed across the TiO_2 film permeated with electrolytes and given by eqn. (5.17).

$$C_u = Q_k^{1/n_k} R_k^{1/n_k - 1} \tag{5.17}$$

5.3.4 Diffusion of I_3^- in the Electrolyte Solution

The solution of redox couple is maintained such that, the $[I^-] \gg [I_3^-]$, so it can be assumed that, mainly I_3^- contributes to the diffusion impedance (in electrolyte solution) that appearing at near $\omega \sim 0$ rad/s region (see Figure. 5.6). The diffusion impedance of I_3^- ions is modeled by transmission line of finite-length (FL) with short-circuits terminus and the corresponding FL Warburg impedance (Z_{DI}) [225]-[227] is given by eqn. (5.18).

$$Z_{D_I} = R_{D_I} \sqrt{\frac{D_I/\delta^2}{j\omega}} tanh \sqrt{\frac{j\omega}{D_I/\delta^2}} \tag{5.18}$$

where Z_{DI} is the diffusion impedance experienced by I_3^-, D_I is the diffusion coefficient of I_3^-, and δ representing diffusion length of I_3^- in electrolyte solution, which is considered as half of electrolyte spacer [226]. Eqn. (5.18) is also illustrating an impedance of FL diffusion with absorbing boundary condition provided that $\omega_D = D_I/\delta^2$. The frequency maxima ($\omega_{max} \sim$ peak frequency) are related to ω_D as $\omega_{max} = 2.5\omega_D$.

5.3.5   Representation of EIS Spectra of Complete DSSCs

According to Figure. 5.2(a) and Figure. 5.2(b), the impedances Z_{OS}, Z_{WE},Z_{DI},
and Z_{Pt} are capable to define a complete equivalent electrical circuit representing
DSSCs [218]- [227]. Thus, net impedance across the anode and cathode of the DSSC.
(Z_{DSSC}) can be expressed as by summation of eqn. (5.9), (5.11), (5.16), and (5.18)
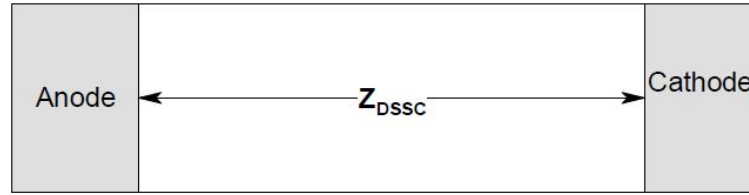and given by eqn. (5.19) and shown in Figure. 5.4.

Figure 5.4: Schematic representing Net impedance Z_{DSSC} across anode and cathode

$$Z_{DSSC} = Z_{OS} + Z_{Pt} + Z_{WE} + Z_{D_I} \tag{5.19}$$

5.4   Results and Discussion

Along with PV curves of the DSSCs, the power generated curves are also mentioned
in Figure. 5.5(a)-Figure. 5.5(c). It can be clearly depicted that the maximum
power (P_{max}) generated by the DSSCs upon light illumination increases from 3.35
mW→5.46 mW for L = 3 μm →12 μm (see Figure. 5.5(b)). As the L increases (3
μm →12 μm), the dye loading also enhances which further enhances the dye ab-
sorbance, hence increases the light absorption. Assuming TiO$_2$ is not of absorbing
any light spectrum. Dye is the only photosensitive material responsible for absorb-
ing the photons. The light absorbing capability of dye coated WE directly related
to its L is given by eqn. (5.20), where A is absorbance of dye, C is dye concentration
(M), ε is molar extinction coefficient of dye (M^{-1}cm^{-1}).

$$A = C\varepsilon L \tag{5.20}$$

Surface area of the TiO$_2$ film increases with electrode thickness L of WE results
more anchoring sites for N719 dye molecules to get adsorbed. As clearly seen from

eqn. (5.20) absorbance increases with L hence it increases the number of photons absorbed by photosensitive dye which further increases charge generations to enhance I_{SC} (see Figure. 5.5(c)).Increasing the L, improves the η of DSSCs from 3.55 % $\rightarrow$ 5.45 %, FF do not show significant variations and V_{OC} reduces from 0.825 V $\rightarrow$ 0.79 V (see Figure. 5.5(c)). The overall improvement in the η of the cell is mainly driven by the number of photons absorbed by the WE. In addition to analysis of light absorbing capability of WE, it is also required to investigate the CT and transport properties of DSSCs with various electrode thicknesses (L).

(a) I-V characteristics of DSSCs

(b) Power characteristics of DSSCs
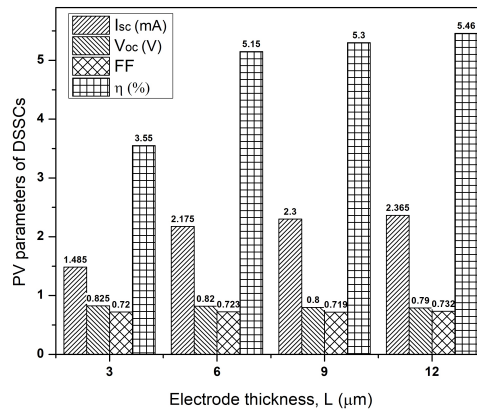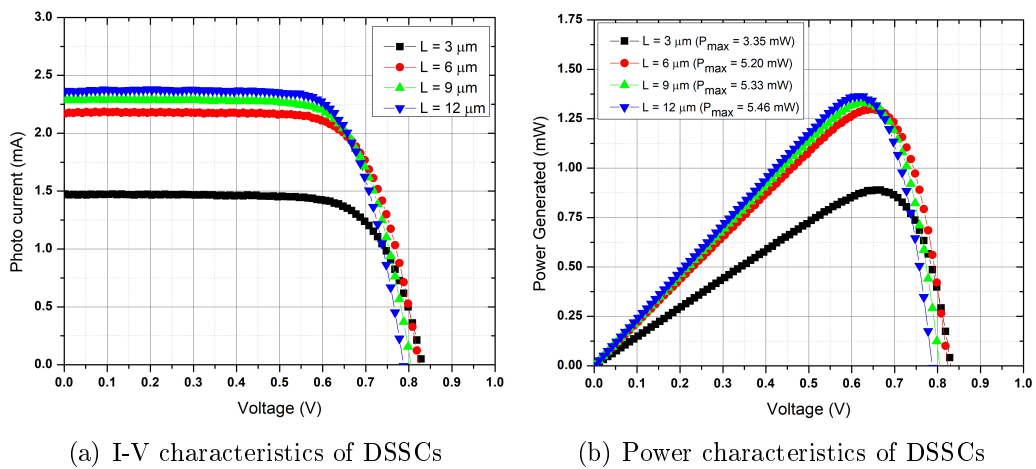
(c) PV parameters of fabricated DSSCs of L
= 3 μm $\rightarrow$12 μm

Figure 5.5: PV curves and performance of the DSSCs

The EIS characteristics for the fabricated DSSC (L = 3 μm $\rightarrow$12 μm) are measured and shown in Figure.5.6 representing Nyquist plot and it is clearly observed that measured bode plot from EIS spectra have three semicircles for every DSSC fabricated for L = 3 μm $\rightarrow$12 μm. Measured semicircles in the EIS spectrum were allocated to the corresponding processes of CT taking place in the DSSC.

As traversing from $\omega \sim \infty$ rad/s $\rightarrow 0$ rad/s (see Figure. 5.6) Z_{Pt} is describing the
first (I) semicircle which is representing CT processes at the P-E interfaces with
ω_{CE}, Z_{WE} is describing the second (II) is representing to the electron diffusion in
the TiO$_2$ film coupled with electron back reaction with I$_3^-$ at the T E interface,
and Z_{DI} describing third (III) semicircle ($\sim\omega_D$) at near of $\omega \sim 0$ rad/s region cor-
responds to the diffusion of I$_3^-$. It is also observed that the real part of impedance
of DSSC (Z_{Re}) at $\omega = 0$ rad/s is also shifting towards the lower values of Z_{Re} for
increasing L (3 μm $\rightarrow$12 μm) and it can be illustrated that series dc ohmic resistance
is also decreasing on increasing L. It can be easily depicted from the Figure. 5.6
that the height and width of the second semicircle defined for Z_{WE} is also decreases
for increasing L (3 μm $\rightarrow$12 μm). Additionally the peak of Z_{Im} is shifting towards
the low frequencies (see Figure. 5.6, Figure. 5.10). The eqn. (5.16) can be rear-
ranged for assumption $n_k = 1$, $\omega \ll \omega_d$ rad/s and given by eqn. (5.21) and further
separately expressed for high frequencies ($\omega \gg \omega_k$ rad/s) and low frequency ($\omega \ll \omega_k$
rad/s) regions and given by eqn. (5.22) and eqn.(5.23) respectively [221]- [223] and
difference between eqn.(5.23) and eqn. (5.22) relates the width ($\sim$R$_k$) of the second
semicircle defined by (Z_{WE}).

$$Z_{WE} = \frac{R_d}{3} + \frac{R_k}{1 + \dfrac{j\omega}{\omega_k}} \tag{5.21}$$

$$Z_{WE}(\omega \sim \infty rad/s) = \frac{R_d}{3} \tag{5.22}$$

$$Z_{WE}(\omega \sim 0 rad/s) = \frac{R_d}{3} + R_k \tag{5.23}$$

From the above equation it can be illustrated that width of the second semicircle rep-
resents the resistance R$_k$ as CT resistance related to electron recombination with I$_3^-$
ions at the T-E interface. Figure. 5.6 clearly depicts that R$_k$ is decreases for increas-
ing; hence CT resistance decreases for L (3 μm $\rightarrow$12 μm). Increasing L (3 μm $\rightarrow$12
μm) increases the dye loading capacity of the TiO$_2$ electrodes which further tends
to increase electron-hole pair generation upon light illumination hence increases
I$_{SC}$(mA) as shown in Figure. 5.5(c). Figure. 5.6 also illustrates that the impedance
point $Z_{WE}(\omega >> \omega_k) = R_d/3$ and impedance point $Z_{WE}(\omega << \omega_k) = R_d/3 + R_k$
which is shifting towards the lower values of Z_{Re} that clearly indicates that electron

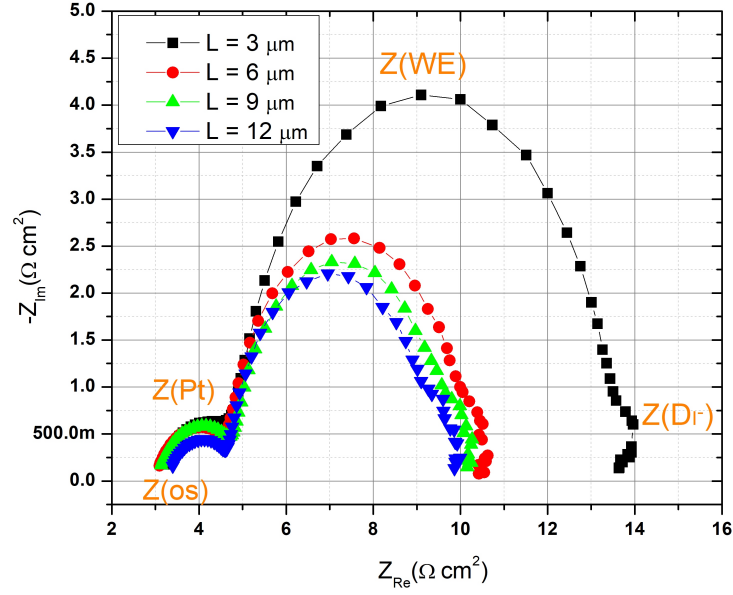diffusion resistance inside the TiO$_2$ film also varies for increasing L.

Figure 5.6: Nyquist Plots of fabricated DSSCs of L = 3 μm $\rightarrow$12 μm

To investigate and validate the charge transport properties in terms of parameters quoted in eqns. (5.9-5.18), it is required to fit the simulated EIS curves (Nyquist plot) based on theoretically modeled equations (eqn. 5.9, 5.11, 5.16, 5.18) with experimentally measured the EIS curves for fabricated DSSC of L (3 μm $\rightarrow$12 μm) in order to analyze impact of electrode thickness on charge transport properties of DSSC. Fitting of simulated EIS curves are done by EIS spectrum analyzer software by incorporating LevMarq and NM Simp algorithm. In this software, Z_{OS} is simply modeled as ohmic resistance R1, Z_{Pt} is representing a double layer capacitance at electrolyte/CE interface which is modeled as CPE. CPE resembles with the capacitance but impedance angle is not 90°, so the admittance of CPE is given by $Y_{CPE} = (j\omega)^{n_{CE}}Q_{Pt}$. The equivalent capacitance of CPE is given by $C_{Pt} = Q_{Pt}^{1/n_{Pt}}R_{Pt}^{1/n_{Pt}-1}$. Now Z_{Pt} is modeled as CPE in parallel with R2 = R_{Pt} in the software. The Z_{WE} is modeled as U (user defined) element (see eqn. 5.24) in the software by mentioning real and imaginary part and given by eqn.(5.25-5.26).

$$Z_{Uelement} = \frac{R_d}{3} + \frac{\omega_k^2 R_k}{\omega^2 + \omega_k^2} - j\frac{\omega\omega_k R_k}{\omega^2 + \omega_k^2} \tag{5.24}$$

$$Z_{Re} = \frac{R_d}{3} + \frac{\omega_k^2 R_k}{\omega^2 + \omega_k^2} \qquad (5.25)$$

$$Z_{Imj} = \frac{\omega \omega_k R_k}{\omega^2 + \omega_k^2} \qquad (5.26)$$

The impedance for I_3^- in the electrolyte solution (Z_{DI}) is modeled by equivalent impedance element (Z_{Ws1}) called Warburg short terminus given by eqn. (5.27), where W_{sr} $(\Omega cm^2\ s^{-0.5})$ and $W_{sc}(s^{-0.5})$ are known as the Warburg coefficients.

$$Z_{Ws1} = \frac{W_{sr}}{\sqrt{\omega}}(1-j)tanh\left(W_{sc}\sqrt{j\omega}\right) = W_{sr}W_{sc}\sqrt{2}\sqrt{\frac{1}{W_{sc}^2 j\omega}}tanh\left(\sqrt{W_{sc}^2 j\omega}\right) \quad (5.27)$$

Comparing eqn. (5.27) and eqn. ((5.18), it is observed that the diffusion resistance for I_3^- in the electrolyte solution, (R_{DI}) can be expressed in terms of Warburg coefficients and given by eqn. (5.28), where $W_{sc} = \delta/D_I^{0.5}$.

$$R_{D_I} = W_{sr}W_{sc}\sqrt{2} \qquad (5.28)$$

The Figure. 5.7 shows the equivalent circuit representing the various impedances inside the DSSC and employed for fitting experimentally measured EIS curves for L $(3\ \mu m \rightarrow 12\ \mu m)$. to obtain the charge transport properties illustrating the kinetics involved in the solar cell.
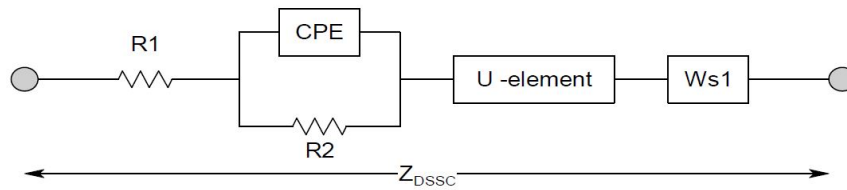

Figure 5.7: Equivalent model of DSSC representing electrochemical impedances responsible for charge transport properties involved in CT kinetics

Figure 5.8 and Table. 5.1 shows the simulation window of EIS spectrum analyzer and upper limits and lower limits for the fitting parameters which are representing charge transport parameters, where $R1(\Omega cm^2) = R_{OS}$, $R2(\Omega cm^2) = R_{Pt}$, $P1(\mu Fcm^2) = Q_{Pt}$, $n1 = n_{Pt}$, $UP1(\Omega cm^2) = R_d$, $UP2(\Omega cm^2) = R_k$, and $UP3(rad/s) = \omega_k$ respectively.
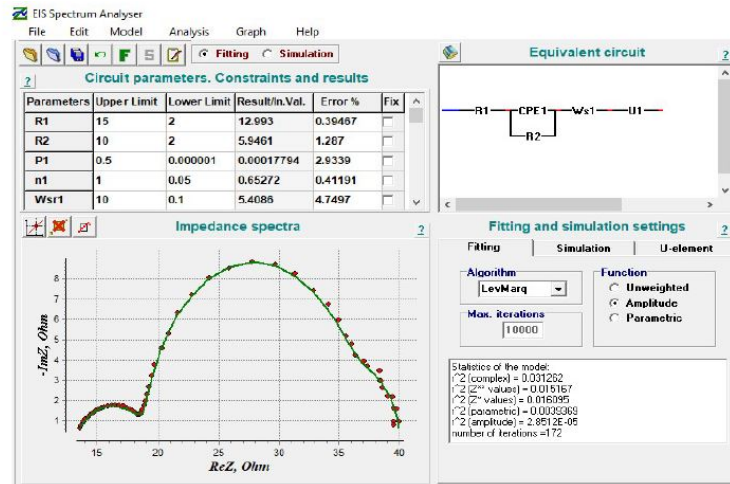
Figure 5.8: Shows the simulation window of EIS spectrum analyzer

On the basis of above description, the following fitted EIS curves are achieved as shown in Figure 5.9 for DSSC fabricated for L = 3 μm $\rightarrow$12 μm.
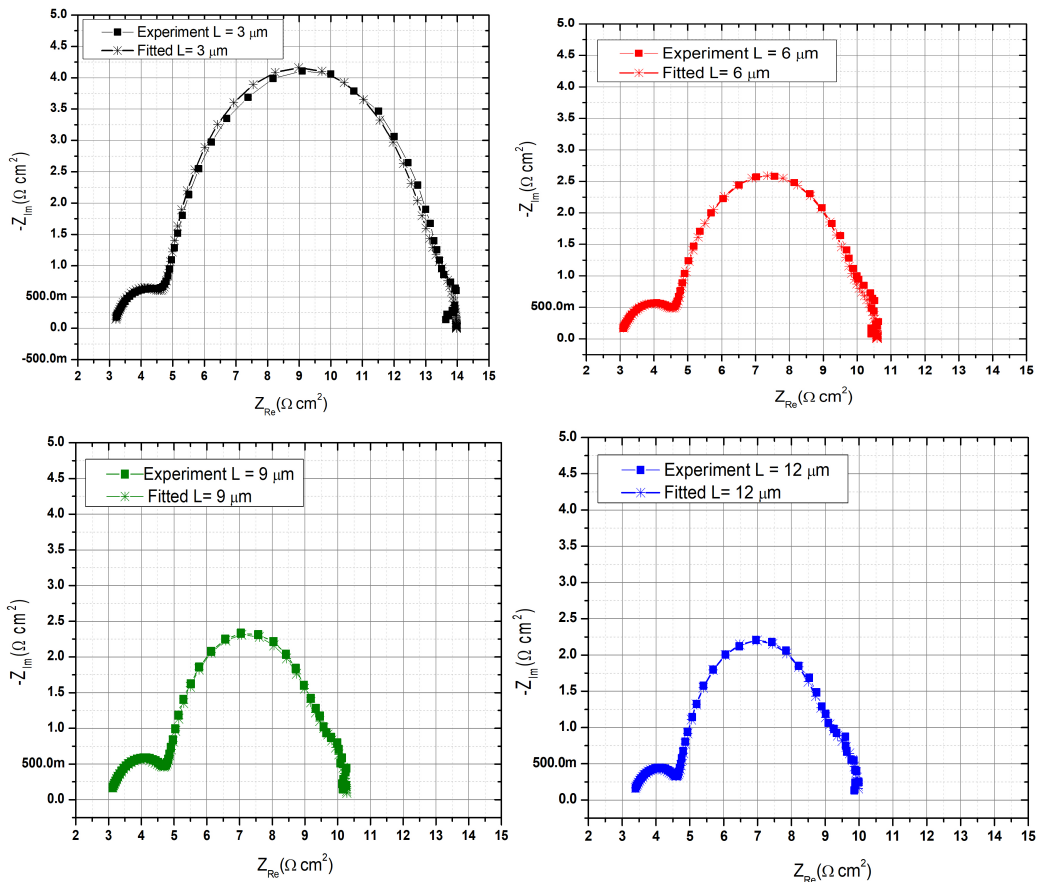

Figure 5.9: Fitted Nyquist plots (EIS curves) using EIS spectrum analyzer software for DSSC L = 3 μm $\rightarrow$ 12 μm.

Table 5.1: Limits for parameters of equivalent circuit (EIS) model)

Limits	R1	R2	P1	n1	W_{sr1}	W_{sc1}	UP1	UP2	UP3
Upper	15	10	0.5	1	10	0.2	10	100	150
Lower	2	2	$1\text{x}10^{-5}$	0.05	0.1	0.05	0.005	1	1

Table 5.2: Fitted parameters (eqn. 5.9-5.28) achieved from EIS spectrum analyzer
for DSSCs L = 3 μm $\to$ 12 μm

L(μm)	R1	R2	P1	n1	W_{sr1}	W_{sc1}	UP1	UP2	UP3
3	3.125	1.73	15.3	0.757	1.625	0.48	0.01	8	175.64
6	3.2	1.82	38.3	0.67	1.06	0.59	0.18	4.9	110.25
9	2.92	1.89	37.5	0.67	1.49	0.53	0.275	4.25	95.61
12	3.0	1.48	43.3	0.65	1.36	0.62	0.564	4.05	80.67

Simulations are carried out to achieve Nyquist Plots (see Figure 5.8) of an equivalent circuit (see Figure. 5.7) representing electrochemical impedances occurring inside DDSCs. Table 5.2 listed the fitted parameters for EIS spectrum analyzer for DSSCs achieved by fitting of simulated Nyquist plots with experimentally measured Nyquist Plots (EIS curves) for DSSC DSSC for L = 3 μm $\to$12 μm. On the basis of listed parameters in Table 5.2, Table 5.3 listed the charge transport properties computed from eqn. eqn. 5.9-5.28.

Table 5.3: Charge transport properties (eqn. 5.9-5.28) of DSSC (L = 3 μm $\to$ 12 μm) achieved by fitting of measured EIS curves by EIS spectrum analyze for DSSC

L(μm)	R_{OS}	R_{Pt}	Q_{Pt}	n1	R_{DI}	R_d	R_k	f_k
3	3.125	1.73	15.3	0.757	1.11	0.01	8	27.45
6	3.2	1.82	38.3	0.67	0.88	0.18	4.9	17.54
9	2.92	1.89	37.5	0.67	1.16	0.275	4.25	15.21
12	3.0	1.48	43.3	0.65	1.19	0.564	4.05	12.83

From Table 5.3 and Figure. 5.6, it can be illustrating a consistency between the width of the Nyquist plots (L = 3 μm $\to$12 μm) and the electron transport resistance, R_k. Squeezing of the width of the Nyquist plots is clearly interprets the decrease in R_k from 8 Ωcm^2 $\to$ 4.05 Ωcm^2 for L = 3 μm $\to$12 μm respectively. For spacer of 60 μm, the computed values of diffusion constant (D_I) for $I_3{}^-$ electrolyte by relation, $W_{sc} = \delta/D_I^{0.5}$ are 1.56x10^{-4}cm^{2}s^{-1}, 1.04x10^{-4}cm^{2}s^{-1}, 1.28x10^{-4}cm^{2}s^{-1}

and 0.95 x10^{-4}cm^{2}s^{-1} for L = 3 μm, 6 μm, 9 μm and 18 μm respectively. In addition to D$_I$, the CT resistance (R$_{Pt}$) across P-E interface does not show significant variation for L.

Characteristic frequency f$_k$ also shifted towards low frequencies for increasing L (see Table 5.3) and improves the electron life time (τ_e) in the TiO$_2$ electrode (see Table 5.4). The net series ohmic resistance (R$_S$) of the DSSC can be also expressed in terms of charge transport parameters observed from EIS curve fitting and given by eqn. (5.29) and listed in Table 5.4. It is observed that the R$_s$ (see eqn. 5.29) of the DSSC is also decreases with L such that highest value of R$_S$ (14.5 Ωcm^2) is noticed for L = 3 μm and insignificant variations for remaining L. It can be easily interpreted as R$_k$ at T-E interface reduces for increasing the L.

$$R_S = R_{OS} + R_{Pt} + R_{D_I} + R_k + \frac{R_d}{3} \tag{5.29}$$

Table 5.4: Series resistance (R$_S$), electron life time (τ_e) and characteristic frequency (f$_k$) estimation through EIS curve fitting method for DSSC L = 3 μm $\rightarrow$ 12 μm

Parameters	L = 3 μm	L = 6 μm	L = 9 μm	L = 12 μm
R$_s$(Ωcm^2)	14.5	11.04	11.62	10.06
τ_e(ms)	5.8	9.07	10.4	12.4
f$_k$	27.45	17.54	15.21	12.83
ω_d(x10^{-4})	21.9	0.477	0.235	0.092
L$_n$(μm)	2400	163	139	86

From the Figure. 5.10 It is clearly depicted that the peak of the imaginary impedance (Z$_{imj}$) shifting towards the lower frequencies for increasing the electrode thicknesses (L = 3 μm $\rightarrow$ 12 μm) i.e. characteristic frequency f$_k$ decreases from 27.45 Hz $\rightarrow$ 12.83 Hz for increasing L = 3 μm $\rightarrow$ 12 μm. Additionally is also noticed that peak of the imaginary impedance (-Z$_{imj}$) also decreases from 4.1 Ωcm^2 $\rightarrow$ 2.23 Ωcm^2 for increasing the electrode thicknesses (L = 3 μm $\rightarrow$ 12 μm) respectively. The electron life time is given by $\tau_e(1/2\pi$f$_k$); calculated as 5.7 ms, 9.07 ms, 10.4 ms, 12.4 ms for DSSC fabricated for L = 3 μm, 6 μm, 9 μm and 12 μm respectively. It is clearly investigated that electron life time get improved for increasing L (3 μm $\rightarrow$ 12 μm). Improvement in electron life time can be also considered as another factor for increases in I$_{SC}$ and overall η of the DSSC. Moreover it is clearly observed that for

each L as listed in Table. 5.3, the relation $R_k \gg R_d$ validates the presence of strong diffusion of electrons in TiO_2 electrode which can be illustrated as high conductivity of the electrode.
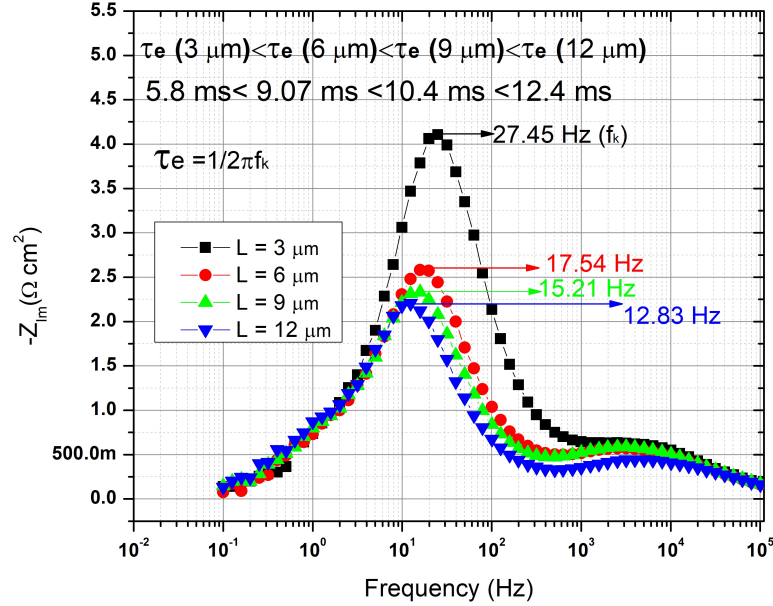

Figure 5.10: Plots of DSSC, L = 3 μm →12 μm representing the characteristic frequency f_k and τ_e.

In addition to $R_k \gg R_d$, the consistency with $\omega_d \gg \omega_k$ is also reported (see Table. 5.4 and Table. 5.4) as given by eqn. (5.30). Despite of existing finite R_k in DSSC causing recombination at T-E interface, the lower electron diffusion resistance (R_d) in TiO_2 WE is continuously transporting the injected electrons efficiently at the front TCO glass substrate. It can be easily understood that diffusion and recombination processes occurs simultaneously at WE however the relation $R_k / R_d \gg 1$(see Table 5.3) is seems to be existed for L = 3 μm → 12 μm to maintain the electron transport effectively through diffusion process. The computed values of effective diffusion length (L_n) of the electrons is listed in Table 5.4 given by eqn.(5.31) are much higher than each electrode thickness (L).

$$\frac{R_k}{R_d} = \frac{\omega_d}{\omega_k} \tag{5.30}$$

$$L_n = L\frac{R_k}{R_d} \tag{5.31}$$

The maximum V_{OC} that can be achieved is given by eqn. (5.32), where E_F is defined as fermi level of TiO_2 semiconductor and E_{redox} is defined as redox potential of the redox couple which depends on the electrolyte concentration resulting impact on V_{OC} (see eqn. 5.33).

$$V_{OC} = E_F + E_{redox} \qquad (5.32)$$

$$E_{redox} = E_o + \frac{RT}{nF} ln \frac{[I_3^-]}{[I^-]^3} \qquad (5.33)$$

Figure. 5.5(c) clearly depicts that V_{OC} is decreases from 0.825 V $\rightarrow$ 0.79 V for L = 3 μm $\rightarrow$ 12 μm. Here E_{redox} remains fixed due to fix I_3^-/I^- concentration, so shifting E_F downwards resulting lowering of V_{OC} (see eqn. 5.32). Moreover the energy difference between LUMO and HOMO levels of dye is also remain constant, hence it can be illustrated that lowering of E_F resulting efficient electron injection (Dye$\rightarrow TiO_2$). The improved life time can be attributed to reduced recombination of photo-generated electrons between the T-E interface.

The recombination depends on the loss mechanisms at the electrolyte/TiO_2 interface. The principal losses occur when an electron from the CB of TiO_2 recombines with the triiodide. Losing electron tends TiO_2 to p type semiconductor, shifts the EF downwards, and reduces open circuit voltage.

Chapter 6

Conclusion and Future Scope of the Work

6.1   Conclusion

Crystalline nanorice-like anatase TiO_2 powder can be well synthesized in a one-pot HT reaction simply by taking advantage of the electronegativity difference of the attached ligands. The average particle size and exposed BET surface area of the resulting nanorice-like TiO_2 powder are quite similar to those of a commercially available benchmark (reference) TiO_2 powder (Degussa P25). The reported HT synthesis process is very convenient, easy and readily scalable. Moreover the synthesized nanorice-like TiO_2 material showed good performance in a DSSC. Thus, such nanorice-like TiO_2 could be potentially adapted as a reference material in numerous applications, whenever and wherever possible.

Thickness of a working electrode (WE) affected the performance of its assembled DSSC structure. TCMM-simulation depicts that as thickness increase, short-circuit photocurrent density (J_{sc}) firstly increases ($\sim$ 5.95$\rightarrow$9.4 mAcm^{-2}) for electrode thickness from 3 μm to 12 μm, and achieve a maximum (9.4 mAcm^{-2}) at 12 μm and then decreases (9.4 mAcm^{-2} -8.72 mAcm^{-2}) for electrode thickness from 12 μm to 18 μm. The maximum Jsc (9.4 mAcm^{-2}) is obtained for a 12 μm thick WE. The similar trend is observed for maximum power points and DSSC efficiency. The optimum value of value of electrode thickness is found to be consistent with the experimental results and a single diode model as well (SDMM). In general, the

simulated TCMM results do not match well with the experimental observations, particularly a fill factor (error 15.8 %) and efficiency (error 14.02 %), and probably one of the possible major reasons is an unaccounted FTO resistance in simulation (tiberCAD) software. To account the FTO resistance, HDMM-simulation is carried out where the extracted value of R_s from experimental J-V curve is used along with other SDMM parameters extracted from TCMM (as input). The obtained simulated DSSC results are in close agreement with the experimental results with the tolerable permissible error for FF~0.52 % and for η~0.055 %.

Henceforth, clever, feasible and well understandable modelling-simulation study just requiring initial experimental data of a preassembled DSSC device could become highly economical and beneficial to make an optimized DSSC through only and only one more additional post assembling process. It have been recently proved that the performance of the dye solar cell can be improved by developing new semiconductor absorber, counter electrodes and electro-hole transporter layers which should offer new opportunities in light harvesting areas. Photoelectrode is the critical component which determines the light harvesting capability of DSSC device. Hence by finding the high yielding routes for synthesis of various morphologies for TiO_2 nanoparticles such as nano rods and rice like structures with suitable band gap and, the efficiency of DSSC device will be able to match with the efficiency of other type of solid state devices.

Thickness of a working electrode (WE) affected the performance of its assembled DSSC structure. Surface area of the TiO_2 film increases with electrode thickness L of WE results more anchoring sites for N719 dye molecules to get adsorbed. Therefore more photons get absorbed by the DSSCs leads to more charge generation upon light illumination and may lead to enhance the η of DSSC. However the analysis of diffusion process and recombination kinetics of charge carriers is also further required for investigation of charge transport properties affecting the performance of the cell. Simulating and fitting of EIS curves achieved from theoretical modeled equations using EIS spectrum analyzer software can be considered as a promising approach for parameters extraction for realization of charge transport properties of the DSSCs. The findings of improved life time (τ_e) of electrons is attributed to reduced recombination rate (ω_k, 175.64 rads^{-1} → 80.67 rads^{-1}) of photo-generated

electrons across the TiO$_2$/electrolyte interface hence increases the CT. More over
EIS fitted results also investigated that effective electron diffusion length L_n (2400
μm $\to$ 86 μm) in WE is much greater than electrode thickness L (3 μm $\to$ 12 μm)
which further satisfies $R_k \gg R_d$ required in order to maintain strong diffusion inside
the WE. The combined effect of improved dye loading and τ_e (5.8 ms $\to$ 12.4 ms)
are considered as responsible factors to increase the η of the DSSC from 3.55 % $\to$
5.46 % for L = 3 μm $\to$ 12 μm respectively From the results, scaling of the WE can
be considered as an critical component for light harvesting in DSSC system which
further improves the η.

Variations in TiO$_2$ micro/nano structure shape, size and crystal phase have the
potential to improve the DSSC's performance by improving dye loading and better
light scattering, or faster electron transportation and longer electron lifetime. DSSC
can be viewed as important factors, which have considerable potential to optimize
its performance by controlling electrode (WE) thickening, slurry or paste prepara-
tion and composition, particle form, size, porosity and its distribution in the oxide
layer. The EIS curved fitting technique for the evaluation of electron kinetics and
their lifetime over TiO$_2$/interface electrolyte's is a cost-effective tool to examine the
charge transport properties. The discussed modifications can be considered in order
to modulate the physical and chemical properties of WE to enhance PV performance
of DSSC.

6.2 Future Scope

Inspite of achieving great development in photovoltaic performance (PV) (η), DSSCs
are still under research to match the efficiency with those of conventional Si-based
solar cells. However DSSC has attracted significant attention of both scientists and
market globe wide for last few decades. The cost effective fabrication process of
DSSCs make them viable and efficient solar cells. It is observed that low cost to
commercialize DSSCs along with better improved PV performance may replace con-
ventional solar cells near future. Various research groups are continuously perform-
ing experiments for improving the efficiency and viability of the cell. A widespread
study has already started to achieve significant gain in the efficiency. These include

the use of efficient photo sensitizers to inject the photo generated charge carries into the working electrode, solid state electrolytes for better temperature response, synthesis routes to transform morphology and crystalline property of electrode etc. The DSSC can produce electricity under low light conditions, including indoor lighting. Due to the structural design and different color dyes, the cell features colors and transparency. Therefore, DSSCs can be used on architecture, interior applications, electronic devices, and portable power systems.

Bibliography

[1] https://www.eia.gov/todayinenergy/detail.php?id=41433

[2] https://www.e-education.psu.edu/meteo300/node/686

[3] https://www.nrel.gov/grid/solar-resource/spectra-am1.5.html

[4] Ranabhat K, Patrikeev L, Antal'evna-Revina A, Andrianov K, Lapshinsky V, Sofronova E. An introduction to solar cell technology. Journal of Applied Engineering Science. 2016; 14(4):481-491.

[5] Wang A, Zhao J, Green MA. 24% efficient silicon solar cells. Applied physics letters. 1990 Aug 6;57(6):602-4.

[6] Green MA, Hishikawa Y, Dunlop ED, Levi DH, Hohl-Ebinger J, Ho-Baillie AW. Solar cell efficiency tables (version 52). Progress in Photovoltaics: Research and Applications. 2018 Jul;26(7):427-36.)

[7] Britt J, Ferekides C. Thin-film CdS/CdTe solar cell with 15.8% efficiency. Applied physics letters. 1993 May 31;62(22):2851-2.

[8] Cotal H, Fetzer C, Boisvert J, Kinsey G, King R, Hebert P, Yoon H, Karam N. III–V multijunction solar cells for concentrating photovoltaics. Energy and Environmental Science. 2009;2(2):174-92.

[9] O'regan B, Grätzel M. A low-cost, high-efficiency solar cell based on dye-sensitized colloidal TiO_2 films. nature. 1991 Oct;353(6346):737-40.

[10] Kay A, Grätzel M. Low cost photovoltaic modules based on dye sensitized nanocrystalline titanium dioxide and carbon powder. Solar Energy Materials and Solar Cells. 1996 Oct 30;44(1):99-117.

[11] Smestad G, Bignozzi C, Argazzi R. Testing of dye sensitized TiO_2 solar cells I: Experimental photocurrent output and conversion efficiencies. Solar energy materials and solar cells. 1994 Mar 1;32(3):259-72.

[12] Gong J, Sumathy K, Zhou Z, Qiao Q. Modeling of interfacial and bulk charge transfer in dye-sensitized solar cells. Cogent Engineering. 2017 Jan 1;4(1):1287231.

[13] Nazeeruddin MK, Pechy P, Renouard T, Zakeeruddin SM, Humphry-Baker R, Comte P, Liska P, Cevey L, Costa E, Shklover V, Spiccia L. Engineering of efficient panchromatic sensitizers for nanocrystalline TiO2-based solar cells. Journal of the American Chemical Society. 2001 Feb 28;123(8):1613-24.

[14] Natural dyes as photosensitizers for dye-sensitized solar cell

[15] Adeloye AO, Ajibade PA. A high molar extinction coefficient mono-anthracenyl bipyridyl heteroleptic ruthenium (II) complex: Synthesis, photophysical and electrochemical properties. Molecules. 2011 Jun;16(6):4615-31.

[16] Nazeeruddin MK, Pechy P, Grätzel M. Efficient panchromatic sensitization of nanocrystallineTiO2 films by a black dye based on atrithiocyanato–ruthenium complex. Chemical Communications. 1997 Jan 1(18):1705-6.

[17] Gupta KS, Zhang J, Marotta G, Reddy MA, Singh SP, Islam A, Han L, De Angelis F, Chandrasekharam M, Pastore M. Effect of the anchoring group in the performance of carbazole-phenothiazine dyads for dye-sensitized solar cells. Dyes and Pigments. 2015 Feb 1;113:536-45.

[18] Peng Y, Geedipally SR, Lord D. Effect of roadside features on single-vehicle roadway departure crashes on rural two-lane roads. Transportation research record. 2012 Jan;2309(1):21-9.

[19] Monari A, Assfeld X, Beley M, Gros PC. Theoretical study of new ruthenium-based dyes for dye-sensitized solar cells. The Journal of Physical Chemistry A. 2011 Apr 21;115(15):3596-603.

[20] Yen YS, Chen YC, Hsu YC, Chou HH, Lin JT, Yin DJ. Heteroleptic Ruthenium Sensitizers That Contain an Ancillary Bipyridine Ligand Tethered with Hydrocarbon Chains for Efficient Dye-Sensitized Solar Cells. Chemistry–A European Journal. 2011 Jun 6;17(24):6781-8.

[21] Funaki T, Kusama H, Onozawa-Komatsuzaki N, Kasuga K, Sayama K, Sugihara H. Near-IR Sensitization of Dye-Sensitized Solar Cells Using Thiocyanate-Free Cyclometalated Ruthenium (II) Complexes Having a Pyridylquinoline Ligand. European Journal of Inorganic Chemistry. 2014 Mar;2014(8):1303-11.

[22] Gao F, Wang Y, Shi D, Zhang J, Wang M, Jing X, Humphry-Baker R, Wang P, Zakeeruddin SM, Gratzel M. Enhance the optical absorptivity of nanocrystalline TiO2 film with high molar extinction coefficient ruthenium sensitizers for high performance dye sensitized solar cells. Journal of the American Chemical Society. 2008 Aug 13;130(32):10720-8.

[23] Nazeeruddin MK, De Angelis F, Fantacci S, Selloni A, Viscardi G, Liska P, Ito S, Takeru B, Grätzel M. Combined experimental and DFT-TDDFT computational study of photoelectrochemical cell ruthenium sensitizers. Journal of the American Chemical Society. 2005 Dec 7;127(48):16835-47.

[24] Cao Y, Bai Y, Yu Q, Cheng Y, Liu S, Shi D, Gao F, Wang P. Dye-sensitized solar cells with a high absorptivity ruthenium sensitizer featuring a 2-(hexylthio) thiophene conjugated bipyridine. The Journal of Physical Chemistry C. 2009 Apr 16;113(15):6290-7.

[25] Gao F, Wang Y, Zhang J, Shi D, Wang M, Humphry-Baker R, Wang P, Zakeeruddin SM, Grätzel M. A new heteroleptic ruthenium sensitizer enhances the absorptivity of mesoporous titania film for a high efficiency dye-sensitized solar cell. Chemical communications. 2008(23):2635-7.

[26] Al-Alwani MA, Mohamad AB, Ludin NA, Kadhum AA, Sopian K. Dye-sensitised solar cells: Development, structure, operation principles, electron kinetics, characterisation, synthesis materials and natural photosensitisers. Renewable and Sustainable Energy Reviews. 2016 Nov 1;65:183-213.

[27] Wang P, Zakeeruddin SM, Moser JE, Humphry-Baker R, Comte P, Aranyos V, Hagfeldt A, Nazeeruddin MK, Grätzel M. Stable new sensitizer with improved light harvesting for nanocrystalline dye-sensitized solar cells. Advanced Materials. 2004 Oct 18;16(20):1806-11.

[28] Adeloye AO, Ajibade PA. Towards the Development of Functionalized PolypyridineLigands for Ru (II) Complexes as Photosensitizers inDye-Sensitized Solar Cells (DSSCs). Molecules. 2014 Aug;19(8):12421-60.

[29] Abbotto A, Barolo C, Bellotto L, De Angelis F, Grätzel M, Manfredi N, Marinzi C, Fantacci S, Yum JH, Nazeeruddin MK. Electron-rich heteroaromatic conjugated bipyridine based ruthenium sensitizer for efficient dye-sensitized solar cells. Chemical communications. 2008(42):5318-20.

[30] Chen CY, Wu SJ, Li JY, Wu CG, Chen JG, Ho KC. A new route to enhance the light harvesting capability of ruthenium complexes for dye sensitized solar cells. Advanced materials. 2007 Nov 19;19(22):3888-91.

[31] Kuang D, Ito S, Wenger B, Klein C, Moser JE, Humphry-Baker R, Zakeeruddin SM, Grätzel M. High molar extinction coefficient heteroleptic ruthenium complexes for thin film dye-sensitized solar cells. Journal of the American Chemical Society. 2006 Mar 29;128(12):4146-54.

[32] Li JY, Chen CY, Chen JG, Tan CJ, Lee KM, Wu SJ, Tung YL, Tsai HH, Ho KC, Wu CG. Heteroleptic ruthenium antenna-dye for high-voltage dye-sensitized solar cells. Journal of Materials Chemistry. 2010;20(34):7158-64.

[33] Nazeeruddin MK, Wang Q, Cevey L, Aranyos V, Liska P, Figgemeier E, Klein C, Hirata N, Koops S, Haque SA, Durrant JR. DFT-INDO/S modeling of new high molar extinction coefficient charge-transfer sensitizers for solar cell applications. Inorganic Chemistry. 2006 Jan 23;45(2):787-97.

[34] Jiang KJ, Xia JB, Masaki N, Noda S, Yanagida S. Efficient sensitization of nanocrystalline TiO2 films with high molar extinction coefficient ruthenium complex. Inorganica Chimica Acta. 2008 Feb 15;361(3):783-5.

[35] Klein C, Nazeeruddin MK, Liska P, Di Censo D, Hirata N, Palomares E, Durrant JR, Grätzel M. Engineering of a novel ruthenium sensitizer and its application in dye-sensitized solar cells for conversion of sunlight into electricity. Inorganic Chemistry. 2005 Jan 24;44(2):178-80.

[36] Klein C, Nazeeruddin MK, Di Censo D, Liska P, Grätzel M. Amphiphilic ruthenium sensitizers and their applications in dye-sensitized solar cells. Inorganic Chemistry. 2004 Jul 12;43(14):4216-26.

[37] Wang P, Klein C, Moser JE, Humphry-Baker R, Cevey-Ha NL, Charvet R, Comte P, Zakeeruddin SM, Grätzel M. Amphiphilic ruthenium sensitizer with 4, 4 '-diphosphonic acid-2, 2 '-bipyridine as anchoring ligand for nanocrystalline dye sensitized solar cells. The Journal of Physical Chemistry B. 2004 Nov 11;108(45):17553-9.

[38] Chen CY, Wang M, Li JY, Pootrakulchote N, Alibabaei L, Ngocle CH, Decoppet JD, Tsai JH, Gratzel C, Wu CG, Zakeeruddin SM. Highly efficient light harvesting ruthenium sensitizer for thin film dye sensitized solar cells. ACS nano. 2009 Oct 27;3(10):3103-9.

[39] Toivola M, Ahlskog F, Lund P. Industrial sheet metals for nanocrystalline dye-sensitized solar cell structures. Solar energy materials and solar cells. 2006 Nov 6;90(17):2881-93.

[40] Hagberg DP, Edvinsson T, Marinado T, Boschloo G, Hagfeldt A, Sun L. A novel organic chromophore for dye-sensitized nanostructured solar cells. Chemical Communications. 2006(21):2245-7.

[41] Horiuchi T, Miura H, Uchida S. Highly-efficient metal-free organic dyes for dye-sensitized solar cells. Chemical Communications. 2003(24):3036-7.

[42] Iqbal Z, Wu WQ, Kuang DB, Wang L, Meier H, Cao D. Phenothiazine-based dyes with bilateral extension of π conjugation for efficient dye-sensitized solar cells. Dyes and Pigments. 2013 Mar 1;96(3):722-31.

[43] Ozawa H, Shimizu R, Arakawa H. Significant improvement in the conversion efficiency of black-dye-based dye-sensitized solar cells by cosensitization with organic dye. RSC advances. 2012;2(8):3198-200.

[44] Kishimoto S, Maoka T, Sumitomo K, Ohmiya A. Analysis of carotenoid composition in petals of calendula (Calendula officinalis L.). Bioscience, biotechnology, and biochemistry. 2005 Jan 1;69(11):2122-8.

[45] Chang H, Wu HM, Chen TL, Huang KD, Jwo CS, Lo YJ. Dye-sensitized solar cell using natural dyes extracted from spinach and ipomoea. Journal of Alloys and Compounds. 2010 Apr 16;495(2):606-10.

[46] Kamel MM, El-Shishtawy RM, Yussef BM, Mashaly H. Ultrasonic assisted dyeing: III. Dyeing of wool with lac as a natural dye. Dyes and pigments. 2005 May 1;65(2):103-10.

[47] Luo P, Niu H, Zheng G, Bai X, Zhang M, Wang W. From salmon pink to blue natural sensitizers for solar cells: Canna indica L., Salvia splendens, cowberry and Solanum nigrum L. Spectrochimica Acta Part A: Molecular and Biomolecular Spectroscopy. 2009 Nov 1;74(4):936-42.

[48] Sutthanut K, Sripanidkulchai B, Yenjai C, Jay M. Simultaneous identification and quantitation of 11 flavonoid constituents in Kaempferia parviflora by gas chromatography. Journal of Chromatography A. 2007 Mar 2;1143(1-2):227-33.

[49] Kumara GR, Kaneko S, Okuya M, Onwona-Agyeman B, Konno A, Tennakone K. Shiso leaf pigments for dye-sensitized solid-state solar cell. Solar Energy Materials and Solar Cells. 2006 May 23;90(9):1220-6.

[50] Zhou H, Wu L, Gao Y, Ma T. Dye-sensitized solar cells using 20 natural dyes as sensitizers. Journal of Photochemistry and Photobiology A: Chemistry. 2011 Apr 15;219(2-3):188-94.

[51] Wongcharee K, Meeyoo V, Chavadej S. Dye-sensitized solar cell using natural dyes extracted from rosella and blue pea flowers. Solar Energy Materials and Solar Cells. 2007 Apr 16;91(7):566-71.

[52] Hernandez-Martinez AR, Estevez M, Vargas S, Quintanilla F, Rodriguez R. New dye-sensitized solar cells obtained from extracted bracts of Bougainvillea glabra and spectabilis betalain pigments by different purification processes. International journal of molecular sciences. 2011 Sep;12(9):5565-76.

[53] Kumara NT, Ekanayake P, Lim A, Liew LY, Iskandar M, Ming LC, Senadeera GK. Layered co-sensitization for enhancement of conversion efficiency of natural dye sensitized solar cells. Journal of alloys and compounds. 2013 Dec 25;581:186-91.

[54] Ali MS, Lee JS, Lee YI. Identification of three-parameter models in the presence of non-zero initial condition. InICCAS 2010 2010 Oct 27 (pp. 5-8). IEEE.

[55] Calogero G, Di Marco G, Cazzanti S, Caramori S, Argazzi R, Di Carlo A, Bignozzi CA. Efficient dye-sensitized solar cells using red turnip and purple wild sicilian prickly pear fruits. International journal of molecular sciences. 2010 Jan;11(1):254-67.

[56] Shanmugam V, Manoharan S, Anandan S, Murugan R. Performance of dye-sensitized solar cells fabricated with extracts from fruits of ivy gourd and flowers of red frangipani as sensitizers. Spectrochimica Acta Part A: Molecular and Biomolecular Spectroscopy. 2013 Mar 1;104:35-40.

[57] Singh LK, Karlo T, Pandey A. Performance of fruit extract of Melastoma malabathricum L. as sensitizer in DSSCs. Spectrochimica Acta Part A: Molecular and Biomolecular Spectroscopy. 2014 Jan 24;118:938-43.

[58] Chang HM, Huang CK, Torng CC. Shop Floor Control Mechanism of Aerospace Machine Shop. InApplied Mechanics and Materials 2011 (Vol. 52, pp. 214-219). Trans Tech Publications Ltd.

[59] Lai WH, Su YH, Teoh LG, Hon MH. Commercial and natural dyes as photosensitizers for a water-based dye-sensitized solar cell loaded with gold nanoparticles. Journal of Photochemistry and Photobiology A: Chemistry. 2008 Apr 15;195(2-3):307-13.

[60] Grätzel M. Recent advances in sensitized mesoscopic solar cells. Accounts of chemical research. 2009 Nov 17;42(11):1788-98.

[61] Yu Z, Vlachopoulos N, Gorlov M, Kloo L. Liquid electrolytes for dye-sensitized solar cells. Dalton transactions. 2011;40(40):10289-303.

[62] Gorlov M, Kloo L. Ionic liquid electrolytes for dye-sensitized solar cells. Dalton Transactions. 2008(20):2655-66.

[63] Wu J, Lan Z, Hao S, Li P, Lin J, Huang M, Fang L, Huang Y. Progress on the electrolytes for dye-sensitized solar cells. Pure and Applied Chemistry. 2008 Jan 1;80(11):2241-58.

[64] de Freitas JN, Nogueira AF, De Paoli MA. New insights into dye-sensitized solar cells with polymer electrolytes. Journal of Materials Chemistry. 2009;19(30):5279-94.

[65] Zhang W, Cheng Y, Yin X, Liu B. Solid-state dye-sensitized solar cells with conjugated polymers as hole-transporting materials. Macromolecular Chemistry and Physics. 2011 Jan 4;212(1):15-23.

[66] Wang P, Wenger B, Humphry-Baker R, Moser JE, Teuscher J, Kantlehner W, Mezger J, Stoyanov EV, Zakeeruddin SM, Grätzel M. Charge separation and efficient light energy conversion in sensitized mesoscopic solar cells based on binary ionic liquids. Journal of the American Chemical Society. 2005 May 11;127(18):6850-6.

[67] Wang P, Zakeeruddin SM, Humphry-Baker R, Grätzel M. A binary ionic liquid electrolyte to achieve ≥ 7 % power conversion efficiencies in dye-sensitized solar cells. Chemistry of Materials. 2004 Jul 13;16(14):2694-6.

[68] Wang P, Zakeeruddin SM, Moser JE, Grätzel M. A new ionic liquid electrolyte enhances the conversion efficiency of dye-sensitized solar cells. The Journal of Physical Chemistry B. 2003 Dec 4;107(48):13280-5.

[69] Kuang D, Wang P, Ito S, Zakeeruddin SM, Grätzel M. Stable mesoscopic dye-sensitized solar cells based on tetracyanoborate ionic liquid electrolyte. Journal of the American Chemical Society. 2006 Jun 21;128(24):7732-3. 161

[70] Ito S, Zakeeruddin SM, Humphry-Baker R, Liska P, Charvet R, Comte P, Nazeeruddin MK, Péchy P, Takata M, Miura H, Uchida S. High-efficiency organic-dye-sensitized solar cells controlled by nanocrystalline-TiO2 electrode thickness. Advanced Materials. 2006 May 2;18(9):1202-5.

[71] Fabregat-Santiago F, Bisquert J, Palomares E, Otero L, Kuang D, Zakeeruddin SM, Grätzel M. Correlation between photovoltaic performance and impedance spectroscopy of dye-sensitized solar cells based on ionic liquids. The Journal of Physical Chemistry C. 2007 May 3;111(17):6550-60.

[72] Fan L, Kang S, Wu J, Hao S, Lan Z, Lin J. Quasi-solid state dye-sensitized solar cells based on polyvinylpyrrolidone with ionic liquid. Energy Sources, Part A: Recovery, Utilization, and Environmental Effects. 2010 Jun 23;32(16):1559-68.

[73] Sauvage F, Chhor S, Marchioro A, Moser JE, Graetzel M. Butyronitrile-based electrolyte for dye-sensitized solar cells. Journal of the American Chemical Society. 2011 Aug 24;133(33):13103-9.

[74] Shi D, Pootrakulchote N, Li R, Guo J, Wang Y, Zakeeruddin SM, Gratzel M, Wang P. New efficiency records for stable dye-sensitized solar cells with low volatility and ionic liquid electrolytes. The Journal of Physical Chemistry C. 2008 Nov 6;112(44):17046-50.

[75] Nogueira AF, Longo C, De Paoli MA. Polymers in dye sensitized solar cells: overview and perspectives. Coordination Chemistry Reviews. 2004 Jul 1;248(13-14):1455-68.

[76] Stathatos E, Lianos P, Zakeeruddin SM, Liska P, Gratzel M. A quasi solid state dye sensitized solar cell based on a sol gel nanocomposite electrolyte containing ionic liquid. Chemistry of materials. 2003 May 6;15(9):1825-9.

[77] Chen X, Zhao J, Zhang J, Qiu L, Xu D, Zhang H, Han X, Sun B, Fu G, Zhang Y, Yan F. Bis-imidazolium based poly (ionic liquid) electrolytes for quasi-solid-state dye-sensitized solar cells. Journal of Materials Chemistry. 2012;22(34):18018-24.

[78] Jeon N, Hwang DK, Kang YS, Im SS, Kim DW. Quasi-solid-state dye-sensitized solar cells assembled with polymeric ionic liquid and poly (3, 4-ethylenedioxythiophene) counter electrode. Electrochemistry communications. 2013 Sep 1;34:1-4.

[79] Rong Y, Li X, Liu G, Wang H, Ku Z, Xu M, Liu L, Hu M, Yang Y, Zhang M, Liu T. Monolithic quasi-solid-state dye-sensitized solar cells based on iodine-free polymer gel electrolyte. Journal of power sources. 2013 Aug 1;235:243-50.

[80] Huang X, Qin D, Zhang X, Luo Y, Huang S, Li D, Meng Q. The potential of eutectic mixtures as environmentally friendly, solvent-free electrolytes for dye-sensitized solar cells. RSC advances. 2013;3(19):6922-9.

[81] Liu X, Iocozzia J, Wang Y, Cui X, Chen Y, Zhao S, Li Z, Lin Z. Noble metal metal oxide nanohybrids with tailored nanostructures for efficient solar energy conversion, photocatalysis and environmental remediation. Energy and Environmental Science. 2017;10(2):402-34.

[82] Wang G, Wang L, Zhuo S, Fang S, Lin Y. An iodine-free electrolyte based on ionic liquid polymers for all-solid-state dye-sensitized solar cells. Chemical Communications. 2011;47(9):2700-2.

[83] Chi WS, Koh JK, Ahn SH, Shin JS, Ahn H, Ryu DY, Kim JH. Highly efficient I2-free solid-state dye-sensitized solar cells fabricated with polymerized ionic liquid and graft copolymer-directed mesoporous film. Electrochemistry communications. 2011 Dec 1;13(12):1349-52.

[84] Wright PV. Polymer electrolytes—the early days. Electrochimica Acta. 1998 Apr 30;43(10-11):1137-43.

[85] Di Noto V, Lavina S, Giffin GA, Negro E, Scrosati B. Polymer electrolytes: Present, past and future. 271

[86] Wang Y. Recent research progress on polymer electrolytes for dye-sensitized solar cells. Solar Energy Materials and Solar Cells. 2009 Aug 1;93(8):1167-75.

[87] Wang P, Zakeeruddin SM, Moser JE, Nazeeruddin MK, Sekiguchi T, Grätzel M. A stable quasi-solid-state dye-sensitized solar cell with an amphiphilic ruthenium sensitizer and polymer gel electrolyte. Nature materials. 2003 Jun;2(6):402-7.

[88] Song JY, Wang YY, Wan CC. Review of gel-type polymer electrolytes for lithium-ion batteries. Journal of power sources. 1999 Feb 1;77(2):183-97.

[89] Mohmeyer N, Wang P, Schmidt HW, Zakeeruddin SM, Grätzel M. Quasi-solid-state dye sensitized solar cells with 1, 3: 2, 4-di-O-benzylidene-D-sorbitol derivatives as low molecular weight organic gelators. Journal of Materials Chemistry. 2004;14(12):1905-9.

[90] Wu J, Lan Z, Wang D, Hao S, Lin J, Huang Y, Yin S, Sato T. Gel polymer electrolyte based on poly (acrylonitrile-co-styrene) and a novel organic iodide salt for quasi-solid state dye-sensitized solar cell. Electrochimica Acta. 2006 May 25;51(20):4243-9.

[91] Xia J, Li F, Huang C, Zhai J, Jiang L. Improved stability quasi-solid-state dye-sensitized solar cell based on polyether framework gel electrolytes. Solar energy materials and solar cells. 2006 May 5;90(7-8):944-52.

[92] Lu S, Koeppe R, Günes S, Sariciftci NS. Quasi-solid-state dye-sensitized solar cells with cyanoacrylate as electrolyte matrix. Solar energy materials and solar cells. 2007 Jul 23;91(12):1081-6.

[93] Gerbaldi C, Nair JR, Meligrana G, Bongiovanni R, Bodoardo S, Penazzi N. UV-curable siloxane-acrylate gel-copolymer electrolytes for lithium-based battery applications. Electrochimica Acta. 2010 Jan 25;55(4):1460-7.

[94] Zhou Y, Lin G, Shih AJ, Hu SJ. Assembly pressure and membrane swelling in PEM fuel cells. Journal of power sources. 2009 Jul 15;192(2):544-51.

[95] Zakeeruddin SM, Grätzel M. Solvent-free ionic liquid electrolytes for mesoscopic dye-sensitized solar cells. Advanced Functional Materials. 2009 Jul 24;19(14):2187-202.

[96] Saito Y, Azechi T, Kitamura T, Hasegawa Y, Wada Y, Yanagida S. Photosensitizing ruthenium complexes for solid state dye solar cells in combination with conducting polymers as hole conductors. Coordination chemistry reviews. 2004 Jul 1;248(13-14):1469-78.

[97] Lee B, He J, Chang RP, Kanatzidis MG. All solid state dye-sensitized solar cells with high efficiency. Nature. 2012 May;485(7399):486-9.

[98] Yu Z, Gorlov M, Nissfolk J, Boschloo G, Kloo L. Investigation of iodine concentration effects in electrolytes for dye-sensitized solar cells. The Journal of Physical Chemistry C. 2010 Jun 17;114(23):10612-20.

[99] Govindaraj R, Pandian MS, Ramasamy P, Mukhopadhyay S. Sol–gel synthesized mesoporous anatase titanium dioxide nanoparticles for dye sensitized solar cell (DSSC) applications. Bulletin of Materials Science. 2015 Apr 1;38(2):291-6.

[100] Li ZQ, Que YP, Mo LE, Chen WC, Ding Y, Ma YM, Jiang L, Hu LH, Dai SY. One pot synthesis of mesoporous TiO2 microspheres and its application for high efficiency dye sensitized solar cells. ACS applied materials and interfaces. 2015 May 27;7(20):10928-34.

[101] Wang HE, Zheng LX, Liu CP, Liu YK, Luan CY, Cheng H, Li YY, Martinu L, Zapien JA, Bello I. Rapid microwave synthesis of porous TiO2 spheres and their applications in dye-sensitized solar cells. The Journal of Physical Chemistry C. 2011 Jun 2;115(21):10419-25.

[102] Dhungel SK, Park JG. Optimization of paste formulation for TiO2 nanoparticles with wide range of size distribution for its application in dye sensitized solar cells. Renewable Energy. 2010 Dec 1;35(12):2776-80.

[103] Xu J, Fan K, Shi W, Li K, Peng T. Application of ZnO micro-flowers as scattering layer for ZnO-based dye-sensitized solar cells with enhanced conversion efficiency. Solar energy. 2014 Mar 1;101:150-9.

[104] Song K, Jang I, Song D, Kang YS, Oh SG. Echinoid-like particles with high surface area for dye-sensitized solar cells. Solar energy. 2014 Jul 1;105:218-24.

[105] Golobostanfard MR, Abdizadeh H. Hierarchical porous titania/carbon nanotube nanocomposite photoanode synthesized by controlled phase separation for dye sensitized solar cell. Solar energy materials and solar cells. 2014 Jan 1;120:295-302.

[106] Satapathi S, Gill HS, Das S, Li L, Samuelson L, Green MJ, Kumar J. Performance enhancement of dye-sensitized solar cells by incorporating graphene sheets of various sizes. Applied surface science. 2014 Sep 30;314:638-41.

[107] Fan J, Li Z, Zhou W, Miao Y, Zhang Y, Hu J, Shao G. Dye-sensitized solar cells based on TiO2 nanoparticles/nanobelts double-layered film with improved photovoltaic performance. Applied Surface Science. 2014 Nov 15;319:75-82.

[108] Zi M, Zhu M, Chen L, Wei H, Yang X, Cao B. ZnO photoanodes with different morphologies grown by electrochemical deposition and their dye-sensitized solar cell properties. Ceramics international. 2014 Jul 1;40(6):7965-70.

[109] Zhu S, Shan L, Tian X, Zheng X, Sun D, Liu X, Wang L, Zhou Z. Hydrothermal synthesis of oriented ZnO nanorod–nanosheets hierarchical architecture on zinc foil as flexible photoanodes for dye-sensitized solar cells. Ceramics International. 2014 Sep 1;40(8):11663-70.

[110] Xu F, Wu Y, Zhang X, Gao Z, Jiang K. Controllable synthesis of rutile TiO2 nanorod array, nanoflowers and microspheres directly on fluorine doped tin oxide for dye sensitised solar cells. Micro and Nano Letters. 2012 Aug 1;7(8):826-30.

[111] Bokhari M, Kasi AK, Kasi JK, Gujela OP, Afzulpurkar N. Improving photoelectric conversion efficiency of DSSC using ZnO/ZnP composite nanorods. International Journal of Nanomanufacturing. 2015;11(1-2):56-63.

[112] Fang X, Li Y, Zhang S, Bai L, Yuan N, Ding J. The dye adsorption optimization of ZnO nanorod-based dye-sensitized solar cells. Solar Energy. 2014 Jul 1;105:14-9.

[113] Saurdi I, Mamat MH, Musa MZ, Amalina MN, Abdullah MH, Rusop M. Photoanode of nanostructured TiO 2 prepared by ultrasonic irradiation assisted of sol-gel with P-25 for dye-sensitized Solar Cells. InRSM 2013 IEEE Regional Symposium on Micro and Nanoelectronics 2013 Sep 25 (pp. 258-261). IEEE.

[114] Sangiorgi A, Bendoni R, Sangiorgi N, Sanson A, Ballarin B. Optimized TiO2 blocking layer for dye-sensitized solar cells. Ceramics International. 2014 Aug 1;40(7):10727-35.

[115] Han Q, Yu M, Liu J. Nanocrystalline titanium dioxide prepared by hydrothermal method and its application in dye sensitised solar cells. Micro and Nano Letters. 2013 May 1;8(5):238-42.

[116] Kim DY, Joshi BN, Park JJ, Lee JG, Cha YH, Seong TY, Noh SI, Ahn HJ, Al-Deyab SS, Yoon SS. Graphene–titania films by supersonic kinetic spraying for enhanced performance of dye-sensitized solar cells. Ceramics International. 2014 Aug 1;40(7):11089-97.

[117] Hu JE, Yang SY, Chou JC, Shih PH. Fabrication of flexible dye sensitised solar cells with titanium dioxide thin films based on screen printing technique. Micro and Nano Letters. 2012 Dec 1;7(12):1162-5.

[118] Shanmugam M, Baroughi MF, Galipeau D. High VOC dye sensitised solar cell using RF-sputtered TiO2 compact layers. Electronics letters. 2009 Jun 4;45(12):648-9.

[119] Chou CS, Chou FC, Su FC, Wu P. Design and development of electronic-and micro-structures for multi-functional working electrodes in dye-sensitized solar cells. Advanced Powder Technology. 2014 Nov 1;25(6):1679-87.

[120] Niaki AG, Bakhshayesh AM, Mohammadi MR. Double-layer dye-sensitized solar cells based on Zn-doped TiO2 transparent and light scattering layers: Improving electron injection and light scattering effect. Solar Energy. 2014 May 1;103:210-22.

[121] Jeong JA, Kim HK. Thickness effect of RF sputtered TiO2 passivating layer on the performance of dye-sensitized solar cells. Solar Energy Materials and Solar Cells. 2011 Jan 1;95(1):344-8.

[122] Bu IY. Synthesis of graphitic carbon nano-onions for dye sensitized solar cells. Solar energy. 2014 Jul 1;105:236-42.

[123] Iefanova A, Nepal J, Poudel P, Davoux D, Gautam U, Mallam V, Qiao Q, Logue B, Baroughi MF. Transparent platinum counter electrode for efficient semi-transparent dye-sensitized solar cells. Thin Solid Films. 2014 Jul 1;562:578-84.

[124] Wang M, Zhao Y, Yuan S, Wang Z, Ren X, Zhang M, Shi L, Li D. High electro-catalytic counter electrode based on three-dimensional conductive grid for dye-sensitized solar cell. Chemical Engineering Journal. 2014 Nov 1;255:424-30.

[125] Dong H, Wu Z, Gao Y, El-Shafei A, Jiao B, Dai Y, Hou X. A nanostructure-based counter electrode for dye-sensitized solar cells by assembly of silver nanoparticles. Organic Electronics. 2014 Jul 1;15(7):1641-9.

[126] Ruhane TA, Islam MT, Rahaman MS, Bhuiyan MM, Islam JM, Bhuiyan TI, Khan KA, Khan MA. Impact of photo electrode thickness and annealing temperature on natural dye sensitized solar cell. Sustainable energy technologies and assessments. 2017 Apr 1;20:72-7.

[127] Nakade S, Saito Y, Kubo W, Kanzaki T, Kitamura T, Wada Y, Yanagida S. Enhancement of electron transport in nano-porous TiO2 electrodes by dye adsorption. Electrochemistry communications. 2003 Sep 1;5(9):804-8.

[128] Ngamsinlapasathian S, Sreethawong T, Suzuki Y, Yoshikawa S. Single-and double-layered mesoporous TiO2/P25 TiO2 electrode for dye-sensitized solar cell. Solar Energy Materials and Solar Cells. 2005 Mar 1;86(2):269-82.

[129] Miller, E. L., Rocheleau, R. E., and Deng, X. M. (2003). Design considerations for a hybridamorphous silicon/photoelectrochemical multijunction cell for hydrogen production. International Journal of Hydrogen Energy, 28(6), 615-623.

[130] E.L. Miller, R.E. Rocheleau, Photoelectrochemical hydrogen production, In: Proceedings of the 2000 U.S. Department of Energy Hydrogen Program Annual Review Meeting, San Ramon, California, U.S. Department of Energy, 2000

[131] Yuwawech K, Wootthikanokkhan J, Wanwong S, Tanpichai S. Polyurethane/esterified cellulose nanocrystal composites as a transparent moisture barrier coating for encapsulation of dye sensitized solar cells. Journal of Applied Polymer Science. 2017 Dec 5;134(45):45010.

[132] Chen X, Mao SS. Titanium dioxide nanomaterials: synthesis, properties, modifications, and applications. Chemical reviews. 2007 Jul 11;107(7):2891-959.

[133] M.R. Hoffmann, S.T. Martin, W.Y. Choi and D.W. Bahnemann, Environmental applications of semiconductor photocatalysis. Chem. Rev. 95 (1995) 69–96.

[134] Carp O, Huisman CL, Reller A. Photoinduced reactivity of titanium dioxide. Progress in solid state chemistry. 2004 Jan 1;32(1-2):33-177.

[135] M. Grätzel, Solar energy conversion by dye-sensitized photovoltaic cells. Inorg. Chem. 44 (2005) 6841–5851.

[136] Hiemenz PC, Rajagopalan R, editors. Principles of Colloid and Surface Chemistry, revised and expanded. CRC press; 2016 Oct 4.

[137] Eddaoudi M. Characterization of Porous Solids and Powders: Surface Area, Pore Size and Density By S. Lowell (Quantachrome Instruments, Boynton Beach), JE Shields (CW Post Campus of Long Island University), MA Thomas, and M. Thommes (Quantachrome In-struments). Kluwer Academic Publishers: Dordrecht, The Netherlands. 2004.348 pp.ISBN 1-4020-2302-2.

[138] Lyklema J, editor. Solid-liquid interfaces. Academic Press; 1995.

[139] Monk PM, Mortimer RJ, Rosseinsky DR. Electrochromism: fundamentals and applications. John Wiley & Sons; 2008 Sep 26.

[140] Brunauer S. The Adsorption of Gases and Vapors Vol I-Physical Adsorption. Brunauer Press; 2008.

[141] Park JK, editor. Principles and applications of lithium secondary batteries. John Wiley & Sons; 2012 Jun 13.

[142] Hubbard AT. Encyclopedia of surface and colloid science. CRC press; 2002 Jul 18.

[143] Che M, Védrine JC, editors. Characterization of solid materials and heterogeneous catalysts: From structure to surface reactivity. John Wiley & Sons; 2012 Apr 16.

[144] Lowell S, Shields JE. Powder surface area and porosity. Springer Science & Business Media; 2013 Nov 11

[145] Fan LS, Zhu C. Principles of gas-solid flows. Cambridge University Press; 2005 Oct 13

[146] Steele WA, Zgrablich G, Rudzinski W, editors. Equilibria and dynamics of gas adsorption on heterogeneous solid surfaces. Elsevier; 1996 Dec 17.

[147] Thommes M, Kaneko K, Neimark AV, Olivier JP, Rodriguez-Reinoso F, Rouquerol J, Sing KS. Physisorption of gases, with special reference to the evaluation of surface area and pore size distribution (IUPAC Technical Report). Pure and Applied Chemistry. 2015 Oct 1;87(9-10):1051-69.

[148] Chang-ha L, editor. Adsorption Science And Technology, Proceedings Of The Third Pacific Basin Conference. World Scientific; 2003 Apr 24.

[149] Thomas JM, Thomas WJ. Principles and practice of heterogeneous catalysis. John Wiley & Sons; 2014 Dec 11.

[150] Sing, K., Everett, D., Haul, R., Moscou, L., Peirotti, R., Rouquerol, J. et al. (1985). IUPAC commission on colloid and surface chemistry including catalysis. Pure Appl. Chem, 57 ,603–619.

[151] Rouquerol, J., Rouquerol, F., & Sing, K. S. W. (1998). Absorption by powders and porous solids. Academic press

[152] Naumov, S. (2009). Hysteresis Phenomena in Mesoporous Materials. Ph.D. thesis Universitat Leipzig

[153] Groen, J. C., Peffer, L. A. A., & Perez-Ramirez, J. (2003). Pore size determination in modified micro-and mesoporous materials. pitfalls and limitations in gas adsorption data analysis. Microporous and Mesoporous Materials, 60 , 1–17.

[154] Conner, W., Cevallos-Candau, J., Weist, E., Pajares, J., Mendioroz, S., & Cortes, A. (1986). Characterization of pore structure: porosimetry and sorption. Langmuir, 2 , 151–154.

[155] Mason G. The effect of pore space connectivity on the hysteresis of capillary condensation in adsorption—desorption isotherms. Journal of Colloid and Interface Science. 1982 Jul 1;88(1):36-46.

[156] Friedrich, W.; Knipping, P.; von Laue, M. Interferenz-Erscheinungenbei Rontgenstrahlen. Sitzungsber. Math.-Phys. Classe Koniglich- Bayerischen Akad. Wiss.Muunchen. 1912, 303–322.

[157] Connolly, J. R. Introduction to X-Ray Powder Diffraction; Spring, 2007. Cullity, B. D. Elements of X-ray Diffraction, 2nd ed.; Addison-Wesley

[158] Brindley, G. W.; Brown, G., eds. Crystal Structures of Clay Minerals and Their Identification. Mineralogical Society: London, 1980.

[159] Roselina NN, Azizan A. Ni nanoparticles: Study of particles formation and agglomeration. Procedia Engineering. 2012 Jan 1;41:1620-6.

[160] K.P.S. Parmar, E. Ramasamy, J. Lee and J.S. Lee, Rapid ($\sim$10 min) synthesis of single-crystalline, anorice TiO_2 mesoparticles with a high photovoltaic efficiency of above 8%. Chem. Commun. 47 (2011) 8572–8574.

[161] H. Jensen, K.D. Joensen, J.-E. Jørgensen, J.S. Pedersen and E.G. Søgaard, Characterization of nanosized partly crystalline photocatalysts. J. Nanoparticle Res. 6 (2004) 519–526.

[162] C. Sanchez, J. Livage, M. Henry and F. Babonneau, Chemical modification of alkoxide precursors. J. Non-Crystalline Solids 100 (1988) 65–75.

[163] U. Schubert, Chemical modification of titanium alkoxides for sol–gel processing. J. Mater. Chem. 15 (2005) 3701–3715.

[164] A. Sacco, Electrochemical impedance spectroscopy: Fundamentals and application in dye-sensitized solar cells. Renewable Sustainable Energy Rev. 79 (2017) 814–829.

[165] Jager-Waldau A. European photovoltaics in world wide comparison. J Non-Cryst Solids 2006;352:1922–7.

[166] Parida B, Iniyan S, Goic R. A review of solar photovoltaic technologies. Renew Sustain Energy Rev 2011;15:1625–36.

[167] Razykov TM, Ferekides CS, Morel D, Stefanakos E, Ullal HS, Upadhyaya HM. Solar photovoltaic electricity: current status and future prospects. Sol Energy 2011;85:1580–608.

[168] Di Francia G. The effect of technological innovations on the cost of the photovoltaic electricity. In2015 International Conference on Renewable Energy Research and Applications (ICRERA) 2015 Nov 22 (pp. 542-546). IEEE.

[169] Sun Y, Yan X, Yuan C, Luo H, Jiang Q. The I–V characteristics of solar cell under the marine environment: Experimental research. In2015 International Conference on Renewable Energy Research and Applications (ICRERA) 2015 Nov 22 (pp. 403-407). IEEE.

[170] Cakmak BY. Solar energy potential of Konya and architectural design criterias for solar energy efficiency. In2015 International Conference on Renewable Energy Research and Applications (ICRERA) 2015 Nov 22 (pp. 1463-1469). IEEE.

[171] Lacerda JS, Van Den Bergh JCJM. Diversity in solar photovoltaic energy: implications for innovation and policy. Renew Sustain Energy Rev 2016;54:331–40.

[172] Gangopadhyay U, Jana S, Das S. State of Art of Solar Photovoltaic Technology. In: Proceedings of International Conference on Solar Energy Photovoltaics; 2013.

[173] Busacca A, Cardona F, Caruso M, Cellura M, Cino A, Miceli R, Parisi A, Pernice R, Galluzzo FR, Viola F. Electrical characterization of low power CIGSSe photovoltaic modules. In2015 International Conference on Renewable Energy Research and Applications (ICRERA) 2015 Nov 22 (pp. 1597-1602). IEEE.

[174] Goetzberger A, Luther J, Willeke G. Solar cells: past, present, future. Sol Energy Mater Sol Cells 2002;74:1–11

[175] Que L, et al. High-efficiency dye-sensitized solar cells based on ultra-long single crystalline titanium dioxide nanowires. J Power Sources 2014;266:440–7.

[176] Fitri A, Benjelloun AT, Benzakour M, Mcharfi M, Hamidi M, Bouachrine M. Theoretical design of thiazolothiazole-based organic dyes with different electron donors for dye-sensitized solar cells. Spectrochim Acta Part A: Mol Biomol Spectrosc 2014;132:232–8.

[177] Saha S, Das P, Chakraborty AK, Sarkar S, Debbarma R. Fabrication of DSSC with nanoporous TiO_2 film and Kenaf Hibiscus dye as sensitizer. International Journal of Renewable Energy Research (IJRER). 2016 Jun 18;6(2):620-7.

[178] Smestad G, Bignozzi C, Argazzi R. Testing of dye sensitized TiO2 solar cells I: Experimental photocurrent output and conversion efficiencies. Solar energy materials and solar cells. 1994 Mar 1;32(3):259-72.

[179] Chou CS, Hsiung CM, Wang CP, Yang RY, Guo MG. Preparation of a counter electrode with P-type NiO and its applications in dye-sensitized solar cell. International Journal of Photoenergy. 2010;2010.

[180] Gong J, Sumathy K, Zhou Z, Qiao Q. Modeling of interfacial and bulk charge transfer in dye-sensitized solar cells. Cogent Engineering. 2017 Jan 1;4(1):1287231.

[181] Thavasi VR, Renugopalakrishnan V, Jose R, Ramakrishna S. Controlled electron injection and transport at materials interfaces in dye sensitized solar cells. Materials Science and Engineering: R: Reports. 2009 Jan 29;63(3):81-99.

[182] Gratzel M. Conversion of sunlight to electric power by nanocrystalline dye-sensitized solar cells. Journal of Photochemistry and Photobiology A: Chemistry. 2004 Jun 1;164(1-3):3-14.

[183] Tripathi B, Yadav P, Kumar M. Charge transfer and recombination kinetics in dye-sensitized solar cell using static and dynamic electrical characterization techniques. Solar Energy. 2014 Oct 1;108:107-16.

[184] Onodera M, Ogiya K, Suzuki A, Tsuboi H, Hatakeyama N, Endou A, Takaba H, Kubo M, Miyamoto A. Modeling of dye-sensitized solar cells based on TiO2 electrode structure model. Japanese Journal of Applied Physics. 2010 Apr 20;49(4S):04DP10.

[185] Ni M, Leung MK, Leung DY. Theoretical modelling of the electrode thickness effect on maximum power point of dye-sensitized solar cell. The Canadian Journal of Chemical Engineering. 2008 Feb;86(1):35-42.

[186] Supriyanto E, Kartikasari HA, Alviati N, Wiranto G. Simulation of Dye-Sensitized Solar Cells (DSSC) Performance for Various Local Natural Dye Photosensitizers. InIOP Conference Series: Materials Science and Engineering 2019 Apr (Vol. 515, No. 1, p. 012048). IOP Publishing.

[187] Jain A, Kapoor A. Exact analytical solutions of the parameters of real solar cells using Lambert W-function. Solar Energy Materials and Solar Cells. 2004 Feb 6;81(2):269-77.

[188] Gagliardi, A., Auf der Maur, M., Pecchia, A., & Di Carlo, A. (2009). Dye Solar Cell Simulations Using Finite Element Method. 2009. 13th International Workshop on Computational Electronics.

[189] D. B. Patel, K. R. Chauhan, and I. Mukhopadhyay. Effect Of Electrode's Geometric Shape, Thickness And Porosity On The Performance Of Dye Sensitized Solar Cell. 2014; 3: 8-19

[190] D. Fitzmaurice. Using spectroscopy to probe the band energetics of transparent nanocrystalline semiconductor films. Sol. Energy Mater. Sol. Cells. 1994; 32: 289-305

[191] N. Papageorgiou. The Performance and Stability of Ambient Temperature Molten Salts for Solar Cell Applications. J. Electrochem. Soc. 1996; 143: 3099.

[192] N. Papageorgiou. An Iodine/Triiodide Reduction Electrocatalyst for Aqueous and Organic Media. J.Electrochem. Soc. 1997; 144: 876

[193] A. Mathew, V. Anand, G. M. Rao, and N. Munichandraiah. Effect of iodine concentration on the PV properties of dye sensitized solar cells for various I2/LiI ratios. Electrochim. Acta. 2013; 87: 92-96

[194] A. M. Gagliardi S Gentilini, D Giordano, F Reale, A Brown, TM Di Carlo, A. Multiscale Modeling of Dye Solar Cells and Comparison With Experimental Data. IEEE J. Sel. Top. Quantum Electron. 2010; 16:1611-1618

[195] Rudra S, Sarker S, Kim DM. Review on simulation of current–voltage characteristics of dye-sensitized solar cells. Journal of Industrial and Engineering Chemistry. 2019 Aug 20.

[196] Penny M, Farrell T, Please C. A mathematical model for interfacial charge transfer at the semiconductor–dye–electrolyte interface of a dye-sensitised solar cell. Solar Energy Materials and Solar Cells. 2008 Jan 1;92(1):11-23.

[197] Thomas S, Deepak TG, Anjusree GS, Arun TA, Nair SV, Nair AS. A review on counter electrode materials in dye-sensitized solar cells. Journal of Materials Chemistry A. 2014;2(13):4474-90.

[198] Grätzel M. Dye-sensitized solar cells. Journal of photochemistry and photobiology C: Photochemistry Reviews. 2003 Oct 31;4(2):145-53.

[199] Oda T, Tanaka S, Hayase S. Differences in characteristics of dye-sensitized solar cells containing acetonitrile and ionic liquid-based electrolytes studied using a novel model. Solar energy materials and solar cells. 2006 Oct 16;90(16):2696-709.

[200] Ferber J, Stangl R, Luther J. An electrical model of the dye-sensitized solar cell. Solar Energy Materials and Solar Cells. 1998 May 12;53(1-2):29-54.

[201] Diantoro M, Suprayogi T, Hidayat A, Taufiq A, Fuad A, Suryana R. Shockley's Equation Fit Analyses for Solar Cell Parameters from IV Curves. International Journal of Photoenergy. 2018;2018. 2018.

[202] Ahmed MT, Gonçalves T, Tlemcani M. Single diode model parameters analysis of photovoltaic cell. In2016 International Conference on Renewable Energy Research and Applications (ICRERA) 2016 Nov 20 (pp. 396-400). IEEE.

[203] Ghani F, Duke M. Numerical determination of parasitic resistances of a solar cell using the Lambert W-function. Solar Energy. 2011 Sep 1;85(9):2386-94.

[204] Tsai JK, Hsu WD, Wu TC, Meen TH, Chong WJ. Effect of compressed TiO2 nanoparticle thin film thickness on the performance of dye-sensitized solar cells. Nanoscale research letters. 2013 Dec;8(1):459.

[205] Kao MC, Chen HZ, Young SL, Kung CY, Lin CC. The effects of the thickness of TiO2 films on the performance of dye-sensitized solar cells. Thin Solid Films. 2009 Jul 1;517(17):5096-9.

[206] Balraju P, Suresh P, Kumar M, Roy MS, Sharma GD. Effect of counter electrode, thickness and sintering temperature of TiO_2 electrode and TBP addition in electrolyte on photovoltaic performance of dye sensitized solar cell using pyronine G (PYR) dye. Journal of Photochemistry and photobiology A: Chemistry. 2009 Jul 5;206(1):53-63.

[207] Miyasaka T, Kijitori Y, Murakami TN, Kimura M, Uegusa S. Efficient non-sintering type dye-sensitized photocells based on electrophoretically deposited TiO2 layers. Chemistry Letters. 2002 Dec 5;31(12):1250-1.

[208] Gomez R, Salvador P. Photovoltage dependence on film thickness and type of illumination in nanoporous thin film electrodes according to a simple diffusion model. Solar Energy Materials and Solar Cells. 2005 Sep 15;88(4):377-88.

[209] Zhao W, Bala H, Chen J, Zhao Y, Sun G, Cao J, Zhang Z. Thickness-dependent electron transport performance of mesoporous TiO2 thin film for dye-sensitized solar cells. Electrochimica Acta. 2013 Dec 30;114:318-24.

[210] Park KH, Kim TY, Kim JH, Kim HJ, Hong CK, Lee JW. Adsorption and electrochemical properties of photoelectrodes depending on TiO2 film thickness for dye-sensitized solar cells. Journal of Electroanalytical Chemistry. 2013 Nov 1;708:39-45.

[211] Docampo P, Guldin S, Steiner U, Snaith HJ. Charge transport limitations in self-assembled TiO2 photoanodes for dye-sensitized solar cells. The journal of physical chemistry letters. 2013 Feb 12;4(5):698-703.

[212] Oktiawati UY, Mohamed NM, Burhanudin ZA. Simulation on the performance of dye solar cell incorporated with TiO2 passivation layer. International Journal of Photoenergy. 2016;2016.

[213] Kumari JM, Sanjeevadharshini N, Dissanayake MA, Senadeera GK, Thotawatthage CA. The effect of TiO2 photo anode film thickness on photovoltaic properties of dye-sensitized solar cells. Ceylon Journal of Science. 2016 Jun 22;45(1)

[214] B. A. Lasia, "Electrochemical impedance spectroscopy and its applications," in Modern Aspects of Electrochemistry, B. E. Conway, J.O.M. Bockris, and R.White, Eds., pp. 143–248, Springer, New York, NY, USA, 2002

[215] J. Bisquert and F. Fabreagat-Santiago, "Impedance spectroscopy: a general introduction and application to dye-sensitized solar cells," in Dye-Sensitized Solar Cells, K. Kalyanasundaram, Ed., p. 457, CRC; Taylor & Francis, Boca Raton, Fla, USA, 2010

[216] J. R. Macdonald, "Impedance spectroscopy," Annals of Biomedical Engineering, vol. 20, no. 3, pp. 289–305, 1992.

[217] J. R. Macdonald and W. B. Johnson, Impedance Spectroscopy, JohnWiley & Sons, New York, NY,USA, 2005

[218] F. Fabregat-Santiago, J. Bisquert, E. Palomares et al., "Correlation between photovoltaic performance and impedance spectroscopy of dye-sensitized solar cells based on ionic liquids,"The Journal of Physical Chemistry C, vol. 111, no. 17, pp. 6550–6560, 2007.

[219] S. Sarker, H. W. Seo, and D. M. Kim, "Calculating current density-voltage curves of dye-sensitized solar cells: a straightforward approach," Journal of Power Sources, vol. 248, pp. 739– 744, 2014.

[220] E. M. Barea, C. Zafer, B. Gultekin et al., "Quantification of the effects of recombination and injection in the performance of dye-sensitized solar cells based on N-substituted carbazole dyes," Journal of Physical ChemistryC, vol. 114, no.46, pp. 19840– 19848, 2010

[221] F. Fabregat-Santiago, H. Randriamahazaka, A. Zaban, J. Garcia- Canadas, G. Garcia-Belmonte, and J. Bisquert, "Chemical capacitance of nanoporous-nanocrystalline TiO_2 in a room temperature ionic liquid," Physical Chemistry Chemical Physics, vol. 8, no. 15, pp. 1827–1833, 2006

[222] F. Fabregat-Santiago, G. Garcia-Belmonte, J. Bisquert,A. Zaban, and P. Salvador, "Decoupling of transport, charge storage, and interfacial charge transfer in the nanocrystalline TiO2/ electrolyte system by impedance methods," The Journal of Physical Chemistry B, vol. 106, no. 2, pp. 334–339, 2002.

[223] J. Halme, P. Vahermaa, K. Miettunen, and P. Lund, "Device physics of dye solar cells," Advanced Materials, vol. 22, no. 35, pp. E210–E234, 2010.

[224] F. Fabregat-Santiago, J. Bisquert, G. Garcia-Belmonte, G. Boschloo, and A. Hagfeldt, "Influence of electrolyte in transport and recombination in dye-sensitized solar cells studied by impedance spectroscopy," Solar Energy Materials and Solar Cells, vol. 87, no. 1–4, pp. 117–131, 2005.

[225] M. Adachi,M. Sakamoto, J. Jiu, Y. Ogata, and S. Isoda, "Determination of parameters of electron transport in dye-sensitized solar cells using electrochemical impedance spectroscopy," The Journal of Physical ChemistryB, vol. 110, no. 28, pp. 13872–13880, 2006

[226] R.Kern, R. Sastrawan, J. Ferber,R. Stangl, andJ.Luther, "Modeling and interpretation of electrical impedance spectra of dye solar cells operated under open-circuit conditions," Electrochimica Acta, vol. 47, no. 26, pp. 4213–4225, 2002. [25]

[227] Wang Q, Moser JE, Grätzel M. Electrochemical impedance spectroscopic analysis of dye-sensitized solar cells. The Journal of Physical Chemistry B. 2005 Aug 11;109(31):14945-53.

[228] A. Hauch and A. Georg, "Diffusion in the electrolyte and charge-transfer reaction at the platinum electrode in dyesensitized solar cells," Electrochimica Acta, vol. 46, no. 22, pp.3457–3466, 2001

[229] L.Han,N.Koide, Y. Chiba, A. Islam, andT.Mitate, "Modelingof an equivalent circuit for dye-sensitized solar cells: improvement of efficiency of dye-sensitized solar cells by reducing internal resistance,"Comptes Rendus Chimie, vol. 9, no. 5-6, pp. 645–651,2006.

[230] Raga SR, Fabregat-Santiago F. Temperature effects in dye-sensitized solar cells. Physical Chemistry Chemical Physics. 2013;15(7):2328-36.

[231] J. Bisquert, "Theory of the impedance of electron diffusion and recombination in a thin layer,"The Journal of Physical Chemistry B, vol. 106, no. 2, pp. 325–333, 2002

[232] J. Bisquert, G. Garcia-Belmonte, F. Fabregat-Santiago, and A. Compte, "Anomalous transport effects in the impedance of porous film electrodes," Electrochemistry Communications, vol. 1, no. 9, pp. 429–435, 1999

[233] J. Bisquert, G. Garcia-Belmonte, F. Fabregat-Santiago, N. S. Ferriols, P. Bogdanoff, and E. C. Pereira, "Doubling exponent models for the analysis of porous film electrodes by impedance. Relaxation of TiO^2 nanoporous in aqueous solution," Journal of Physical Chemistry B, vol. 104, no. 10, pp. 2287–2298, 2000.

[234] S. Sarker, H. W. Seo, and D. M. Kim, "Electrochemical impedance spectroscopy of dye-sensitized solar cells with thermally degraded N719 loaded TiO_2," Chemical Physics Letters, vol. 585, pp. 193–197, 2013. and dynamic electrical characterization techniques. Solar Energy. 2014 Oct 1;108:107-16.

Plagiarism Report

Curiginal

Document Information

Analyzed document	Revised vesrion _New Phd Thesis.pdf (D108760253)
Submitted	6/13/2021 6:00:00 PM
Submitted by	
Submitter email	d.kumar@ddn.upes.ac.in
Similarity	7%
Analysis address	d.kumar.upes@analysis.urkund.com

Sources included in the report

W	URL: http://prr.hec.gov.pk/jspui/bitstream/123456789/11606/1/Niaz%20Muhammad_Chem_2018_QAU_PRR.pdf Fetched: 12/8/2020 7:05:29 AM	⊞	10
W	URL: https://library.ndsu.edu/ir/bitstream/handle/10365/25926/Experimental%20and%20Theoretical%20Studies%20of%20Nanostructured%20Electrodes%20for%20Use%20in%20Dye-Sensitized%20Solar%20Cells.pdf?sequence=2&isAllowed=y Fetched: 12/25/2019 3:15:45 PM	⊞	9
W	URL: https://core.ac.uk/download/pdf/147960864.pdf Fetched: 4/16/2021 11:36:17 AM	⊞	14
W	URL: https://www.scholarmate.com/F/dcfce7c0a665abfc48304d55258ee426 Fetched: 6/13/2021 6:01:00 PM	⊞	19
W	URL: http://library.iugaza.edu.ps/thesis/115517.pdf Fetched: 6/7/2021 6:20:32 AM	⊞	15
W	URL: https://www.eia.gov/todayinenergy/detail.php?id=41433 Fetched: 6/13/2021 6:01:00 PM	⊞	4
W	URL: https://repositorio-aberto.up.pt/bitstream/10216/58589/1/000143578.pdf Fetched: 3/14/2020 8:27:22 AM	⊞	5
W	URL: https://www.science.gov/topicpages/n/nanostructured+dye+solar Fetched: 2/25/2020 4:05:29 AM	⊞	1
W	URL: https://www.mdpi.com/1996-1944/12/12/1998/pdf Fetched: 12/23/2019 5:42:21 PM	⊞	17
W	URL: https://www.researchgate.net/publication/257548004_Review_on_dye-sensitized_solar_cells_DSSCs_Fundamental_concepts_and_novel_materials Fetched: 12/12/2019 12:22:43 PM	⊞	2
W	URL: https://www.researchgate.net/publication/264176536_Enhancement_of_Dye_Adsorption_on_TiO2_Surface_through_Hydroxylation_Process_for_Dye-sensitized_Solar_Cells Fetched: 12/9/2020 2:34:08 PM	⊞	2

A facile low temperature synthesis of TiO2 nanorods for high efficiency dye sensitized solar

Curriculum Vitae

DEEPAK KUMAR

Asst. Professor (Senior Scale)

Vidwan Id: https://vidwan.inflibnet.ac.in/profile/89273

Department of Electrical and Electronics Eng.

University of the Petroleum and Energy Studies

Area of Research

VLSI Microelectronics, Semiconductor Devices (TFETs, OSC, DSSC, OTFT)

Solar cell Technology, Device to Circuit Transformation using Verilog-A.

Education

Year of Passing	Degree/Certificate	Institute	%/CGPA
2015	M. Tech in Microelectronics, VLSI & Display Technology	Indian Institute of Technology, Kanpur	7.0/10
2011	B. Tech in Electronics Engineering	Harcourt Butler Technological Institute, Kanpur	66.05 %
2006	Intermediate (CBSE)	Wood Row School	66.0 %
2004	Matriculation (CBSE)	Wood Row School	61.8 %

Academic Responsibilities

1. Faculty Counsellor of IEEE Student Branch(STB 10991), Electrical and Electronics Eng. Department, UPES.

2. Faculty Coordinator of Spoken Tutorial Program, IIT-B (MHRD India) at Electrical and Electronics Eng. Department, UPES.

Research Projects

1. Effect of particle morphology on efficiency of Dye Sensitized Solar Cells (DSSC).

2. Fabrication of electronic device for quantitation of chemical compounds based on colorimetric analysis.

Publications

1. D.kumar et.al. Facile one-pot hydrothermal synthesis of nanorice-like TiO2 for an efficient dyesensitized solar cell (DSSC).Nanotechnology Perceptions 15 (2019), doi: 10.4024/N03KU19A.ntp.15.01, March 2019

2. D.kumar et.al. Optimizing Photovoltaic Efficiency of a Dye-Sensitized Solar Cell (DSSC) by a Combined (Modelling-Simulation and Experimental) Study.International Journal of Renewable Energy Research (IJRER).March 2020

3. Kumar D, Parmar KP, Kuchhal P. Analysis of charge transport properties of dye-sensitized solar cell (DSSC) with TiO_2 working electrode by employing electrochemical impedance spectroscopy (EIS). network. 2021 Mar 30;19:22-6.

4. Kumar D. Performance evaluation of double gate tunnel FET based chain of inverters and 6-T SRAM cell. Engineering Research Express. 2019 Dec 18;1(2):025055.

5. Kumar D, Jain P. Double Gate Tunnel Field Effect Transistor with Extended Source Structure and Impact Ionization Enhanced Current. InIntelligent Communication, Control and Devices 2018 (pp. 973-980). Springer, Singapore.

6. Jain P, Kumar D. Drive Current Boosting Using Pocket Implant Near to the Strained SiGe/Si Source with Single-Metal/Dual-Metal Double-Gate Tunnel Field-Effect Transistor. InProceeding of International Conference on Intelligent Communication, Control and Devices 2017 (pp. 943-950). Springer, Singapore.

7. Kumar D, Jain P. Performance of Dual Metal-Double Gate Tunnel Field Effect Transistor with Different Dielectrics. InProceeding of International Conference on Intelligent Communication, Control and Devices 2017 (pp. 927-933). Springer, Singapore.

8. Kumar A, Verma G, Gupta MK, Salauddin M, Rehman BK, Kumar D. 3D Multilayer Mesh NoC Communication and FPGA Synthesis. Wireless Personal Communications. 2019 Jun;106(4):1855-73.

9. Yadav A, Kaundal V, Sharma A, Sharma P, Kumar D, Badoni P. Wireless Sensor Network Based Patient Health Monitoring and Tracking System. InProceeding of International Conference on Intelligent Communication, Control and Devices 2017 (pp. 903-917). Springer, Singapore.

10. Chaurasia RK, Mishra R, Mishra RG, Kumar D, Shrivastava AK. Numerical Modelling And Solution Of Microstrip Antenna By Using Caupto Time Fraction RDT Method.International Journal of Scientific & Technology Research. 2019.

11. Kumar D, Mishra RG, Mishra R, Shrivastava AK. Impact of band to band Tunneling on Transient performance of Dual Gate Tunnel Field Effect Transistor (TFET).International Journal of Innovative Technology and Exploring Engineering (IJITEE).2019

12. Mohammad S, Seetha R, Jayamangala S, Rehman BK, Kumar D. Implementation of FM-Based Communication System with 3-Level Parallel Multiplier Structure for Fast Transmission Using FPGA. InIntelligent Communication, Control and Devices 2020 (pp. 619-626). Springer, Singapore.

13. D.kumar et.al. Investigation of Analog Parameters and Miller Capacitance affecting the Circuit Performance of Double Gate Tunnel Field Effect Transistors, Accepted in ICICCD 2020 conference proceedings.

14. Book Chapter accepted: Performance Analysis of Tunnel Field Effect Transistors for Low Power Applications in Wiley, 2021 for edited book: Intelligent green technologies for sustainable smart cities.

Edited Book

Emerging Low-Power Semiconductor Devices: Applications for Future Technology Nodes, CRC Press, Taylor and Francis Group, USA. PB ISBN 978-1-032-14730-7.